Growing low-dimensional supramolecular crystals via Organic Solid-Solid Wetting Deposition: physico-chemical basis, structure analysis, and doping of graphene

Alexander Richard Eberle

SIGILL. UNIVERSITAT. LUDOVIC. MAXIM.

München 2018

Growing low-dimensional supramolecular crystals via Organic Solid-Solid Wetting Deposition: physico-chemical basis, structure analysis, and doping of graphene

Alexander Richard Eberle

Dissertation zur Erlangung des Doktorgrades
an der Fakultät für Geowissenschaften
der Ludwig-Maximilians-Universität
München

vorgelegt von
Alexander Richard Eberle
aus Ebersberg

München, den 23. August 2018

Erstgutachter:	Prof. Dr. Wolfgang W. Schmahl
Zweitgutachter:	Prof. Dr. Guntram Jordan
Tag der mündlichen Prüfung:	07.02.2019

“Habent parvae commoda magna morae.”

Publius Ovidius Naso

Contents

List of Abbrevations

1D	one-dimensional
2D	two-dimensional
3D	three-dimensional
8CB	octylcyanobiphenyl
AMOLED	active-matrix organic light-emitting diode
CNTs	carbon nanotubes
DMMP	dimethyl methylphosphonate
DMQAC	dimethylquinacridone
HOPG	highly oriented pyrolytic graphite
LED	light-emitting diode
MoS_2	molybdenum disulphide
OSWD	Organic Solid-Solid Wetting Deposition
PTCDA	perylenetetracarboxylicdianhydride
QAC	quinacridone
γQAC	gamma quinacridone
R	Pearson correlation coefficient
R^2	coefficient of determination
RFID	radio-frequency identification
SEM	Scanning Electron Microscopy
STM	Scanning Tunneling Microscopy
STS	Scanning Tunneling Spectroscopy
TNT	2,4,6-trinitrotoluene
z33	point within a zeta potential distribution where 33 % of the distribution is more negative and 66 % is more positive

Abstract

Carbon-based (nano)electronics, utilising the outstanding electronic properties of graphene, serve as a promising approach in overcoming the limitations of silicon-based electronics, thereby aiding the development of innovative future electronic devices. In this regard, the supramolecular self-assembly is a well-established procedure for the bottom-up fabrication of low-dimensional nanostructures and adsorbates from molecular units, as it can easily be directed via the programmable, non-covalent interactions. However, a deeper insight reveals the expensive and technically demanding side of the related, commonly used standard technologies, thus limiting their applicability in the large-scale production of electronic devices.

Keeping in mind the above limitations, an alternative deposition approach was developed, termed as the "Organic Solid-Solid Wetting Deposition" (OSWD). For this, the underlying, basic solid-solid wetting phenomenon occurs at the solid-solid interface and generates supramolecular adsorbate structures directly from dispersed three-dimensional (3D) organic semiconductor crystals, under ambient conditions and in a straightforward way. OSWD therefore does not require dissolving, melting or evaporation of the source crystals and thus presents itself as a highly promising approach for various research and technology fields.

However, the start of the current work saw a lack in profound understanding of the physico-chemical basis of the OSWD process, preventing thus the broader development of ways of catalysing the basic effect. This hence made it impossible to assess the potentials of the OSWD technology, especially when it comes to the area of carbon-based electronics. In order to explore these basics, model systems were investigated in *ceteris paribus* approaches. These model systems were composed out of several substrate materials (highly oriented pyrolytic graphite (HOPG), carbon nanotubes, graphene, and molybdenum disulphide (MoS_2)), varying aqueous and organic dispersing agents, and of one of two different organic semi-conductive pigments (gamma quinacridone and dimethylquinacridone) as the active phases.

The experimental analysis of the model systems was done using Scanning Tunneling Microscopy (STM), Scanning Tunneling Spectroscopy (STS), Raman spectroscopy, Scanning Electron Microscopy (SEM), and by analysing the particle size, the zeta potential, and the corresponding pH values. Additional insights into the basis of the OSWD were gained using theoretical approaches, as via force field calculations and refined DLVO simulations.

The findings and results of the present dissertation could be briefly summarized as follows:

- Up to temperatures of at least 160 °C, the adsorbate layer generated via OSWD shows a distinct domain structure and fragmentary coverage, due to limited surface diffusion and the binding energy anisotropy of the 3D semiconductor crystals. From 240 °C, however, a large-scale, homogeneous, and continuous monolayer is formed. In addition, the supramolecular adsorbates generated are thermally stable up to at least 300 °C, temporally stable for at least 36 days, and resistant to humidity and water.

- A fundamental model has been proposed which reveals that the OSWD process is governed by a complex balance of physico-chemical interactions between various components in the system. As a result, a semiconductor crystal approaching a substrate undergoes various sub-processes that significantly affect the OSWD. The catalysing effect of the dispersing agent is largely determined by the electrical double layer forces, including the so-called Casimir-like fluctuation-induced forces. These forces can be quantified using the zeta potential. In addition, a direct physical contact between semiconductor crystal and substrate is essential for triggering the OSWD, which is facilitated in particular by the effect of dewetting in hydrophobic nano-confinement.

- Based on the gained deeper understanding of OSWD, insoluble organic semiconductors can now be processed using new organic or aqueous dispersing agents, significantly reducing the production costs of the technology. In addition, the adsorbate layer design and surface coverage (the latter between 0.3 and 98 %) can now be globally controlled. This is realized by the variety of suitable dispersing agents, additives such as salts, acids, bases, as well as advanced sample preparation and post-processing techniques. The OSWD approach is thus characterized by its eco-friendliness, free scalability and large-scale feasibility, thus demonstrating its competitiveness vis-à-vis standard technologies.

- As a brief outlook, the various possibilities for triggering and controlling the OSWD identified in this dissertation open the way for the application of the approach to different processing technologies such as inkjet-printing, drop-casting or spin-coating. Further, the STM and STS analysis clearly showed that graphene can be chemically doped via OSWD. This paves the way for future bandgap engineering of graphene. In addition, there is clear application potential for advanced electrical devices based on pigment-functionalized graphene, such as printed and flexible carbon-based electronics.

Zusammenfassung

Die kohlenstoffbasierte (Nano-) Elektronik nutzt die herausragenden Eigenschaften des Graphens aus und präsentiert sich deshalb als ein sehr vielversprechenden Ansatz, um die Grenzen der siliziumbasierten Elektronik zu überwinden und um innovative und zukunftsträchtige elektronische Geräte zu entwickeln. Vor diesem Hintergrund stellt die supramolekulare Selbstassemblierung ein etabliertes Verfahren zur Bottom-up Herstellung von niedrigdimensionalen Nanostrukturen und Adsorbaten aus molekularen Einheiten dar, da diese mithilfe programmierbarer nichtkovalenter Wechselwirkungen leicht gesteuert werden kann. Bei näherer Betrachtung entpuppen sich die in diesem Kontext gemeinhin verwendeten Standardtechnologien allerdings als teuer und technisch aufwendig, was deren Anwendbarkeit für die großtechnische Herstellung von elektronischen Geräten stark einschränkt.

In Anbetracht der oben genannten Beschränkungen wurde eine neue Depositionsmethode entwickelt, die den Namen „Organic Solid-Solid Wetting Deposition" (OSWD) erhielt. Das zugrundeliegende, fundamentale Phänomen der Festphasenbenetzung tritt an der fest/fest Grenzfläche auf und erzeugt supramolekulare Adsorbatstrukturen direkt aus dispergierten dreidimensionalen (3D) organischen Halbleiterkristallen, und das unter Umgebungsbedingungen und auf unkomplizierte Art und Weise. Die OSWD erfordert daher weder das Auflösen, das Schmelzen, noch das Verdampfen der Ursprungskristalle, was sie zu einem vielversprechenden Ansatz für verschiedene Forschungs- und Technologiebereiche macht.

Zu Beginn der vorliegenden Dissertation fehlte jedoch ein tiefgreifendes Verständnis der physikalisch-chemischen Grundlagen des OSWD Prozesses, was die weitere Entwicklung von Methoden, den grundlegenden Effekt zu katalysieren, verhinderte. Dies machte eine Einschätzung der Potentiale der OSWD Technologie unmöglich, insbesondere für den Bereich der kohlenstoffbasierten Elektronik. Um diese Grundlagen nun zu erforschen, wurden Modellsysteme in *ceteris paribus* Ansätzen untersucht. Die Modellsysteme wurden zusammengesetzt aus verschiedenen Substratmaterialien (in hohem Maße gerichteter pyrolytischer Graphit (HOPG), Kohlenstoffnanoröhrchen, Graphen und Molybdändisulfid (MoS_2)), variierenden wässrigen und organischen Dispersionsmedien, und aus einem von zwei organischen, halbleitenden Pigmenten (Gammachinacridon und Dimethylchinacridon) als den aktiven Phasen.

Zur experimentellen Analyse der Modellsysteme wurden Rastertunnelmikroskopie (STM), Rastertunnelspektroskopie (STS), Raman-Spektroskopie und Rasterelektronenmikroskopie verwendet und darüber hinaus wurden die Partikelgröße, das Zetapotential und der pH-Wert analysiert. Zusätzliche Erkenntnisse über die Grundlagen der OSWD wurden mithilfe theoretischer Methoden wie z.B. durch Kraftfeldrechnungen und weiterentwickelte DLVO Simulationen gewonnen.

Eine kurze Zusammenfassung der Erkenntnisse und Ergebnisse der vorliegenden Dissertation:

- Bis zu Temperaturen von mindestens 160 °C weist die mittels OSWD erzeugte Adsorbatschicht eine ausgeprägte Domänenstruktur und eine nur partielle Bedeckung auf, die ihre Ursache in der limitierten Oberflächendiffusion und der Anisotropie der Bindungsenergie der 3D Halbleiterkristalle hat. Ab 240 °C bildet sich jedoch eine großflächige, homogene und lückenlose Monoschicht. Darüber hinaus sind die erzeugten supramolekularen Adsorbate temperaturbeständig bis mindestens 300 °C, mindestens 36 Tage lagerstabil, sowie feuchtigkeits- und wasserbeständig.

- Ein fundamentales Modell wurde vorgeschlagen, das zeigt, dass der OSWD-Prozess abhängig ist von einem komplexen Gleichgewicht physikalisch-chemischer Wechselwirkungen zwischen verschiedenen Komponenten im System. Infolgedessen durchläuft ein Halbleiterkristall, der sich einem Substrat nähert, verschiedene Teilprozesse, die die OSWD maßgeblich beeinflussen. Die katalytische Wirkung des Dispersionsmediums wird dabei maßgeblich von den elektrischen Doppelschichtkräften bestimmt, einschließlich der sogenannten Casimir-ähnlichen fluktuationsinduzierten Kräfte. Diese Kräfte lassen sich anhand des Zetapotentials quantifizieren. Für das Auslösen der OSWD ist darüber hinaus ein direkter physischer Kontakt zwischen Halbleiterkristall und Substrat essentiell, welcher insbesondere durch den Effekt der Entnetzung in einem hydrophoben und örtlich im Nanometerbereich begrenzten Raum ermöglicht wird.

- Auf der Grundlage des gewonnenen tieferen Verständnisses von der OSWD können jetzt unlösliche organische Halbleiter mithilfe neuer organischer oder wässriger Dispersionsmedien verarbeitet werden, wodurch sich die Produktionskosten der Technologie deutlich reduzieren. Darüber hinaus können das Adsorbatschichtdesign und die Oberflächenbedeckung (letztere zwischen 0,3 und 98 %) jetzt auch global gesteuert werden. Dies wird ermöglicht durch die Vielzahl an geeigneten Dispersionsmedien, Additiven wie Salze, Säuren, Basen, sowie fortschrittlichen Probenvorbereitungs- und Nachbearbeitungstechniken. Die OSWD-Methode zeichnet sich somit durch ihre Umweltfreundlichkeit, eine freie Skalierbarkeit und großtechnische Umsetzbarkeit aus, und demonstriert damit ihre Wettbewerbsfähigkeit gegenüber den Standardtechnologien.

- Perspektivisch gestatten die in dieser Dissertation identifizierten vielfältigen Möglichkeiten zur Auslösung und Steuerung der OSWD die Verwendung der Methode in verschiedenen Verarbeitungstechnologien wie Tintenstrahldruck, Fallguss oder Rotationsbeschichtung. Darüber hinaus zeigten die STM- und STS-Analysen deutlich, dass Graphen mithilfe der OSWD chemisch dotiert werden kann. Dies ebnet den Weg für ein zukünftiges Bandgap Engineering von Graphen. Überdies ergibt sich ein deutliches Anwendungspotential für fortschrittliche elektrische Bauteile auf Basis von pigmentfunktionalisiertem Graphen und damit beispielsweise im Bereich der gedruckten und flexiblen kohlenstoffbasierten Elektronik.

1. Introduction

1.1. Carbon-based Electronics

More than a decade ago, it became evident that the miniaturisation of silicon-based electronics is limited and that it will soon reach its termination [1-2]. Consequently, numerous scientists began exploring the prospects of carbon-based (nano)electronics, to utilise the outstanding electronic properties of graphene, and thus to enhance the performance of existing and for the development of future electronic devices (like the flexible or inkjet-printed electronics) [2-10]. However, a deeper insight revealed the production of functional nano-systems, like the nanoscale transistors, to be quite a challenging task [10-14]. Nonetheless, for the fabrication of essential semi-conductive sub-regions, a promising approach that came forward was providing a bandgap to the graphene substrate, by covering it with a monolayer of an organic semiconductor [6-8].

An established way to achieve such a monolayer is by utilizing the procedure of supramolecular self-assembly. Programmable, non-covalent interactions (hydrogen bonding, Van-der-Waals, π–π stacking, and electrostatics) are employed in this respect for the bottom-up fabrication of low-dimensional nanostructures and adsorbates, formed from organic semiconductor molecules [10-14]. The corresponding bottom-up assembly could be executed via two common techniques: vapor deposition and liquid phase deposition [15,16]. However, both the approaches possess distinct limitations: the vapor deposition methods, as the organic molecular beam deposition, for instance, being applicable only to a few organic substances that survive a thermally enforced vacuum sublimation [16-19,23]. Liquid phase deposition, on the other hand, as the drop-casting or spin-coating methods [18], are based on chemical solutions, being thus unable to incorporate most of the organic pigments with promising semi-conductive properties, owing to their insolubility in almost all the liquid media. The latter drawback, hence, limits the processing of the organic pigments without a chemical functionalization that otherwise enables their dissolution [18,19,23]. However, the customized synthesis of functionalized semiconductors is expensive, particularly in relation to the standard pigments already being used in the industry.

1.2. The Organic Solid-Solid Wetting Deposition

Keeping in mind the above limitations, hence, an alternative deposition approach was developed, termed as the “Organic Solid-Solid Wetting Deposition” (OSWD) technique [19-24]. Compared to the time-consuming and expensive standard manufacturing techniques (based on either the vapour or the liquid phase deposition approaches, as introduced above), this new deposition technique comes up with several advantages, as discussed next. Firstly, the OSWD marks as a highly straightforward method: under ambient conditions, the powdered organic semiconductor is dispersed in an appropriate dispersing agent and then drop-casted on an inorganic substrate. Soon (within few seconds or less [22]), two-dimensional (2D) supramolecular adsorbates form directly from the three-dimensional (3D) particles, covering the substrate’s surface. Thus, the technical effort for the application of the OSWD is rather low, which limits the potential investment costs for future industrial applications and makes the technology easily up-scalable. Additionally, with results revealing the ability of even purified water to catalyse the OSWD [22], the technique marks as both to be cheap and environmentally friendly.

Furthermore, briefly summarising the basics of OSWD, the whole process is based on the effect of solid-solid wetting [25-27], with the gradient of the surface free energy serving as the prime driving force behind the technology. Consequently, the OSWD technique is capable of processing various organic semiconductors such as quinacridone, dimethylquinacridone (DMQAC), acridone or perylenetetracarboxylic dianhydride (PTCDA), and can be applied to several substrates such as graphite, graphene, carbon nanotubes (CNTs) or molybdenum disulphide (MoS_2), with minimum effort [20-23,42]. Owing to the above advantages, OSWD can hence be found relevant in a series of applications, as in the field of low-dimensional crystal engineering on surfaces [24,28-29], chemical doping and bandgap engineering of graphene [21], and say for the fabrication of organic field-effect transistors [18].

1.3. The OSWD Model Systems

1.3.1. Composition of the Model Systems

In order to explore the physico-chemical basis of the OSWD, model systems out of highly oriented pyrolytic graphite (HOPG) as the substrate material, varying aqueous and organic dispersing agents, and the organic semi-conductive pigment gamma quinacridone (γQAC) as the active phase were utilized in *ceteris paribus* approaches. γQAC is known to be a cheap and commercially available pigment with promising electrical properties, low toxicity, an excellent physical and chemical stability, and with biocompatibility for applications in the living organism [30-36]. Furthermore, the gamma polymorph has been known to be the most stable out of the four possible 3D crystal structures (α^{I}, α^{II}, β, and γ), with the polymorphs being built up by the linear QAC molecules connected with their neighbours via four hydrogen bonds of the type NH···O=C [40, 41]. For the chemical structure of a single QAC molecule refer Figure 1.1, for the crystallographic data of the quinacridone polymorphs refer Table 1.1, and for the force field calculated crystal morphology of a three-dimensional γQAC crystal facing a HOPG substrate refer Figure 1.2. At standard atmospheric pressure, QAC crystals are entirely insoluble both in water [37-40] and in common organic solvents [32,40]. As a result, until now, QAC monolayers could only be assembled either via organic molecular beam deposition in ultra-high vacuum [36], or by the use of soluble QAC derivates [32], making the γQAC thus highly suitable for solid-solid wetting studies. Moreover, additional experiments were performed utilizing alternative model systems, references to them being made elsewhere in the text, as and when appropriate.

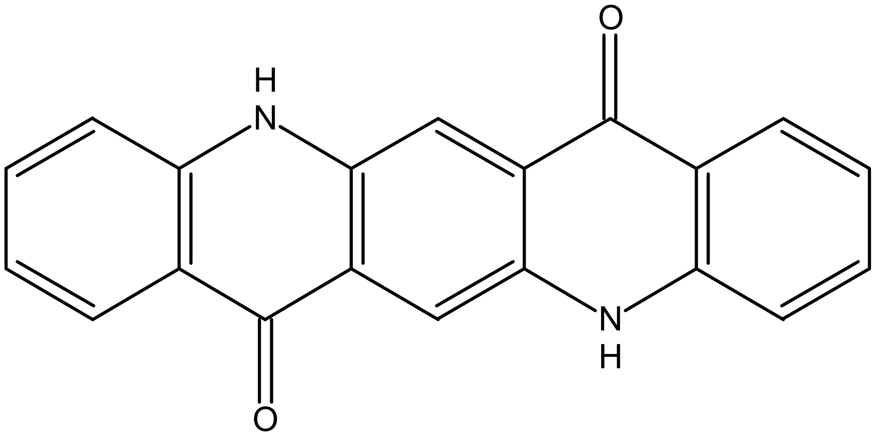

Figure 1.1 Chemical structure of the QAC molecule.

Table 1.1 Crystallographic data of the quinacridone polymorphs, determined at a temperature of 293 K [40].

Crystal phase	$\boldsymbol{\alpha^{I}}$	$\boldsymbol{\alpha^{II}}$	**β**	**γ**
a [Å]	3.802	14.934	5.692	13.697
b [Å]	6.612	3.622	3.975	3.881
c [Å]	14.485	12.935	30.02	13.402
α [°]	100.68	91.39	90.00	90.00
β [°]	94.40	107.12	96.76	100.44
γ [°]	102.11	92.84	90.00	90.00
Volume V [$Å^3$]	355.0	667.8	674.5	700.6

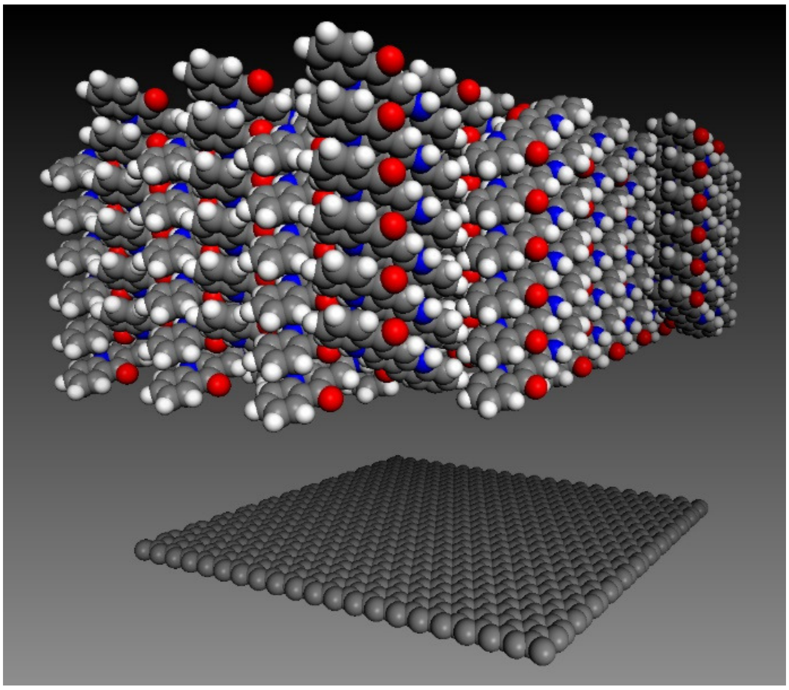

Figure 1.2 Force field calculated simulation of a γQAC crystal facing a HOPG substrate [22].

1.3.2. Standard Sample Preparation Method

With respect to the used model systems, the standard OSWD preparation procedure called for simply mixing a fine powder (2 % by weight) of γQAC crystals (refer Figure 1.3) in an organic or aqueous liquid medium. The insoluble molecular crystals lead to particle dispersions within the mixture, with the liquid medium thereby serving as the dispersing agent. Next, these dispersed organic crystals are drop-casted under ambient conditions onto the HOPG substrate. An OSWD is triggered if an organic crystal physically contacts the substrate, provided a sufficient gradient of the surface free energy prevails. Consequently, semiconductor molecules detach themselves from the contacting 3D crystal and get adsorbed onto the substrate's surface. This eventually leads the adsorbed molecules to assemble into highly ordered supramolecular architectures [19-23]. Depending on the choice of the dispersing agent, the OSWD's outcome can be probed via Scanning Tunneling Microscopy (STM) under ambient conditions, scanning either directly within the dispersion, or post the drop-casted dispersion is dried and the dry sample's surface covered with a thin layer of dodecane. For the latter case, dodecane was found to neither trigger the OSWD nor form supramolecular assemblies, except preventing the formation of a contamination layer, condensed from the air [43,44]. Though the preparation procedure seems to be very straightforward, understanding the formation process and outcomes of the OSWD technique possess great challenges, resolving which being the prime aim of the current dissertation.

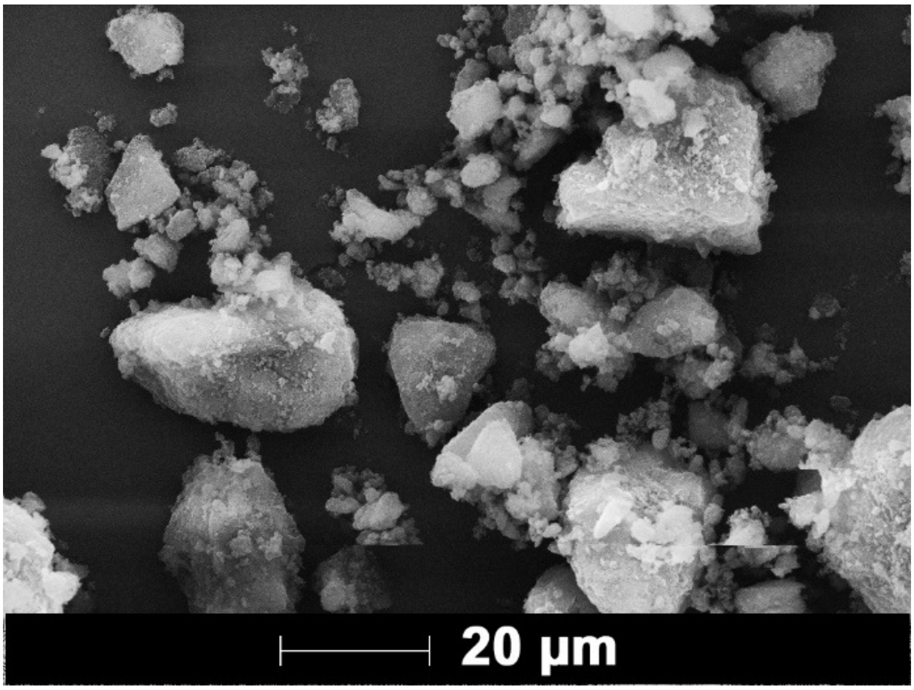

Figure 1.3 Scanning Electron Microscopy (SEM) picture of 3D γQAC crystals [22].

1.3.3. The Results of the OSWD

Probing of the OSWD generated adsorbate structures via STM revealed that the QAC molecules self-assemble into one-dimensional (1D) supramolecular chains via NH···O=C hydrogen bonds, in accordance to the QAC molecule's functional groups (refer Figure 1.4) [19-23]. The supramolecular chains have a uniform width of 1.63 nm and they appear on the substrate's surface either isolated or arranged into supramolecular arrays, the chains being arranged in the latter multiple parallel and side-by-side [20, applies to the entire paragraph]. It was found that the distance between adjacent QAC chains is a multiple of one of the two different lattice vectors, the related structures being accordingly termed as either the "close-packing QAC chain configuration" (chain distance: 1.63 nm) or the "relaxed QAC chain configuration" (chain distance: 2.04 nm). Further, an overall look at the supramolecular QAC arrays revealed that they exhibited either a high packing density or a low packing density, the latter being due to the absence of QAC chains, leading to gaps (Figure 1.5). With respect to large-scale STM scans, these arrays were imaged as linear features and domains, as can be seen in the Figure 1.5. The analysis of the Fourier transformation of various multi-directional arrays yielded that the arrays exhibit 6 different orientations, corresponding to the preferred directions of the graphitic substrate (Figure 1.6). In addition, QAC bilayer structures were found occasionally, indicating their detectability but absence in most of the STM images. Thus, it was concluded that the processing of γQAC via OSWD leads primarily to the formation of monomolecular thick adsorbate structures, i.e. the 1D and 2D structures.

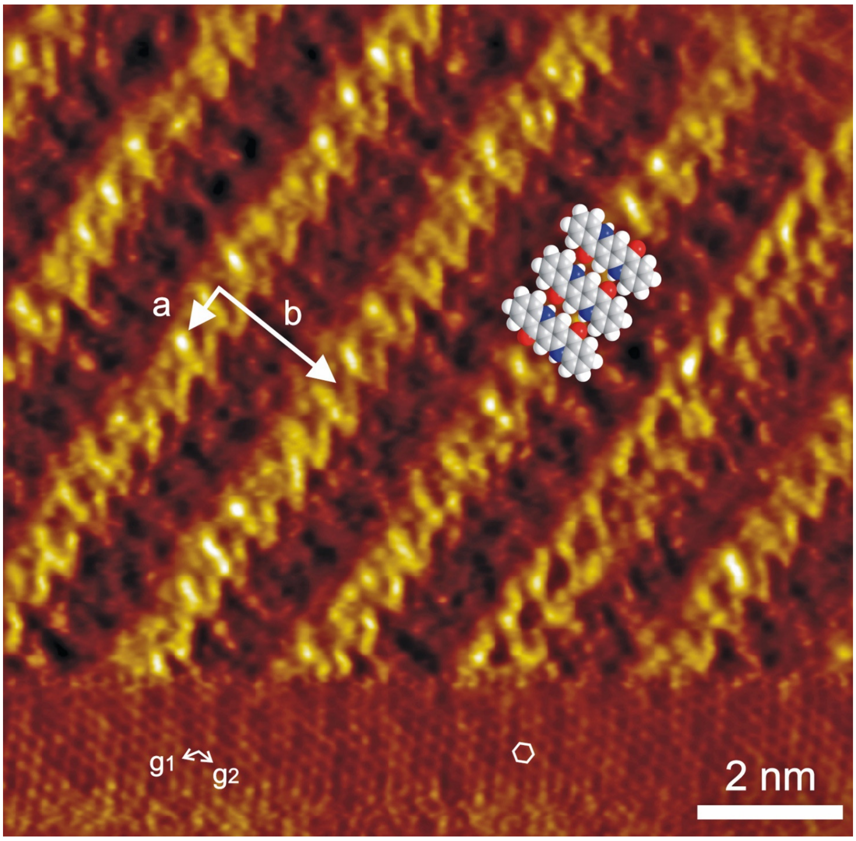

Figure 1.4 STM image (close-up view) of a QAC adsorbate layer, generated via the OSWD (substrate: single layer graphene atop copper). The superimposed and force field calculated inlay on the QAC structures (center right) illustrates the width of a QAC chain (1.63 nm), with relation to the length of the QAC molecule, further highlighting the formation of supramolecular chains via NH···O=C hydrogen bonds. The indicated lattice vectors: a = 0.70, b = 2.04 nm, and an intermediate angle of 88 ° refer to the relaxed QAC chain configuration. The bottom of the image, in addition, presents the underlying graphene substrate's structure, with graphene unit cell having lattice parameters: g1 = g2 = 0.246 nm. The white marked hexagon in the image (atop the graphene substrate) represents one carbon ring of the graphene structure, with an atom-to-atom distance of 0.142 nm. It is to be noted that the QAC formes identical adsorbate structures on the HOPG and on the graphene substrates [20,21]. Image courtesy: Michael Blum.

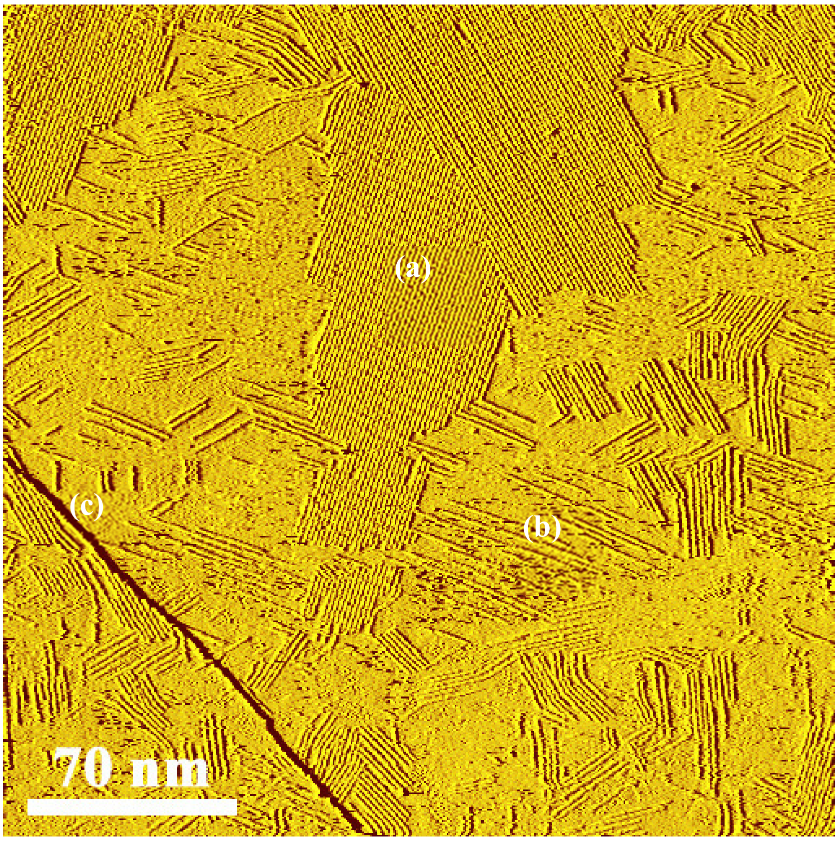

Figure 1.5 STM picture of QAC arrays on a HOPG surface. (a) QAC array with a high packing density, (b) QAC array with a low packing density, (c) 1D QAC chain [20].

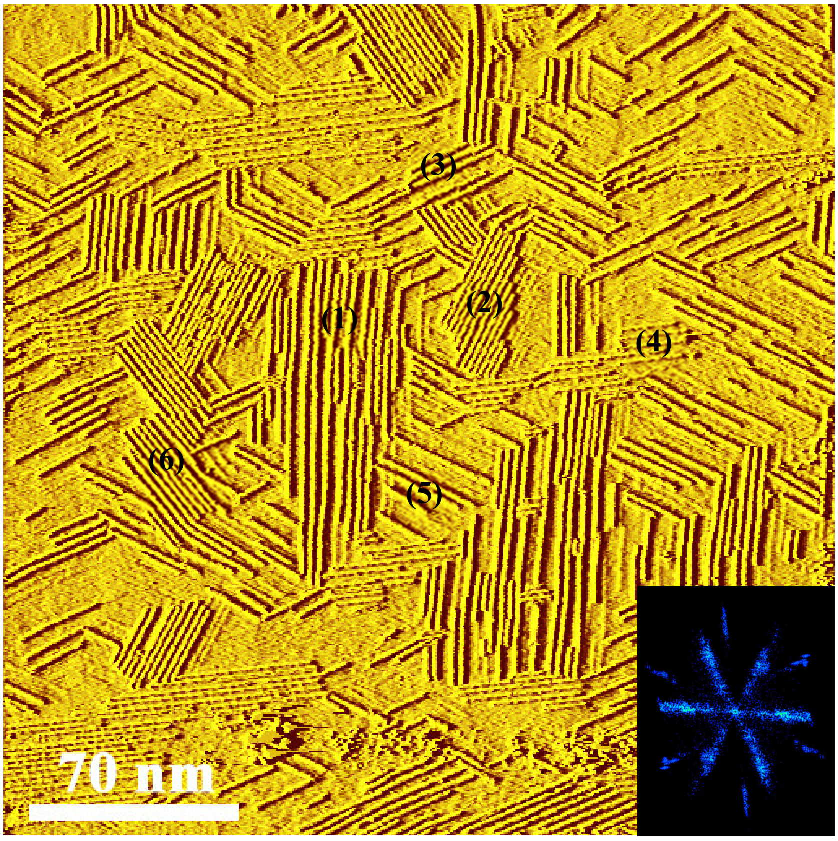

Figure 1.6 The QAC arrays shown in this STM picture (atop a HOPG substrate) depict the six different orientations observed: (1) – (6). The small picture in the bottom right corner shows the fast Fourier transformation of this STM picture. [20].

1.4. General Objective and Thesis Structure

Initially, a lack of profound understanding of the physico-chemical basis of the OSWD restricted the approach to a narrow range of suitable, but rather expensive dispersing agents, like the octylcyanobiphenyl (8CB). This limitation prevented the broader development of ways to catalyse the basic effect, and hence made it impossible to assess the potentials of the OSWD technology in the field of carbon-based electronics. Thereby, the overall goal of this dissertation was to provide a detailed model for the OSWD process, determining the required environmental conditions, describing the contributing physical and chemical interactions, and further characterising in detail the outcomes of the OSWD. Establishment of such a model was further aimed towards assessing the potentials of the OSWD for possible applications as low-dimensional crystal engineering on surfaces, chemical doping and bandgap engineering of graphene, and its process suitability for large-scale applications.

Summarizing the thesis structure, chapter 2.1, titled “Growing Low-dimensional Supramolecular Crystals” (page 13 and following), puts forward the characteristics of supramolecular QAC adsorbate structures generated via the OSWD. The crystallographic properties of the 1D QAC chains and the 2D QAC arrays are determined and their epitaxial dependence on the structure of different substrates (HOPG, CNTs, and MoS_2) revealed. Further, the different large-scale configurations of supramolecular QAC arrays are analysed and the characteristics of bilayer structures explored. Along with this, the chapter investigates the influence of the dispersing agent on the structural properties of the generated adsorbate structures and evaluates the potentials of controlling the self-assembly of the desired QAC structures in advance. Besides, the stability of the adsorbates is examined with respect to factors as the thermal and temporal stability, electric fields, humidity, and water resistance.

Chapter 2.2, titled “Doping Graphene via Organic Solid-Solid Wetting Deposition” and 2.3, titled “Doping Graphene via OSWD - Supporting Information” (page 23 and following), address the question: whether the OSWD enables the chemical doping and bandgap engineering of graphene? This is essential as being a pre-requisite when it comes to the development of OSWD for future applications, especially in the field of carbon-based electronics. Since such a chemical doping simultaneously alters the spectroscopic properties of a material, Raman spectroscopy was incorporated for the analysis, the technique known to be a reliable and widely used method for investigating the fundamental physical properties of carbon nanomaterials [6-8,45-50]. However, as the hitherto used standard OSWD preparation technique failed to generate suitable samples for Raman analysis, the chapters as well present modifications to the approach, enabling a significant adjustment to the large-scale configuration of the generated substrate surface coverage in a scalable manner, by either incorporating a reworking step or by triggering the OSWD process thermally (and thus without employing a catalysing dispersing agent). Further, in order to verify the outcomes of the Raman analysis (and to probe the potential chemical doping of graphene), an independent, additional experimental technique, the Scanning Tunneling Spectroscopy (STS) [51-57], was employed and results subsequently presented. The chapters further provide complementary explorations that revealed the basic principles of the adsorbate layer growth. Moreover, the sections disclose that the findings of the OSWD model systems, used so far, are transferable to the substrate graphene and to an alternative semiconductor (dimethylquinacridone (DMQAC)), making the obtained results thus valid for OSWD applications in general.

Identification of the contributing physical and chemical forces and the required environmental conditions (as to provide a fundamental model of the OSWD process) marks as the aim of the chapters 2.4, titled “Revealing the Physicochemical Basis of OSWD” and 2.5, titled “Revealing the Physicochemical Basis of OSWD – Supporting Information” (page 39 and following). The relevance of the dispersing agent in triggering the OSWD is assessed and its impact on the performance of the OSWD process is studied (by applying *ceteris paribus* approaches to the OSWD model system, using both organic liquids and purified water). The coefficient of determination R^2 (square of the Pearson correlation coefficient R) was used in this regard, as to quantify the degree of a potential correlation between the achieved surface coverage and factors such as viscosity, permittivity, surface tension, or vapour pressure of the dispersing agent in use. Further, approaches to control the OSWD process are presented, addressing the properties and conditions of the dispersed γQAC crystals via modification of aqueous dispersing agents with the aid of different salts, acid, and base, thereby exploring the impact of particle size, zeta potential and pH on the OSWD. Additionally, essential insights into the OSWD process are offered that are gained by simulating the approach of a semiconductor crystal towards the substrate surface and approximating the related gradient of the surface free energy. This was achieved by using an appropriate mathematical model, based on a refined DLVO theory and incorporating the Casimir-like fluctuation-induced forces [58-66]. Besides, the geometrical interaction between a γQAC crystal and a HOPG substrate is investigated via force field calculations. Finally, a model for the OSWD is proposed describing the OSWD process in detail, considering the operating distance of the participating forces and incorporating the effect of dewetting in a hydrophobic confinement, for both the polar and the nonpolar dispersing agents [67-72].

Lastly, chapter 3., titled “Summary and Outlook” summarizes the outcomes of the present dissertation and provides an outlook by assessing the potentials of the OSWD technique.

2. Results and Discussion

2.1. Growing Low-dimensional Supramolecular Crystals

CrystEngComm

PAPER

View Article Online
View Journal | View Issue

Cite this: *CrystEngComm*, 2017, **19**, 1417

Growing low-dimensional supramolecular crystals directly from 3D particles

Alexander Eberle,[a] Adrian Nosek,[b] Johannes Büttner,[c]
Thomas Markert[d] and Frank Trixler*[ac]

Received 9th November 2016,
Accepted 6th February 2017

DOI: 10.1039/c6ce02348g

rsc.li/crystengcomm

We show that one-dimensional (1D) nanostructures and two-dimensional (2D) supramolecular crystals of organic semiconductors can be grown on substrates under ambient conditions directly from three-dimensional (3D) organic crystals. The approach does not require dissolving, melting or evaporating of the source crystals and is based on organic solid–solid wetting deposition (OSWD). We exemplify our approach by using the pigment quinacridone (QAC). Scanning tunnelling microscopy (STM) investigations show that the structures of the resulting 2D crystals are similar to the chain arrangement of the alpha and beta QAC polymorphs and are independent of the 3D source crystal polymorph (gamma). Furthermore, distinct 1D chains can be produced systematically.

Introduction

One of the most promising areas of research concerning the development of future electronic devices deals with the so-called carbon-based nanoelectronics.[1–8] In this regard, utilizing the outstanding electronic properties of graphene offers both an enhanced performance increase and the development of new electronic device types, such as flexible or inkjet printed electronics.[1–10] Further, the semiconductive parts of a carbon-based nanocircuitry can be fabricated using organic semiconductor molecules. Such 2D supramolecular arrays induce a bandgap if adhered to the graphene substrate.[6–8] Thus, the assembly of supramolecular architectures consisting of organic semiconductors *via* 2D crystal engineering is of special interest as far as the construction of functional nanosystems is concerned.[10–15] Functional nanosystems, like nano-scale transistors, are created by the self-assembling of small organic molecules *via* programmable non-covalent interactions, such as hydrogen bonding, van der Waals, π–π stacking, and electrostatic interactions.[10–15]

Today's standard technologies for the bottom-up assembly of supramolecular arrays are mainly based on either vapour deposition[16] or liquid phase deposition techniques.[17] However, processing organic semiconductors *via* vapour deposition methods, like organic molecular beam deposition,[17,18] is often challenging due to their thermal instability during the vacuum sublimation process.[19–21] Also, since most organic pigments with promising semiconductive properties are insoluble in almost all liquid media, liquid phase deposition techniques, like drop-casting or spin-coating,[19] cannot be applied without a chemical functionalization to enable the dissolution of such organic pigments.[19–21] However, the custom synthesis of functionalised semiconductors is costly and expensive, particularly in relation to the purchase prices of the standard pigments that are already being used in the industry. In contrast to the above mentioned limitations, we introduce organic solid–solid wetting deposition (OSWD)[20–22] as a novel, environment friendly, cheap, and up-scalable technology to assemble 2D supramolecular semiconductive arrays. Compared with time-consuming and expensive standard manufacturing techniques based on either vapour or liquid phase deposition, OSWD is a very straightforward technique to perform: under ambient conditions; the powdered organic semiconductor is dispersed in a dispersing agent and then drop-cast on a substrate, *e.g.* graphite, graphene or molybdenum disulphide (MoS_2). Immediately afterwards, highly ordered supramolecular arrays covering the substrate surface are formed. The self-assembly is driven by a solid–solid wetting effect,[23–25] with a gradient of the surface free energy acting as the driving force.

In this study we show that *via* the OSWD technique, 3D crystalline particles can be transformed directly into several, distinctly defined 1D and 2D supramolecular structures. We exemplify our approach using the organic semiconductor quinacridone (QAC), a cheap and commercially available

---

[a] *Department für Geo- und Umweltwissenschaften and Center for NanoScience (CeNS), Ludwig-Maximilians-Universität München, Theresienstraße 41, 80333 München, Germany. E-mail: trixler@lrz.uni-muenchen.de*
[b] *Department of Physics & Astronomy, University of California, Riverside, 900 University Ave., Riverside, CA 92521, USA*
[c] *TUM School of Education, Technische Universität München and Deutsches Museum, Museumsinsel 1, 80538 München, Germany*
[d] *Institut für Theoretische Chemie, Universität Ulm, Albert-Einstein-Allee 11, 89081 Ulm, Germany*

pigment with promising electrical properties, low toxicity, excellent physical and chemical stability and biocompatibility, for applications within the living organism.[26–32] The chemical structure of a single QAC molecule is shown in Fig. 1. The linear QAC molecules built up stable 3D crystal structures by connecting with their neighbours by four hydrogen bonds of the type NH···O═C, forming four possible polymorphs: α^{I}, α^{II}, β, and γ.[36] A detailed analysis of the related crystal structures of these polymorphs using X-ray powder diffraction was provided by Paulus *et al.*[36] and by Lincke.[37] The crystal morphology of a 3D QAC crystal, formed by the gamma quinacridone polymorph (γQAC), is shown in Fig. 2(a). Please note that, below, the abbreviation QAC is used for quinacridone in general, usually related to either quinacridone molecules or 1D as well as 2D quinacridone structures, and γQAC is used for the 3D gamma quinacridone polymorph. At standard atmospheric pressure, QAC crystals are entirely insoluble in water[33–36] as well as in common organic solvents.[28,36] As a result, so far QAC monolayers could only be assembled *via* organic molecular beam deposition in ultra-high vacuum[32] or by the use of soluble QAC derivates.[28] However, we demonstrate the direct generation of low-dimensional QAC adsorbate crystals from 3D organic crystals *via* the OSWD technology without a dissolving step and without vacuum sublimation and present a detailed structure analysis of the resulting patterns. In addition, we present results from the OSWD on various substrates, including carbon nanotubes, and show that the dispersing agent can catalyse and direct this crystallisation at the solid–solid interface. Finally, the thermal and temporal stability of the generated low-dimensional structures and the general validity of the presented results are discussed.

Results and discussion

Characterisation of the 1D and 2D crystal structures

To begin with, we characterise the crystallographic properties of different supramolecular QAC structures that have been grown atop a highly ordered pyrolytic graphite (HOPG) surface as the substrate, this being done for both the 1D chains and the 2D arrays. The structure characterisation described below is based on empirically determined parameters that have been acquired *via* the analysis of scanning tunnelling microscopy (STM) scans. Additionally, these parameters and the different types of supramolecular QAC structures presented below have been verified with the aid of force-field calculations, by simulating QAC adsorbate structures atop a graphene substrate. Initially, the QAC molecules are linked in 3D crystals; the molecular arrangement within a γQAC crystal is shown in Fig. 2(b). The OSWD process enables the detachment of molecules from an adsorbed QAC crystal. The detached molecules attach themselves to the substrate surface, where they begin to assemble new supramolecular structures. According to the functional groups of the QAC molecule, QAC builds up supramolecular chains *via* NH···O═C hydrogen bonds,[20] and multiple parallel and side-by-side appearing chains build supramolecular arrays (Fig. 2(c)). These 1D supramolecular chains and 2D arrays are shown in the simulation in Fig. 2(c) that is a result of the performed force-field calculations.

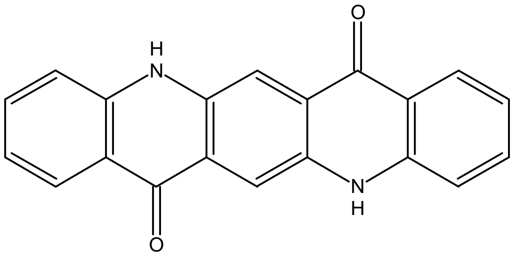

Fig. 1 Chemical structure of the QAC molecule.

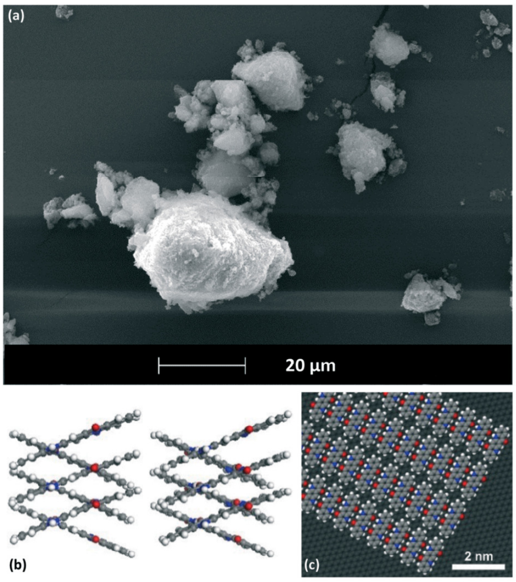

Fig. 2 (a) Scanning electron microscope picture showing the 3D crystal morphology of γQAC. (b) Model of how the QAC molecules are arranged in the γQAC polymorph. (c) Force-field calculated supramolecular structure, showing how the QAC molecules arrange themselves in 1D supramolecular chains and 2D arrays.

Examining how single QAC chains lie side by side to form an array, we observed two possible configurations: the single chains can be located directly next to each other and this condition is termed close-packing QAC chain configuration (Fig. 3, lattice vectors a and b). In addition, there is another case where varying but definite spacing among the QAC chains is observed – such a configuration is termed as the relaxed QAC chain configuration (Fig. 3, lattice vectors a′ and b′). The lattice parameters of these two configurations are:

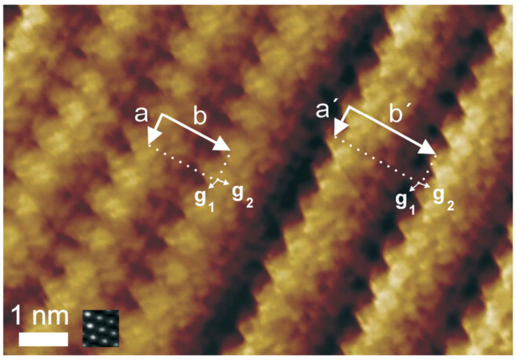

Fig. 3 STM picture of supramolecular QAC chains on a HOPG surface displaying variable interspaces. The lattice vectors a and b indicate the unit cell of the close-packing chain configuration of the QAC adsorbate, whereas a′ and b′ indicate the lattice vectors of the relaxed QAC chain configuration. The lattice vectors g_1 and g_2 of the graphite substrate are added in correct relation to the vectors of the adsorbate lattice. Inset: Auto-correlated STM image of the HOPG substrate, received directly after scanning the QAC chains.

- Close-packing QAC chain configuration:

  $|a| = 0.70 \pm 0.02$ nm; $|b| = 1.63 \pm 0.02$ nm, $\gamma = 87 \pm 1°$
- Relaxed QAC chain configuration:

  $|a'| = |a|$, $|b'| = 2.04 \pm 0.02$ nm, $\gamma = 88 \pm 1°$

Investigating the origin of the relaxed QAC chain configuration, we compared the QAC lattice vectors with the graphite lattice vectors (g_1 and g_2 in Fig. 3). For this, we used a STM picture, received directly after scanning the QAC chains (refer to Fig. 3, inset). Converting the lattice vectors of the substrate (g_1, g_2) into the lattice vectors of the adsorbates (a, b, respectively a′, b′), we obtained the following transformation matrixes:

$$\begin{pmatrix} a \\ b \end{pmatrix} = \begin{pmatrix} 10/3 & 4/3 \\ 1 & 7 \end{pmatrix} \begin{pmatrix} g_1 \\ g_2 \end{pmatrix} \qquad \begin{pmatrix} a' \\ b' \end{pmatrix} = \begin{pmatrix} 10/3 & 4/3 \\ 2 & 9 \end{pmatrix} \begin{pmatrix} g_1 \\ g_2 \end{pmatrix}$$

The lattice vectors a and a′ of the QAC adsorbates are identical multiples of the graphite vectors and are coincident with the graphite structure as a result of the strong intermolecular NH⋯O═C hydrogen bonds of the QAC chain.[20] The vectors b and b′ are whole-number multiples of the graphite vectors and thus are commensurable. The vector b indicates the smallest possible distance between two QAC chains, while the lattice vector b′ of the relaxed configuration is the next greater distance as a consequence of the crystal lattice of the graphite substrate. In the direction of the b and b′ vectors, perpendicular to the growth direction of the QAC chains, the van der Waals interactions between the QAC chain and the graphite substrate were found to exceed the van der Waals interactions between neighbouring QAC chains.[20] Greater distances between the QAC chains arise due to missing chains along the periodicity of the b or b′ vectors (Fig. 4).

Further investigations revealed that these different types of QAC chain configurations lead to the formation of three different types of QAC arrays: arrays with a high packing density (Fig. 5(a)), arrays with a low packing density (Fig. 5(b)) and loose appearing 1D QAC chains (Fig. 5(c)). The 2D QAC arrays with high packing density are the result of the close-packing QAC chain configuration. The QAC arrays with low packing density are found to be the result of either the relaxed QAC chain configuration or the absence of QAC chains.

According to Fig. 4 and 6, QAC wires as well as QAC arrays assemble not only in a parallel fashion but also in a multi-directional fashion. Analysing the Fourier transformation of various multi-directional arrays, it was further found that QAC domains assemble in six different orientations on the graphite substrate (Fig. 6). Comparing these structure details with the chain arrangements within the QAC crystal-polymorphs, they were found to be independent of their 3D crystalline source, the gamma polymorph. In fact, the 2D arrays assembled *via* OSWD seem to be similar to the alpha and beta polymorphs of the 3D QAC crystals.[36]

In rare cases, supramolecular QAC bilayers were found, arising as a 2D QAC array is built on top of another one. Further, these two-layer structures were found to occur in two different configurations: a QAC array overgrowing a contiguous QAC array with a different orientation, leading to the crisscross structure of two overlapping domains (Fig. 7(a)). Additionally, the supramolecular QAC chains forming the top layer arise straight above and parallel to the chains of the

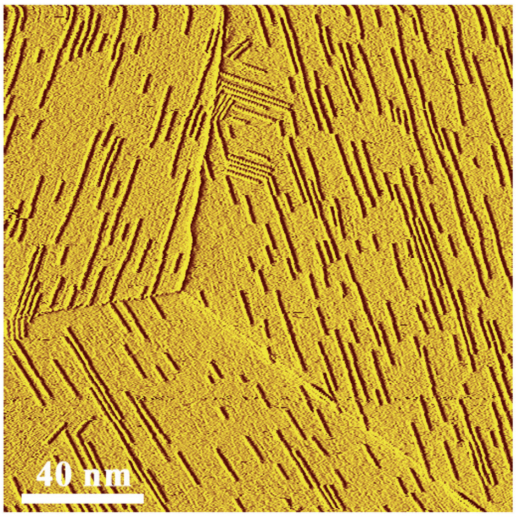

Fig. 4 STM picture of a HOPG surface that is predominantly covered by 1D QAC chains with varying gaps between them. The average coverage of the whole treated HOPG surface is 24 ± 4%. Ethylbenzene was used as the catalysing dispersing agent.

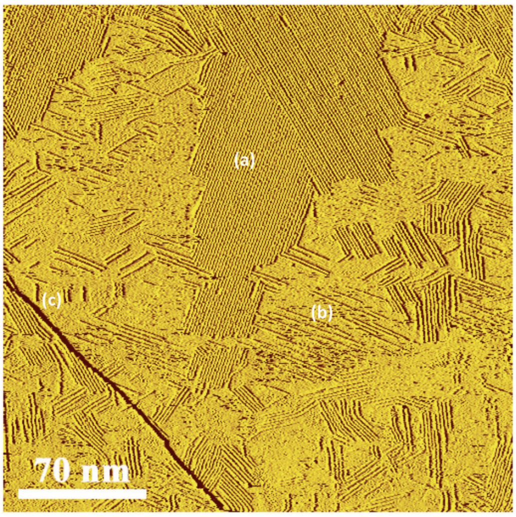

Fig. 5 STM picture of QAC arrays on a HOPG surface. The dispersing agent anisole was used to catalyse the OSWD, leading to an overall coverage of the surface by QAC arrays of 61 ± 9%. (a) QAC array with a high packing density. (b) QAC array with a low packing density. (c) 1D QAC chain.

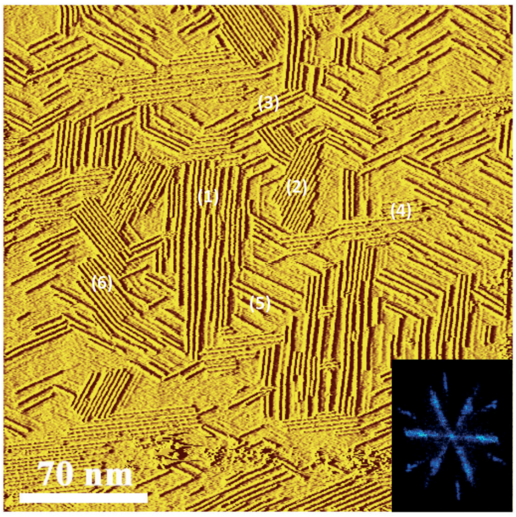

Fig. 6 The QAC arrays shown in this STM picture were assembled with the aid of the dispersing agent glycerol. The arrays occur with six different orientations that are shown in (1)–(6). The small picture in the bottom right corner shows the fast Fourier transformation of this STM picture.

bottom layer (Fig. 7(b)), resulting in a plane-parallel bilayer configuration. However, as the top layer can be easily removed using the tip of the STM, the binding energy between the top and the bottom QAC layer is supposed to be considerably lower than the binding energy between the bottom layer and the HOPG surface. Thus we propose that as the bilayers seem to be unstable and prone to mechanical stress, the STM measurement process might destroy these structures before they can be detected. So far, though we have been able to verify the occurrence of these two-layer structures using various sample preparation methods, we were still not successful in directing their growth.

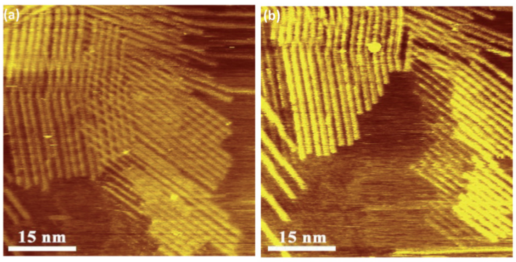

Fig. 7 (a) Supramolecular QAC bilayer in a crisscross structure of two overlapping QAC arrays. (b) Plane-parallel QAC bilayer, with the QAC chains forming the top layer being on top of and parallel to the chains of the bottom layer.

At this point, we would like to point out once more that OSWD is based on a solid–solid wetting effect, with a gradient of the surface free energy being the driving force. Referring to previous publications, we have demonstrated in detail that there are no detectable dissociated semiconductor-molecules present in the liquid phase of the dispersion in use and thus OSWD is not related to a solubility phenomenon.[20,21] Additionally, we pointed out that a 2D self-assembly from a liquid phase results in periodic structures, but the observed supramolecular structures arrange themselves in well-defined arrays, displaying varying orientations. Furthermore, if molecules are removed from an adsorbate layer and the liquid phase is still present, then the gap within the periodic structures would immediately be healed by nearby dissociated molecules. However, if a nanoscaled gap is induced in an array that was self-assembled via OSWD, then this gap remains stable and detectable for days, since the semiconductor particles within the liquid phase cannot come in contact with the substrate surface due to their considerably larger dimensions. Also, we have demonstrated that the time-dependent gap-stability decreases with an increasing gap size as a result of the increasing probability that a nearby semiconductive particle fits into the gap.

Applying the OSWD to alternative substrates: CNTs and MoS_2

The question arose as to whether the OSWD is capable of generating supramolecular structures on different kinds of substrates as well. Thus, we decided to explore whether the 1D and the 2D supramolecular QAC configurations that have been discovered so far using a HOPG substrate can also be detected on other substrates. For this, we began a series of tests using MoS_2 as the underlying substrate. The results of our investigations are illustrated in Fig. 8. As can be seen, the single QAC molecules arrange themselves again in 1D chains, with a likewise lattice vector |a| of 0.70 ± 0.02 nm. Furthermore, in analogy to our investigations using HOPGs, multiple parallel and side-by-side appearing chains form arrays displaying various orientations, however, with the distance between the single chains (vector b) being now constantly 2.15 ± 0.02 nm (Fig. 8(a) and (b)). Fast Fourier transformations further revealed six main array orientations that are likewise related to the substrate's crystal lattice. An occasionally occurring seventh orientation, as depicted in the small picture in the bottom right corner of Fig. 8(a), was revealed as well, potentially being the result of an array shift along a grain boundary of the substrate.

In an alternative approach, we tried to cover multi-walled carbon nanotubes (CNTs). We expected that as the chemical structure of the CNTs is identical to that of a HOPG, potentially occurring supramolecular QAC structures on top of them should also display similar configurations. Additionally, we wanted to verify whether the substrate surface has to be flat or if the OSWD is also applicable to nanoscale curved surface structures. As shown in Fig. 9, the OSWD was actually found to cover the CNTs with supramolecular QAC structures. Exploring the crystallographic properties of these structures revealed that the 1D QAC chains arrange themselves primarily in the close-packing QAC chain configuration. Thus, the CNTs are closely covered by a QAC monolayer. Additionally, this result underlines the high mechanical stability of the 1D and 2D QAC structures.

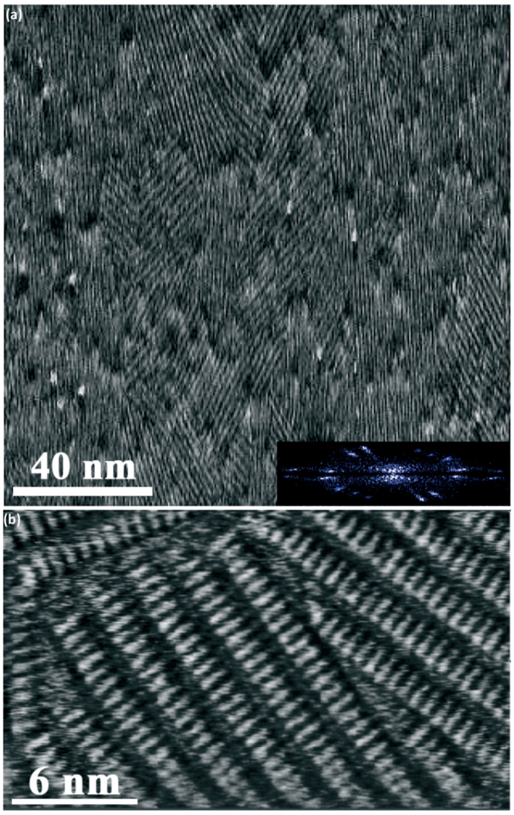

Fig. 8 (a): Overview STM scan of 2D supramolecular QAC arrays on a MoS_2 substrate. The small picture in the bottom right corner shows the related fast Fourier transformation. (b) Straightened close-up view of the overview scan, showing that the single QAC molecules arrange themselves in 1D chains. The distance between parallel QAC chains is constant. The dispersing agent used to catalyse the OSWD was octylcyanobiphenyl (8CB).

The dispersing agent determines the structure and quantity of the QAC arrays

After the determination of the three large-scale configurations of the supramolecular QAC structures (high packing density, low packing density and loose appearing 1D chains), we faced the question of whether these structures occur randomly or the probability of their occurrence is dependent on the environmental conditions.

First of all, we tried to verify if an OSWD takes place without a dispersing agent. With respect to the current model, the OSWD depends on a gradient of the surface free energy.[20–25] Hence, assuming the situation of a γQAC crystal coming in contact with a HOPG substrate, if the attractive forces towards the substrate surface exceed the binding forces within the adsorbed semiconductor crystal, then an OSWD should take place. Comparing the surface free energies of graphite (54.8 mJ m^{-2})[43] and γQAC (49.1 mJ m^{-2})[44] revealed that the binding forces within the graphite surface are

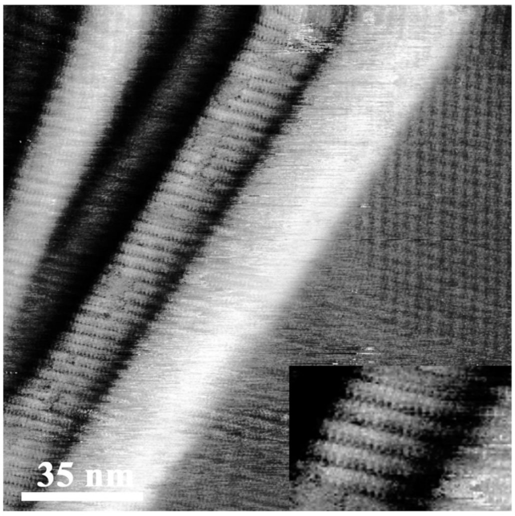

Fig. 9 STM picture of multi-walled carbon nanotubes (CNTs) that are covered by supramolecular QAC structures. The close-up view in the bottom right corner illustrates that to cover the CNTs the 1D QAC chains arrange themselves primarily in the close-packing QAC chain configuration.

stronger than those within a γQAC crystal. This fact implies that inducing an OSWD in ambient conditions could be possible without the necessity to use a dispersing agent. Thus, we linked the powdered γQAC and the HOPG substrate without a dispersing agent in a couple of approaches. However, for all of the cases tried, no QAC arrays could be detected *via* STM measurements.

Thereupon, we started a series of tests using several polar and non-polar dispersing agents with varying properties. It was observed that the selection of the dispersing agent had a great influence on the structure, size, and coverage of the assembled QAC arrays. In this regard, propylene carbonate was found to predominantly catalyse the formation of arrays with high packing density, and with an achieved coverage of 67 ± 19% it is the most powerful dispersing agent to catalyse the OSWD process detected so far (Fig. 10). Further, the individual arrays were observed to have small dimensions, as compared to the arrays when assembled with the aid of anisole (Fig. 5). However, anisole was found to not preferentially catalyse a specific array configuration, and hence arrays with a high packing density, arrays with a low packing density, and loose appearing 1D QAC chains were observed having approximately the same probability of occurrence. Using anisole, the achieved coverage rate of 61 ± 9% is still high, but lower than that observed in the case of the propylene carbonate sample.

Surprisingly, we were able to trigger the OSWD process by simply using purified water as the dispersing agent. This resulted in the building up of arrays, chiefly with a low packing density, as can be seen in Fig. 11. In contrast to the polycarbonate and anisole samples, the supramolecular QAC structures built up using purified water were seen to cover a considerably lower area of 24 ± 7%. Moreover, purified water, by far being the cheapest available dispersing agent, enables the possibility of replacing the organic dispersing agents used so far. This is a major step forward in the direction of the OSWD application for an industrial, large-scale production.

Using the dispersing agent ethylbenzene enables covering the HOPG surface predominantly with separately occurring 1D QAC chains (refer to Fig. 4). The achieved coverage of 24 ± 4% corresponds to that of the water based sample. Finally, the dispersing agent dodecane does not catalyse the formation of stable QAC structures. Sometimes, or by scanning a large area, tiny sporadically occurring 1D QAC chains can be found, as shown in Fig. 13. These structures are not stable but occur and vanish during the STM scan.

Reviewing these results, we concluded that the dispersing agents deliver activation energy to enable the OSWD process to take place. Furthermore, the dispersing agents direct the OSWD and thereby the structure, size, and coverage of the assembled QAC arrays. Thus, by using appropriate dispersing agents, it is possible to control the self-assembly of the desired 1D or 2D QAC structures in advance. However, the role of the dispersing agent is based on a complex network of diverse factors, including zeta potentials, which needs an extensive discussion and thus will be published elsewhere.

Analysing the stability of the low-dimensional structures and the general applicability of the OSWD

The results of the experiments performed to analyse the nature of OSWD generated adsorbate structures also enabled

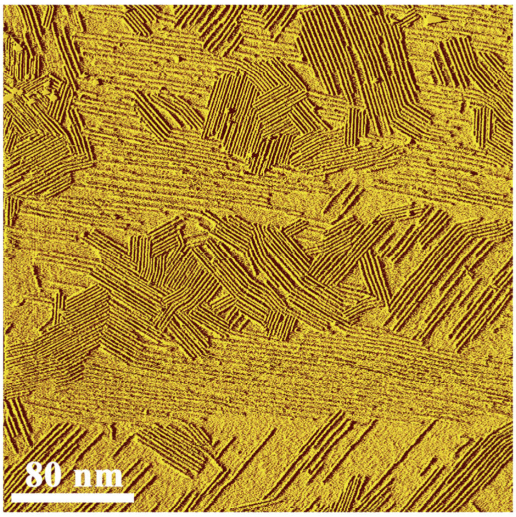

Fig. 10 STM picture of a HOPG substrate, displaying a surface coverage by QAC structures of 67 ± 19%. Predominant are arrays with a high packing density, the other array configurations hardly occur. Propylene carbonate was used as the catalysing dispersing agent.

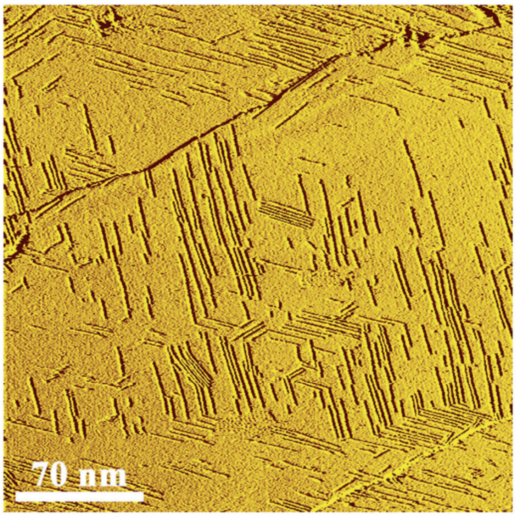

Fig. 11 STM picture of a HOPG substrate with supramolecular QAC arrays atop, displaying mainly a low packing density. Purified water was used as the dispersing agent. The overall surface coverage is 24 ± 7%.

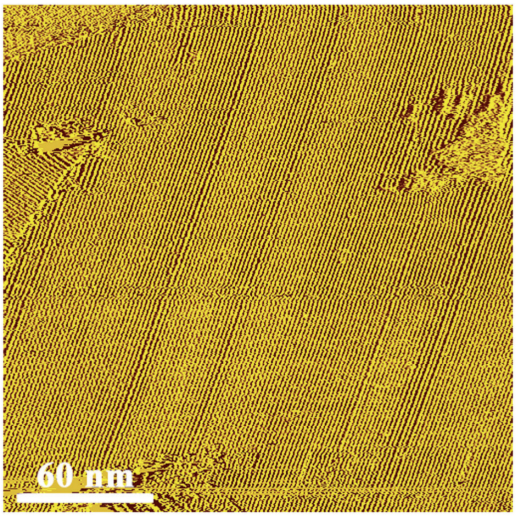

Fig. 12 QAC adsorbate structures that have been grown by heating pure γQAC powder on a HOPG to 240 °C. The surface coverage rate is 83 ± 14%.

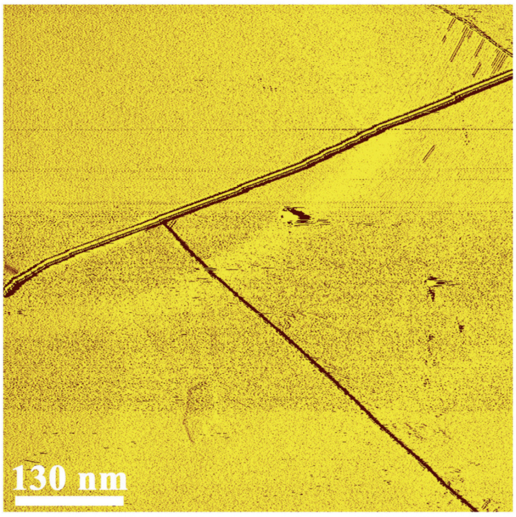

Fig. 13 STM picture of a HOPG surface treated with a dispersion of γQAC and the dispersing agent dodecane. No 2D QAC arrays could be found.

estimation of their temporal as well as thermal stability. First, the OSWD is performed under ambient conditions and so are the STM measurements used for the sample analysis. This indicates that the structures are generally resistant to moderate electric fields, as they are applied by the STM, and to humidity. The resistance to water in general is confirmed by the fact that water can be used as an OSWD catalysing dispersing agent. Previously published test results further show that 2D perylenetetracarboxylicdianhydride (PTCDA) arrays generated *via* OSWD do not change their design within a period of at least 3 days.[21] In addition, the QAC samples in this study have been analysed *via* STM for up to 7 days, revealing no changes in design or surface coverage. By exploring the thermal stability, it was found that heating samples up to 160 °C in the presence of different dispersing agents has no observable effect on the overall design of the QAC adsorbate layer. Further tests revealed that heating pure γQAC powder on a HOPG substrate up to at least 240 °C thermally triggers OSWD processes, leading to an overall surface coverage rate of 83 ± 14% (Fig. 12). The related samples were again analysed *via* STM after 36 days, still showing no decomposition of the QAC adsorbates. Summing up, the adsorbate structures generated *via* OSWD present themselves to resist temperatures up to at least 240 °C and to have a life span of at least several weeks.

Although the results presented so far were obtained by using a QAC example system, we would like to clarify that the OSWD is able to process a number of different organic semiconductors such as perinone, flavanthrone, indanthrone, and MePTCDI as well as PTCDA and acridone.[21,47]

Conclusions

Our investigations successfully offered insight into the basic principles and the control capabilities of OSWD technology. We were able to show that OSWD enables the assembly of 1D and 2D supramolecular architectures directly from the corresponding 3D crystals. The crystal structures and the lattice parameters of the various QAC array configurations were determined and their dependency on the substrate surface was revealed. Further, we were able to verify that the OSWD is applicable to graphite and MoS_2 substrates. Additionally, supramolecular QAC structures assembled *via* OSWD are mechanically stable enough to cover the nanoscale curved surface structure of CNTs.

Working under ambient conditions, the whole OSWD process is driven by the catalysing dispersing agent. Based on our results, we were able to induce the OSWD using low-cost organic dispersing agents as well as employing purified water. Further, the results indicated that the properties and conditions within the dispersion direct the OSWD and thereby the design and the coverage of the assembled supramolecular structures. Thus, it can be said that the OSWD process can be controlled by choosing the right dispersing agent. In addition, the 1D QAC chains and the 2D arrays form a far-ranging periodic pattern, again dependent on the dispersing agent in use. Such a pattern in turn can be found wherever the dispersion wets the underlying graphite substrate. Hence, the OSWD process can be directed locally and globally, paving a way for a scale up.

In addition, it was found that the generated adsorbate structures are temporally and thermally stable. Further, it can be said that the QAC arrays are chemically and mechanically resistant[26–32] and can be built up within minutes or even seconds.[20,21] Additionally, previous investigations have shown that alkyd resin can be used to seal a QAC adsorbate layer, providing a resistant protection layer without damaging the supramolecular structures.[20] Estimating the potentials of the OSWD technology, the above results point towards an industrial application to produce low-cost products using large-scale production technologies, like printed and potentially flexible carbon based electronics,[9] or highly efficient systems to capture carbon dioxide.[45] In particular, by using water as a dispersing agent, all kinds of non-toxic applications, such as in living organisms or in the food industry, are imaginable.

Experimental section

Force-field calculations

The calculations were performed using the Cerius2 software package employing a Dreiding II force-field,[46] which contains an explicit term for hydrogen bonding. Geometrical constraints were derived from STM measurements and applied to these simulations.

Scanning electron microscope measurements

The corresponding measurements were performed using a 440i scanning electron microscope from Zeiss; the chief scan settings were a working distance of either 3 or 5 mm and an extra-high tension of 20.00 kV. Further, an SE1 detector was used for such measurements.

STM sample preparation and scan setting

To prepare a standard scanning tunnelling microscope (STM) sample, using a dispersion with 2 wt% pigment, γQAC (purchased as Hostaperm Red E5B02 from Clariant) was dispersed in 4 ml of the desired dispersing agent. The dispersing agents used were anisole (from Sigma Aldrich, item no. 10520), ethylbenzene (from Sigma Aldrich, item no. 03080), glycerol (from Alfa Aesar, item no. A1620), propylene carbonate (from Sigma Aldrich, item no. 310328), 8CB (purchased as 4′-*n*-octylbiphenyl-4-carbonitrile from Alfa Aesar, item no. 52709-84-9), and purified water. First, a few drops of the dispersion were dispensed on a highly ordered pyrolytic graphite (HOPG, purchased from NT-MDT, item no. GRBS/1.0). In continuative tests, either molybdenum disulphide (MoS_2, from Climax Molybdenum Company) or multi-walled carbon nanotubes (CNTs, from ABCR, item no. AB 255407) as alternative substrates were used. The CNTs were dispersed and ultrasonicated in toluene for 60 minutes. Next, the CNT-dispersion was added dropwise to a HOPG substrate. After the toluene was completely vaporised (verified in additional STM measurements), the substrate was treated with a γQAC dispersion in the manner as already described.

If the dispersing agent did not vaporize after an exposure time of 10–20 minutes, the HOPG was dried using a special hotplate, enabling accurate temperature control and providing a smooth temperature increase (Stuart SD160, temperature accuracy ±1.0 °C). Once the sample was dried, it was immediately taken off the hotplate. Note, that all dispersing agents vaporized below 160 °C, besides glycerol (235 °C). Heating pure γQAC powder to 160 °C without a dispersing agent does not induce an OSWD. To create 2D QAC arrays without a dispersing agent was only possible by heating pure γQAC powder to 240 °C. Thus, so far we were unable to explore how the high evaporation temperature of glycerol influences the created QAC arrays. Note that the dispersing agent 8CB was not removed, *i.e.* the corresponding samples have not been dried because 8CB does not disturb the STM measurement.

The ready-made STM samples were investigated within days; as per the previous tests, QAC arrays were revealed to not change their structure for a minimum of four weeks, provided they are not influenced *via* any external forces. For the STM measurements, we used a home-built STM combined with a SPM 100 control system supplied by RHK Technology. The scan settings were bias = 1 V, tunnel current = 300 pA, and the line time = 50 ms. Further, the voltage pulses used to improve the scan quality were located in the range between 4.3 and 10 V. For the STM measurements being performed under ambient conditions, a thin layer of dodecane (purchased from Sigma Aldrich, item no. D221104) was generally applied on top of the HOPG surface to increase the measurement quality.[41] Extensive tests revealed that a mixture of dodecane and γQAC, without another dispersing agent, was unable to generate two-dimensional QAC structures (Fig. 13) and that the dodecane by itself could not form supramolecular assemblies at room temperature.[42] In addition, to conduct a STM measurement under ambient conditions without dodecane was very challenging, mainly due to the occurrence of a thin contamination layer of adsorbed water on top of the HOPG surface,[38–40] which otherwise was found to be successfully removed using the hydrophobic dodecane.

Determining the coverage

To determine the coverage of the HOPG surface by the QAC arrays within a single STM picture, the software program Gwyddion (64 bit), version 2.42, was used. For this, initially, the QAC arrays *via* the tool "Mask Editor" were highlighted followed by the export of single array dimensions using the tool "Grain distributions", finally accompanied by Microsoft Excel 2013 (version 15.0.4667.1002) calculations to determine the coverage ratio. Further, to investigate the average coverage of a STM sample, we analyzed per sample an area of 0.63 ± 0.24 μm^2 using a number of STM pictures with high scan resolution and without measurement artefacts; the average coverage rates including the double standard deviations are specified in the current study. Calculations revealed high double standard deviations, indicating the dependence of the coverage by QAC arrays on different positions of a STM sample. Nevertheless, the average coverage rates of different samples treated with different dispersing agents were observed to differ significantly higher in value.

Fast Fourier transform

Fast Fourier transform was done using the Fourier processing tool of the software SPIP (Scanning Probe Image Processor, Version 2.3000; distributor: Image Metrology ApS).

Acknowledgements

The authors would like to thank Ms. Neeti Phatak for proofreading and helping us with the English language. Further, the Bayerisches Staatsministerium für Umwelt und Verbraucherschutz is gratefully acknowledged for their funding.

Notes and references

1 P. Avouris, Z. Chen and V. Perebeinos, *Nat. Nanotechnol.*, 2007, **2**, 605–615.
2 W. Lu and C. M. Lieber, *Nat. Mater.*, 2007, **6**, 841–850.
3 T. Jain and T. Agrawal, *Int. J. Comput. Sci. Inf. Technol.*, 2013, **4**, 477–480.
4 H.-H. Chen, S. H. Su, S.-L. Chang, B.-Y. Cheng, S. W. Chen, H.-Y. Chen, M.-F. Lin and J. C. A. Huang, *Sci. Rep.*, 2015, **5**, 11623.
5 S. Tans, A. Verschueren and C. Dekker, *Nature*, 1998, **672**, 669–672.
6 H. Medina, Y. C. Lin, D. Obergfell and P. W. Chiu, *Adv. Funct. Mater.*, 2011, **21**, 2687–2692.
7 A. K. Manna and S. K. Pati, *Chem. - Asian J.*, 2009, **4**, 855–860.
8 B. Long, M. Manning, M. Burke, B. N. Szafranek, G. Visimberga, D. Thompson, J. C. Greer, I. M. Povey, J. MacHale, G. Lejosne, D. Neumaier and A. J. Quinn, *Adv. Funct. Mater.*, 2012, **22**, 717–725.
9 S. Park, M. Vosguerichian and Z. Bao, *Nanoscale*, 2013, **5**, 1727–1752.
10 N. Liu, Y. Zhou, N. Ai, C. Luo, J. Peng, J. Wang, J. Pei and Y. Cao, *Langmuir*, 2011, **27**, 14710–14715.
11 N. Liu, Y. Zhou, L. Wang, J. Peng, J. Wang, J. Pei and Y. Cao, *Langmuir*, 2009, **25**, 665–671.
12 J. Y. Zheng, Y. Yan, X. Wang, Y. S. Zhao, J. Huang and J. Yao, *J. Am. Chem. Soc.*, 2012, **134**, 2880–2883.
13 G. Yu and C. M. Lieber, *Pure Appl. Chem.*, 2010, **82**, 2295–2314.
14 M. Koepf, F. Chérioux, J. A. Wytko and J. Weiss, *Coord. Chem. Rev.*, 2012, **256**, 2872–2892.
15 B. J. Jordan, Y. Ofir, D. Patra, S. T. Caldwell, A. Kennedy, S. Joubanian, G. Rabani, G. Cooke and V. M. Rotello, *Small*, 2008, **4**, 2074–2078.
16 M. Liu, Z. Ji and L. Shang, in *Nanotechnology*, Nanostructured Surfaces, ed. L. Chi, WILEY-VCH, Weinheim, 2010, ch. 1.3, vol. 8, pp. 17–35.
17 D. Zhong, H. Zhang and L. Chi, in *Nanotechnology*, Nanostructured Surfaces, ed. L. Chi, WILEY-VCH, Weinheim, 2010, ch. 9.2.4, vol. 8, pp. 357–369.
18 S. Kowarik, A. Gerlach and F. Schreiber, *J. Phys.: Condens. Matter*, 2008, **20**, 184005.
19 M. Treier, E. Orgiu, L. Zalewski, D. Cho, R. Rieger, K. Müllen and P. Samorì, *J. Mater. Chem.*, 2010, **20**, 9018.
20 F. Trixler, T. Markert, M. Lackinger, F. Jamitzky and W. Heckl, *Chem. – Eur. J.*, 2007, **13**, 7785–7790.
21 F. Trixler and W. M. Heckl, in *Modern Research and Educational Topics in Microscopy*, ed. A. Méndez-Vilas and J. Diaz, Formatex, Badajoz, 2007, vol. 2, pp. 534–541.
22 J. A. A. W. Elemans, S. Lei and S. De Feyter, *Angew. Chem., Int. Ed.*, 2009, **48**, 7298–7333.
23 J. Haber, T. Machej and T. Czeppe, *Surf. Sci.*, 1985, **151**, 301–310.
24 J. Leyrer, R. Margraf, E. Taglauer and H. Knözinger, *Surf. Sci.*, 1988, **201**, 603–623.
25 F. Bertinchamps, C. Grégoire and E. M. Gaigneaux, *Appl. Catal., B*, 2006, **66**, 1–9.
26 E. D. Głowacki, R. R. Tangorra, H. Coskun, D. Farka, A. Operamolla, Y. Kanbur, F. Milano, L. Giotta, G. M. Farinola and N. S. Sariciftci, *J. Mater. Chem. C*, 2015, 6554–6564.
27 E. D. Głowacki, G. Romanazzi, C. Yumusak, H. Coskun, U. Monkowius, G. Voss, M. Burian, R. T. Lechner, N. Demitri, G. J. Redhammer, N. Sünger, G. P. Suranna and S. Sariciftci, *Adv. Funct. Mater.*, 2014, 1–12.
28 M. Sytnyk, E. D. Głowacki, S. Yakunin, G. Voss, W. Schöfberger, D. Kriegner, J. Stangl, R. Trotta, C. Gollner, S. Tollabimazraehno, G. Romanazzi, Z. Bozkurt, M. Havlicek, N. S. Sariciftci and W. Heiss, *J. Am. Chem. Soc.*, 2014, **136**, 16522–16532.
29 E. D. Głowacki, M. Irimia-Vladu, M. Kaltenbrunner, J. Gsiorowski, M. S. White, U. Monkowius, G. Romanazzi, G. P. Suranna, P. Mastrorilli, T. Sekitani, S. Bauer, T. Someya, L. Torsi and N. S. Sariciftci, *Adv. Mater.*, 2013, **25**, 1563–1569.
30 E. D. Glowacki, L. Leonat, G. Voss, M. Bodea, Z. Bozkurt, M. Irimia-Vladu, S. Bauer and N. S. Sariciftci, *Organic Semiconductors in Sensors and Bioelectronics IV*, 2011, vol. 8118, p. 81180M.
31 E. D. Głowacki, M. Irimia-Vladu, S. Bauer and N. S. Sariciftci, *J. Mater. Chem. B*, 2013, **1**, 3742.
32 T. Wagner, M. Györök, D. Huber, P. Zeppenfeld and E. D. Głowacki, *J. Phys. Chem. C*, 2014, **118**, 10911–10920.
33 K. Sue, T. Usami, K. Arai, H. Kasai, H. Nakanishi and T. Hiaki, *J. Chem. Eng. Data*, 2007, **52**, 714–717.
34 S. De Feyter, A. Gesquière, F. C. De Schryver, U. Keller and K. Müllen, *Chem. Mater.*, 2002, **14**, 989–997.
35 U. Keller, K. Müllen, S. De Feyter and F. C. De Schryver, *Adv. Mater.*, 1996, **8**, 490–493.
36 E. F. Paulus, F. J. J. Leusen and M. U. Schmidt, *CrystEngComm*, 2007, **9**, 131–143.
37 G. Lincke, *Dyes Pigm.*, 2000, **44**, 101–122.
38 Y. A. Hong, J. R. Hahn and H. Kang, *J. Chem. Phys.*, 1998, **108**, 4367.
39 G. Nagy, *J. Electroanal. Chem.*, 1996, **409**, 19–23.

40 G. Nagy, *Electrochim. Acta*, 1995, **40**, 1417–1420.

41 H. J. Räder, A. Rouhanipour, A. M. Talarico, V. Palermo, P. Samorì and K. Müllen, *Nat. Mater.*, 2006, **5**, 276–280.

42 J. Cousty and L. Pham Van, *Phys. Chem. Chem. Phys.*, 2002, **5**, 599–603.

43 S. Wang, Y. Zhang, N. Abidi and L. Cabrales, *Langmuir*, 2009, **25**, 11078–11081.

44 S. Wu and K. J. Brzozowski, *J. Colloid Interface Sci.*, 1971, **37**, 686–690.

45 D. H. Apaydin, E. D. Głowacki, E. Portenkirchner and N. S. Sariciftci, *Angew. Chem., Int. Ed.*, 2014, **53**, 6819–6822.

46 S. L. Mayo, B. D. Olafson and W. A. I. Goddard, *J. Phys. Chem.*, 1990, **101**, 8897–8909.

47 F. Trixler, *Curr. Org. Chem.*, 2013, **17**, 1758–1770.

2.2. Doping Graphene via Organic Solid-Solid Wetting Deposition

Carbon 125 (2017) 84–92

Contents lists available at ScienceDirect

Carbon

journal homepage: www.elsevier.com/locate/carbon

Doping graphene via organic solid-solid wetting deposition

Alexander Eberle [a], Andrea Greiner [a], Natalia P. Ivleva [b], Banupriya Arumugam [c], Reinhard Niessner [b], Frank Trixler [a, d, *]

[a] *Department of Earth and Environmental Sciences and Center for NanoScience (CeNS), Ludwig-Maximilians-Universität München, Theresienstraße 41, 80333 München, Germany*
[b] *Institute of Hydrochemistry, Chair for Analytical Chemistry, Technische Universität München, Marchioninistr. 17, 81377 München, Germany*
[c] *Institute for Nanoelectronics, Technische Universität München, Theresienstrasse 90, 80333 München, Germany*
[d] *TUM School of Education, Technische Universität München and Deutsches Museum, Museumsinsel 1, 80538 München, Germany*

ARTICLE INFO

Article history:
Received 24 March 2017
Received in revised form
7 August 2017
Accepted 11 September 2017
Available online 13 September 2017

ABSTRACT

Organic Solid-Solid Wetting Deposition (OSWD) enables the fabrication of supramolecular architectures without the need for solubility or vacuum conditions. The technique is based on a process which directly generates two-dimensional monolayers from three-dimensional solid organic powders. Consequently, insoluble organic pigments and semiconductors can be made to induce monolayer self-assembly on substrate surfaces, such as graphene and carbon nanotubes, under ambient conditions. The above factuality hence opens up the potential of the OSWD for bandgap engineering applications within the context of carbon based nanoelectronics. However, the doping of graphene via OSWD has not yet been verified, primarily owing to the fact that the classical OSWD preparation procedures do not allow for the analysis via Raman spectroscopy – one of the main techniques to determine graphene doping. Hence, here we describe a novel approach to induce OSWD on graphene leading to samples suitable for Raman spectroscopy. The analysis reveals peak shifts within the Raman spectrum of graphene, which are characteristics for p-type doping. Additional evidence for chemical doping is found via Scanning Tunneling Spectroscopy. The results open up a very easily applicable, low-cost, and eco-friendly way for doping graphene via commercially available organic pigments.

1. Introduction

Nearly a decade ago, it became evident that the miniaturisation of silicon-based electronics is limited and that it will soon reach its termination [1,2]. As a result, numerous scientists began exploring the prospects of carbon-based nanoelectronics, to utilise the outstanding electronic properties of graphene, and thus to increase the performance of existing and to develop future electronic devices like the flexible or inkjet-printed electronics [2–10]. However, a deeper insight revealed the production of functional nanosystems, like the nanoscale transistors, to be quite a challenging task [10–14]. A promising approach nonetheless, for the fabrication of essential semiconductive sub-regions, came forward as providing a bandgap to the graphene substrate, by covering it with a monolayer of an organic semiconductor [6–8]. Such a monolayer, in turn, can be built up by the bottom-up technologies (as the mostly available the vapor deposition- [15] or the liquid phase deposition- [16] techniques), directing the self-assembly of organic molecules via the non-covalent interactions (hydrogen bonding, Van-der-Waals, $\pi-\pi$ stacking, and electrostatics) [10–14].

However, the processing of organic semiconductor and pigment molecules imposes its own limitations: only few of these compounds survive the thermally enforced vacuum sublimation unscathed that is necessary to apply vapor deposition methods, as the organic molecular beam deposition technique [16–18]. Further, as most of the organic pigments with promising semiconductive properties are insoluble in common liquids, liquid phase deposition techniques like the drop-casting or spin-coating [18] call for an additional chemical functionalisation [18–21]. Nevertheless, in relation to the standard pigments employed usually in the industrial sector, the custom synthesis of functionalized semiconductors marks as an extensive and cost-intensive process.

As an alternative approach, we hence developed the Organic Solid-Solid Wetting Deposition (OSWD) technology, an

---

* Corresponding author. TUM School of Education, Technische Universität München and Deutsches Museum, Museumsinsel 1, 80538 München, Germany.
E-mail address: trixler@lrz.uni-muenchen.de (F. Trixler).

http://dx.doi.org/10.1016/j.carbon.2017.09.043

environmental friendly, cheap, up-scalable, and both, straightforward and quick to perform procedure [19–22]. The OSWD being based on the solid-solid wetting effect [23–25], it is the gradient of surface free energy that acts as the prime driving force behind the technology. Briefly summarizing its basics, it can be said that the surface free energy of organic semiconductor crystals that physically contact an inorganic substrate like graphite, graphene, carbon nanotubes or MoS_2 [20], gets modified when appropriate organic or aqueous dispersing agents are used. As a consequence, a solid-solid wetting process is triggered, detaching semiconductor molecules from the attached crystal and adsorbing them to the substrate surface. Subsequently, the adsorbed molecules assemble into supramolecular architectures, covering the substrate surface [19–21].

However, in this regard, worth investigating was, if the OSWD generated surface coverage dopes the graphene substrate and thus induces a bandgap. Since a bandgap alters the spectroscopic properties of a material, such a modification, if induced, can be detected via the Raman spectroscopic analysis [6–8]. Raman spectroscopy has been known as a fast and a non-destructive high-resolution technique, which can be employed to study the fundamental physical properties of carbon nanomaterials, such as determining their layer thickness, detecting structural defects, and verifying graphene doping [6,34–39]. It can thus be said to be a reliable and widely used method for investigating the doping of graphene. However, in order to perform an accurate Raman measurement, the substrate surface needs to be covered with adsorbate layers, freely accessible for the laser beam and featuring homogeneity of the order of few hundred nanometres magnitude. Unfortunately, the hitherto used standard OSWD preparation technique fails to generate such a covering, thereby calling for a modification of the approach.

Hence, in an attempt to modify the OSWD technique for gaining samples suitable for the Raman spectroscopy analysis, a series of experimental tests were performed, their results being presented and discussed in the following sub-sections. In this regard, initial efforts were made to enhance the surface coverage of the sample substrate by incorporating a reworking step. Furthermore, a new ‘thermally triggered’ sample preparation technique was tested and is put forward, with an aim of potentially triggering the OSWD process without employing a catalysing dispersing agent. Post successful generation of suitable Raman samples, the results of the Raman spectroscopy analyses are discussed, as to determine whether the OSWD produced supramolecular surface covering modifies the substrate's electronic properties by providing a bandgap or not. Finally, the results of a series of Scanning Tunneling Spectroscopy (STS) tests are presented, as to verify the outcomes of the Raman analysis via an independent, additional experimental technique. STS is especially suited in this regard, owing to its sensitivity in probing the chemical doping of graphene, by providing an atomic resolution analysis of the local electronic properties of a surface [26–32].

2. Results and discussions

2.1. Refinement of the standard sample preparation method by incorporating a reworking step

As per the results of the previous investigations, the substrate surface coverage generated via the OSWD can be altered to a large extent by substituting the dispersing agent in use, i.e. without replacing the organic semiconductor itself [20]. Until now, for the samples fabricated via the standard preparation method, the maximum achievable surface coverage rate was limited to approx. 67%, not being sufficient enough for the execution of Raman spectroscopy measurements. Thus, to accomplish such analysis and to enhance the surface coverage of the ‘traditionally prepared’ samples, the incorporation of a reworking procedure was considered. For this, and to explore the physio-chemical basics of the OSWD process, model systems out of highly oriented pyrolytic graphite (HOPG) as the substrate material, and the organic semiconductive pigment gamma quinacridone (γQAC) as the active phase were utilized. γQAC is known to be a cheap and commercially available pigment with promising electrical properties, low toxicity, an excellent physical and chemical stability, and with biocompatibility for applications in the living organism [40–46]. Furthermore, the gamma polymorph has been known to be the most stable out of the four possible, three-dimensional crystal structures, this polymorph being built up by the linear QAC molecules (refer Fig. 1 (a)) connected with their neighbours via four hydrogen bonds of the type NH···O=C [47]. Presuming the successful processing of three-dimensional γQAC crystals into substrate surface adsorbate structures through the OSWD approach, the quinacridone molecules (QAC) have been investigated to arrange themselves in one-dimensional supramolecular chains via the NH···O=C hydrogen bonds. Further, multiple parallel and side-by-side appearing chains have been reported to form supramolecular arrays (refer Fig. 1 (b)) [19,20]. Note: the abbreviation QAC is used for quinacridone in general, usually relating to either quinacridone molecules or quinacridone adsorbate structures, whereas the term γQAC is employed for the 3D gamma polymorph of quinacridone.

Force field calculations in this respect revealed that a γQAC crystal comprises of at least one crystal face, in which the QAC molecules have binding energy less than the binding energy of a molecule adsorbed on a graphene substrate [19]. From these calculations, it can be hence deduced that only on the condition that the γQAC crystal contacts the HOPG with one of its energetically favourable crystal faces, QAC molecules can detach and subsequently attach themselves to the HOPG substrate and thus initiate the self-assembly processes. In addition, experiments revealed that a complete coverage of the HOPG surface by the supramolecular QAC arrays could not be achieved, although the standard sample preparation technique covers the entire HOPG surface with a distinct layer of γQAC crystals (i.e. γQAC powder) (refer Fig. 2 (a)). From the above theoretical and experimental results, it can hence be deduced that the OSWD approach is an anisotropic process. The latter deduction, in turn, proposes a way of subsequently increasing the surface coverage of the sample, by gently rubbing the remaining γQAC powder against it. Such a procedure, supposedly, forces the γQAC crystals to roll over the HOPG surface, thereby significantly increasing the chances of specific crystal faces to contact the HOPG.

For the execution of the above, the virgin HOPGs were hence initially treated with a dispersion of γQAC and the dispersing agent octylcyanobiphenyl (8CB), the latter is known to be one of the few dispersing agents that neither does vaporise at room temperatures nor disturbs the STM measurements (further information on the 8CB's chemical structure and its ability to self-assemble stable and well-ordered arrays being available in the supplementary data). Subsequent STM measurements of the samples prepared in the above manner revealed an overall surface coverage of 50 ± 4%, including twice the standard deviation (refer Fig. 2 (a)). Thereinafter, using a metal spatula, the remaining γQAC powder was gently rubbed against the substrate, and consequently the results depict a greater overall surface coverage of 98 ± 2% (refer example picture in Fig. 2 (b)). Hence, it can be said that the incorporated reworking step enabled almost complete surface coverage, though the surface covering displayed still various arrays with different orientations. Therefore, since the substrate surface covering obtained by the above sample preparation procedure does not exhibit homogeneity of the order of magnitude of a few hundred nanometres, the above

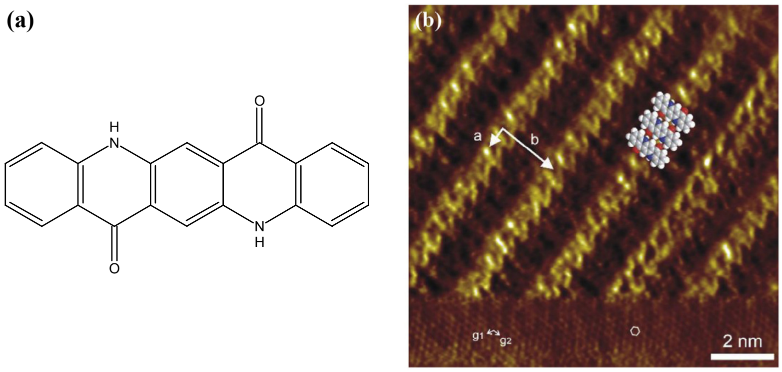

Fig. 1. OSWD induced monolayer self-assembly of QAC on graphene. (a) Chemical structure of the QAC molecule. (b) Upper section: supramolecular QAC structures situated atop single layer graphene on copper as the substrate, with the observed structures having lattice parameters as: a = 0.72 ± 0.02 nm, b = 2.06 ± 0.02 nm, and an intermediate angle of 89 ± 2°. Further, the superimposed inlay on the QAC structures (little right of the image) depicts the arrangement of single QAC molecules in one-dimensional chain-like structures. The bottom of the image, in addition, presents the underlying graphene substrate's structure, with lattice parameters of the graphene unit cell as: g1 = g2 = 0.246 nm. Besides, the white marked hexagon in the image (atop the graphene substrate) represents one carbon ring of the graphene structure, with an atom to atom distance of 0.142 nm.

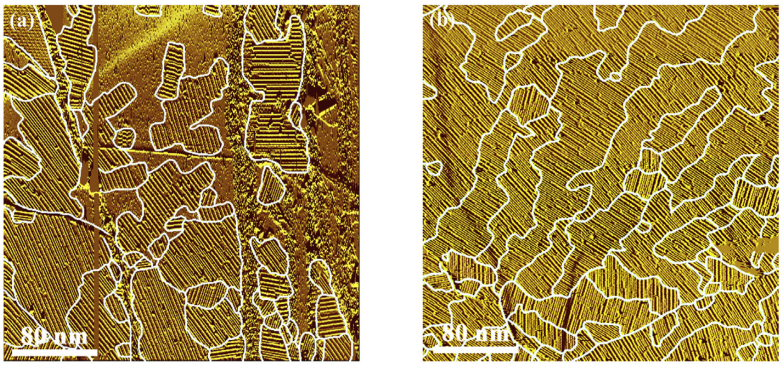

Fig. 2. Large-area STM scans of supramolecular QAC arrays (white markings highlighting the borders of the QAC arrays). (a) Example STM image of a supramolecular surface covering, atop a HOPG substrate, generated using a dispersion of γQAC and 8CB as the dispersing agent; the average surface coverage rate being 50 ± 4%. (b) Example STM image post gently rubbing the remaining γQAC powder with 8CB being still present; the average surface coverage in this case being 98 ± 2%.

sample preparation method cannot be hence used to prepare samples suited for accurate Raman spectroscopy measurements.

2.2. Triggering the OSWD without a catalysing dispersing agent

Since all attempts to rework samples fabricated by the standard OSWD sample preparation method did not lead to sufficient Raman samples, it was hence thought upon to develop a new and adequate sample preparation technique that could supply and transfer the essential activation energy to trigger the OSWD in an alternative way, i.e. without the need of a catalysing dispersing agent. A way of doing so, as per literature, could be by employing the concept that the gradient of surface free energy at the solid-solid interface changes with an increase in temperature [50,51], thereby presenting the possibility of triggering the solid-solid wetting effect via a thermal sample treatment [23–25]. However, for implication of such a treatment, the thermal stability and the melting point of the involved pigment has to be taken into account. Since QAC crystals are thermally stable up to their melting point of 390 °C [46,52], a series of tests were performed where the virgin HOPGs covered with pure γQAC powder were heated up gently to different temperatures, as to trigger the OSWD process thermally. Results in this respect revealed, though generation of no supramolecular QAC structures for temperatures up to 160 °C, however, the detection of a significant surface coverage of 83 ± 13% for samples being further heated up to 240 °C (refer Fig. 3). In addition, it was observed that the supramolecular QAC chains arranged themselves in a large-scale homogeneous monolayer, which changed its orientation almost exclusively by hitting the border to a new graphite plane. Such planes, in turn, are predetermined by the quality of the substrate surface. Further experiments were performed in this regard, where several HOPGs covered with γQAC powder were heated up to approx. 270 °C, yielding a greater surface coverage of 92 ± 6%. Hence, it can be concluded that the above described thermally triggered sample preparation method marks as a promising approach towards fabricating samples, enabling accurate Raman spectroscopy measurements.

In order to determine the underlying formation mechanism that results in the observed extended and well-ordered QAC adsorbate layers, worth recapitulating, initially, are the so far gained findings about the classical OSWD sample preparation. Summarizing briefly, when a three-dimensional semiconductor crystal contacts a HOPG substrate, molecules from the crystal detach and get attached to the substrate, provided the adsorption energy E_a is higher than the

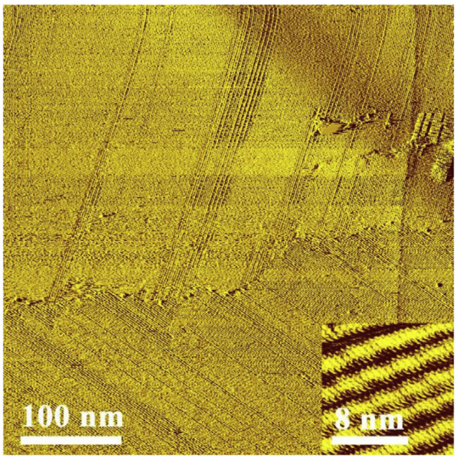

Fig. 3. STM image of a HOPG substrate covered with a QAC monolayer. The sample was prepared by heating up dry γQAC powder on the HOPG substrate to a temperature of 240 °C; the surface coverage rate being 83 ± 13% in this case. The close-up view in the bottom right corner highlights, how the QAC molecules arrange themselves within the adsorbate layer.

cohesive energy E_c of the semiconductor bulk (as derived from force field calculations in previous studies [19]). In this respect, having analyzed HOPG samples via STM measurements over a period of several weeks (with semiconductor particles and 8CB being continuously present), no significant increase in the array dimensions could be detected over time. Further, except few results showing instable bilayer structures, no case of three-dimensional growth could be detected [20]. In this regard, an approximate energetic criterion was found to predict two-dimensional vs. three-dimensional growth under conditions of thermodynamic equilibrium [53,54]: the condition for the three-dimensional growth being $E_c < E_a$ and the inverse being true for the two-dimensional growth. Hence, it can be said that for the HOPG and γQAC model system as used in the present study, growth of two-dimensional morphology is expected to be favoured, what corresponds to our findings.

Generally speaking, the growth of a supramolecular surface adsorbate structures is proportional to the surface diffusion. Surface diffusion was observed for both single adsorbate molecules and compact adsorbate clusters containing numerous molecules [54], provided the diffusion barrier is overcome. Further, the surface diffusion process is thermally promoted, just as in the case of bulk diffusion, with diffusion rates (corresponding to the adsorbate mobility) increasing with increasing temperature. We can thus conclude from our experimental findings that the surface diffusion is limited in the temperature range of up to 160 °C, whereas significant diffusion is achieved for temperatures of 240 °C and above. Hence, provided the conditions for a thermally triggered OSWD prevail, the adsorbed QAC molecules migrate over the substrate surface in a direction away from the depositing γQAC crystal plane, with the concentration gradient and diffusion processes as the driving forces. As a result, further molecules can be deposited from the γQAC source, leading to an expansion of the QAC array.

As the formed adsorbate layers show a high degree of order, an additional thermal annealing effect is presumed. In this respect, it is referred to experiments conducted by Wagner et al., analysing the thermal annealing of a two-dimensional surface covering formed by QAC arrays exhibiting different orientations, however using Ag(111) as the substrate material [46]. Their results revealed that for a temperature range between 550 and 570 K (i.e. 277–297 °C), the structural properties of the QAC covering change towards the formation of extended and well-ordered monolayers. Hence, in analogy with the above, it can be said that for our study the thermal annealing presumably plays a part, by triggering the rearrangement of QAC molecules and thus leading to the formation of extended and highly ordered monolayers. In addition, worth mentioning are the series of continuative experiments performed to test the stability of these thermally generated QAC adsorbate structures [20]. Our results yielded no signs of structural decomposition after the samples have been stored for 36 days under ambient conditions and furthermore, the QAC adsorbates were observed to be resistant towards humidity and direct water contact.

Discussing the effect of sintering processes on the above, it can be said that first of all, the working temperatures (240 °C and 270 °C respectively) are way low than the melting temperature of γQAC (390 °C) [52]. Although early reports on lower temperature sintering observed with nanoscale particles conjectured a melting temperature reduction, this idea however has been dispelled by careful analysis, revealing further no new mechanism to be active in sintering nanoscale particles beyond known processes [55]. In this respect, as per the well-known viscous flow sintering model, the concept of sintering is analogous with the growth of sinter necks between contacting objects (i.e. grains in this context), connecting the contacting grains and forming a polycrystalline solid [55]. Hence, it can be said that a potential sintering would both interlink contacting semiconductor particles to strongly bonded crystalline structures and connect these structures to the substrate surface at the contact points. Further, in contrast to the OSWD process, the resulting sinter neck formation would be isotropic in nature, resulting in numerous contacting points, thereby establishing a permanent connection (besides, the type of chemical bonding between the substrate and the semiconductor is supposed to be π–π stacking). Thus, small-scale nanocrystals fixed to the substrate could be detected directly via STM, whereas the presence of large, permanently fixed nanocrystals would be noticed since they would considerably disturb the STM measurements, thereby making STM imaging hardly possible. However, STM measurements revealed no detection of sintered γQAC crystals of any kind, thereby highly limiting the influence of sintering processes on the above thermally triggered sample treatment approach.

2.3. *Replacing QAC by DMQAC*

Successfully applied to a HOPG substrate, the newly developed, thermally triggered sample preparation method generated a surface covering that synced with the requirements of a Raman spectroscopic analysis. Testing the applicability of OSWD for single graphene layer on a copper foil as the substrate material (refer Fig. 1) revealed similar supramolecular structures as detected on a HOPG substrate [20]. Hence, the single QAC molecules arranged themselves in one-dimensional chain-like structures, leading to the coverage of the substrate surface by multiple parallel and side-by-side appearing chain-like formations. Further, the lattice parameters ‘a’ and ‘b’ of the supramolecular monolayer (compare Fig. 1) were observed to correspond to one of the array configurations as observed on the HOPG substrates, such an HOPG array configuration being termed as the ‘relaxed QAC chain configuration’ in this case [20].

Next, the initial Raman measurements of samples fabricated via thermally triggered OSWD, applied to graphene as the substrate material, revealed that due to the sole presence of sp^2-bonded carbon atoms in both the γQAC and the graphene substrates, the location, the shape, and the intensity of the corresponding G peaks (described in the next sub-sections) was found to be quite similar for both the materials. Consequently, the spectra of both the samples could not be distinguished accurately, making hence the further, exact analysis quite a challenging task. Thus, to resolve the above, it was decided to replace γQAC by the quinacridone derivate dimethylquinacridone (DMQAC). In this regard, the linear DMQAC molecules (refer Fig. 4) generate three-dimensional crystal structures, iso-structural to the α^{I} polymorph formed by the QAC molecules [47–49].

In this respect, to begin with, different samples were analyzed via STM measurements, to explore the processability of DMQAC via the OSWD technique. Results revealed, analogous to QAC, the DMQAC molecules arranging themselves in one-dimensional supramolecular chains, forming in turn two-dimensional arrays. Further, within the limits of accuracy, the lattice parameters of these supramolecular structures were found to be identical for both the substrates HOPG and single layer graphene (refer Fig. 5). Besides, the latter substrate depict the distinct honeycomb structure of single layer graphene [26] (refer Fig. 5 (b)). However, further analysis revealed that in contrast to the QAC adsorbate structures (refer Fig. 3) [20], the DMQAC chains arrange themselves solely in a close-packing chain configuration (on both the HOPG and the single layer graphene), leading to DMQAC arrays with high packing density (refer Figs. 5 and 6).

In addition, regarding the adsorbate layer thickness, most of the observed DMQAC arrays were clearly determined to be two-dimensional monolayers (refer Figs. 5 and 9 (b)). However, previous studies using DMQAC revealed that, although rarely observed, bilayer and even trilayer structures could as well be detected, with their structure being similar to the ones seen when analysing QAC adsorbates [20]. Further, these structures were found to range in the size of single DMQAC chains up to arrays of a few dozen nanometres in diameter. Hence, for clarity purposes, the term ‘DMQAC adsorbate layer’ will be used hereinafter. Nevertheless, it should be noted that since the Raman spectroscopy is an averaging technique, the related analysis of potential doping effects is not disturbed by sporadically occurring small-sized bilayer or trilayer adsorbates. Furthermore, as extended multilayer adsorbates would generate fluorescence effects within the Raman signal, their occurrence could be detected, however, Raman analysis revealed no detection of multilayer DMQAC adsorbates (refer to the Raman discussion below).

Results revealed that the thermally triggered sample preparation method yielded an overall surface coverage of 92 ± 8% atop a HOPG substrate, with the DMQAC adsorbate layer found to be sufficiently homogeneous in nature (refer Fig. 6). However, worth noting here is that the structure of the copper foil leads to a rather uneven surface, making hence large-scale STM scans of the covered graphene samples impossible. Thus, we have not been able to determine the surface coverage of the graphene samples accurately, though, the promising results of the HOPG samples and the explored similar adsorbate structure properties on both the substrates indicated similar coverage rates. In addition, the STM analysis of graphene samples over a period of four weeks detected negligible decomposition of the DMQAC adsorbate structures, thus indicating the temporal stability and the resistance against humidity of the latter adsorbate layers being similar to that of QAC adsorbates [20].

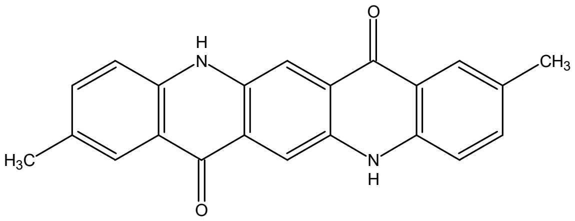

Fig. 4. Chemical structure of the DMQAC molecule.

2.4. Raman spectroscopy measurements

Generally speaking, the Raman spectrum of carbon-based substrates can be mainly characterised by three characteristic peaks [6,34–39], i.e. the D peak, the G peak, and the 2D peak. The D peak is typically observed at a Raman frequency of approx. 1350 cm^{-1} indicating a structural defect, owing to its activation due to A_{1g} mode breathing vibrations of six-membered sp^2 carbon rings, which are absent in defect-free graphene [34,35]. Hence, the D peak intensity increases with the amount of disorder present in the material [36]. The G peak, on the other hand, appears at approx. 1580 cm^{-1}, being associated with the doubly degenerate E_{2g} phonon at the Brillouin-zone centre [34,35]. Finally, the 2D peak is the second order of the D peak, found usually at about 2680 cm^{-1}. Further, since the 2D peak originates from a process where momentum conservation is satisfied by two phonons with opposite wave vectors, it is always present for graphene, with its activation requiring no structural defects [34–36].

Moreover, variations of the above characteristic Raman peaks can be generated by the introduction of either mechanical strain or by chemical doping. However, both these sources cause specific changes in the Raman spectrum, making hence the respective variations distinguishable from each other [35,36]. Mechanical strain, for example caused by an adsorbate layer or by a previous thermal treatment of the sample, modifies the crystal phonons due to changes in the lattice constants and the resulting structural disorder activates the D peak [36]. It was further found that the compressive strain leads to an upshift of the G and the 2D peak, the tensile stress whereas, leading to the downshift of both these peaks. However, in either case, the 2D peak shift is several times greater, with the intensity ratio of the 2D to G peak (I_{2D}/I_G) remaining unaltered [35,36]. Nevertheless, in contrast to the above, the intensity ratio I_{2D}/I_G has been observed to be sensitive to chemical doping. Appropriate doping effects cause the above ratio to decrease monotonically with an increase in both the electron and the hole concentration [6,36–38]. Also, as per empirical findings, doping with electron-donating aromatic molecules (i.e. electron- or n-type doping) downshifts the G peak frequency, whereas the presence of electron-withdrawing molecules (i.e. hole- or p-type doping) leads to a G peak upshift. Nonetheless, the 2D frequency is reported to be upshifted, irrespective of the type of doping [37,38].

The results of the Raman test series are as presented in Fig. 7. To begin with, the depicted Raman spectra were determined by averaging nine measurements, both for the pure graphene and the ‘DMQAC powder on a graphene substrate’ samples, and by averaging 16 measurements for the ‘graphene covered with a DMQAC adsorbate layer’ sample. Results revealed detection of no graphene-specific peaks at the appropriate peak locations (Fig. 7 (a)) within the spectrum of the DMQAC powder on a graphene substrate (treated with the identical, thermally triggered sample preparation method). However, a few DMQAC-specific peaks could be observed which could be determined precisely in the spectra of both the DMQAC samples (DMQAC powder and DMQAC adsorbate layer on graphene), their locations being determined as 1204 ± 2 cm^{-1}, 1233 ± 2 cm^{-1}, 1312 ± 1 cm^{-1}, and 1567 ± 2 cm^{-1}, respectively. Also, further analysis in this regard revealed no shift of the DMQAC-specific peaks in the spectra of both the DMQAC samples. Furthermore, worth noting here is that the spectrum of the sample ‘graphene covered with a DMQAC adsorbate layer’ exhibited additional peaks, which are as well related to DMQAC [56], their

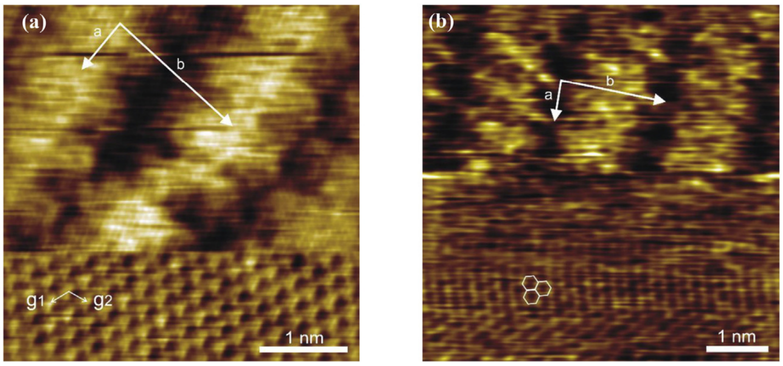

Fig. 5. STM images of supramolecular DMQAC structures (upper sections) and the subjacent substrates (l ower section). The STM pictures have been equalized using the substrates unit cell parameters for calibration. (a) The substrate in use is HOPG and the lattice parameters of the adsorbate structures were found to be as: a = 0.68 ± 0.02 nm, b = 1.72 ± 0.02 nm, and an intermediate angle of 87 ± 2°. The HOPG unit cell is depicted via the parameters g1 and g2, having lengths as: g1 = g2 = 0.246 nm. (b) Using single layer graphene on a copper foil as the substrate, the lattice parameters of the adsorbates were determined to be as: a = 0.67 ± 0.02 nm, b = 1.72 ± 0.02 nm, and an intermediate angle of 88 ± 2°. Further, the marked hexagon in the image represents one carbon ring of the graphene structure; the atom to atom distance in this regard being 0.142 nm.

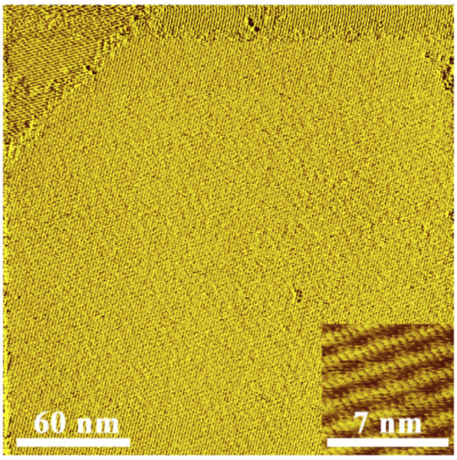

Fig. 6. Example STM picture of a two-dimensional supramolecular adsorbate layer atop a HOPG substrate generated by DMQAC molecules, yielding an overall average coverage rate of 92 ± 8%. Besides, the close-up inset in the bottom right corner highlights, how the DMQAC molecules arrange themselves within the adsorbate layer.

determined locations being as 1408 ± 1 cm^{-1}, 1509 ± 1 cm^{-1}, and 1648 ± 2 cm^{-1}, respectively. Nevertheless, the precise location of these peaks could not be determined in the spectrum of the sample 'graphene covered with DMQAC powder', due to the occurrence of fluorescence (Fig. 7 (b)) [57,58]. In this regard, the revealed finding that fluorescence effects are quenched by the properties and conditions of the sample 'graphene covered with a DMQAC adsorbate layer', indicate though a structural transition of the three-dimensional DMQAC particles into a thin adsorbate layer (being triggered by the OSWD process), thereby acting no longer as a bulk solid [59,60]. This deduction affirms the findings of the previously presented STM measurements.

Further investigation revealed that the spectra of the pure graphene substrate and that of the graphene sample covered with a two-dimensional DMQAC adsorbate layer comprises the graphene-specific peaks, i.e. the D, the G, and the 2D peaks (Fig. 7 (a)). The location of the D peak was found to be similar for both the samples (Fig. 7 (b)), however, owing to its significantly lower intensity in contrast to the other peaks, it being determined only at around 1348 ± 5 cm^{-1} (including twice the standard deviation). In addition, the D peak intensity was as well found to be similar for both the samples, thereby indicating the exclusion of thermally induced structural defects. Furthermore, for the pure graphene substrate, the G peak was found at 1592 ± 1 cm^{-1} and the 2D peak at 2691 ± 1 cm^{-1}, respectively, whereas for the 'graphene plus DMQAC adsorbate layer' sample, their locations being 1595 ± 2 cm^{-1} and 2701 ± 3 cm^{-1}, respectively (Fig. 7 (c) and (d)). Thus, the Raman spectrum of the DMQAC adsorbate layer sample revealed an upshift of both the G peak frequency (3 ± 2 cm^{-1}) and the 2D peak frequency (10 ± 3 cm^{-1}), indicating thereby chemical doping with electron-withdrawing aromatic molecules (i.e. p-type doping). The latter is further supported by literature findings, showing that DMQAC thin films act only as p-type materials [30,33]. Comparison of the Raman intensity ratio I_{2D}/I_G of the pure graphene substrate (I_{2D}/I_G = 1.15 ± 0.06) and the graphene substrate covered with a DMQAC adsorbate layer ($I_{2D}/I_G = 0.53 \pm 0.06$) further revealed a significant decrease, indicating hence the chemical doping of graphene as well. In addition, mechanical strain was excluded as the probable source of the Raman peak shifts, since no increase of the D peak intensity was found after the thermally triggered sample preparation and due to the decrease in the Raman intensity ratio I_{2D}/I_G.

2.5. Scanning Tunneling Spectroscopy (STS) analysis of DMQAC on graphene

In order to further verify the results of Raman spectroscopy by an independent experimental technique, an STS test series was conducted in addition. STS, determining the current-bias spectra I(V) at a fixed tip position, is known as a sensitive technique to probe the local electronic properties of a surface [26–32]. At low tip–sample voltages, the tunneling differential conductance is proportional to the local density of states of conducting and semiconducting samples [26–29]. However, due to the dependence of sample-tip separation on the tunneling probability, the STS acquisition relies on the initial set point tunneling conditions [28]. Thus, the tunneling distance for the below discussed STS spectra was adjusted with identical tunneling parameters, whenever possible: bias = 50.1 mV, and tunnel current = 1 nA for the analysis of graphene, and bias = 1.5 V, and tunnel current = 501 pA for the analysis of both DMQAC arrays and the test series regarding

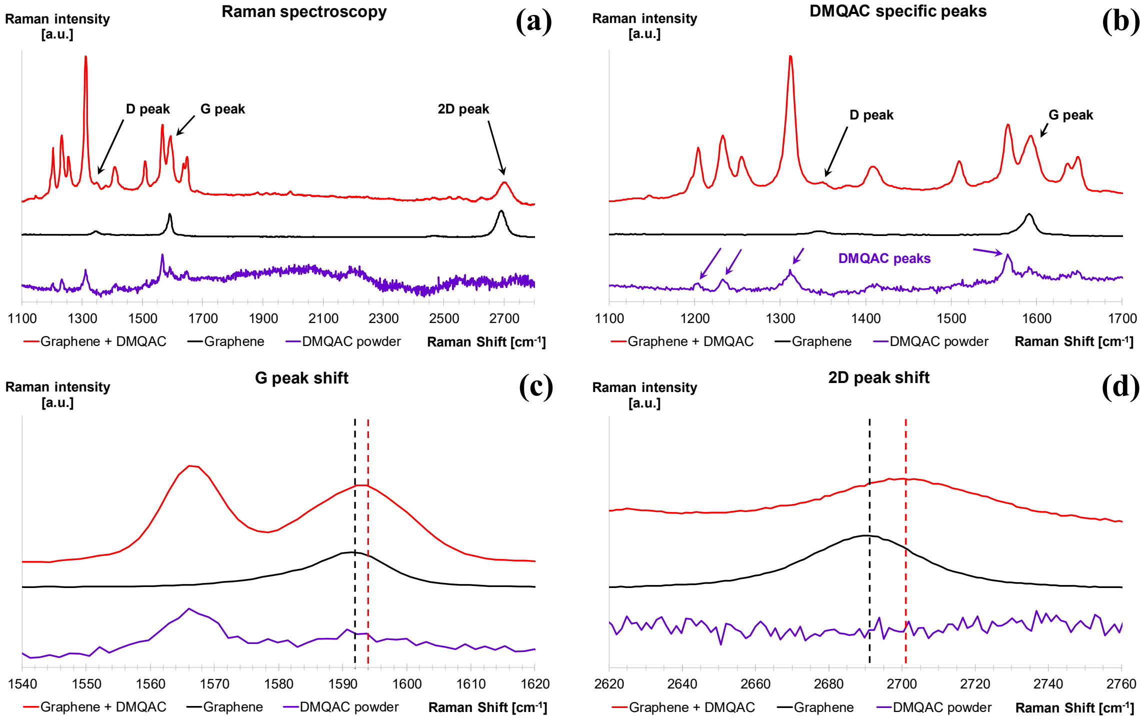

Fig. 7. Data representing the averaged results of the performed Raman measurements. (a) Overview of the Raman spectra in the relevant frequency range between 1100 and 2800 cm^{-1}. (b) Zoomed-in view of the frequency range between 1100 and 1700 cm^{-1}. The Raman spectra of both the DMQAC powder and the two-dimensional DMQAC adsorbate layer atop a graphene substrate depict additional peaks. Further, a close-up view of the frequency range revealing: (c) the G peak and (d) the 2D peak, respectively.

potential chemical doping. Further, each spectrum was acquired within 100 m s.

Appropriate samples were investigated via STS measurements, in order to explore the surface electronic structure of graphene substrates with DMQAC adsorbates atop. To begin with, STS spectra taken of pure graphene are as shown in Fig. 8 (a). As can be seen, the curve progressions are in agreement with the reported metallic behaviour of the zero-gap semiconductor graphene [27]. Further, the spectra taken of DMQAC arrays feature a sample bias range with approximately zero current (refer Fig. 8 (b)), as expected of a semiconducting material [27]. However, the curves are subject to strong fluctuations that are related to the ambient measurement conditions, causing thermal fluctuations that affect the STS measurement accuracy [27]. Thereby, owing to the above, the direct determination of the tunneling differential conductance was hardly possible. Instead, a trend line of the type $f(x) = a\,(x + b)^3$ (with 'a' and 'b' as constants) was fitted to the obtained spectra and differentiation yielded suitable parabolic shaped dI/dV curves (refer Figs. 8 (b) and Fig. 9 (a)). Assuming a differential conductance below 0.7 nA to be zero, the bandgap of DMQAC was estimated to be

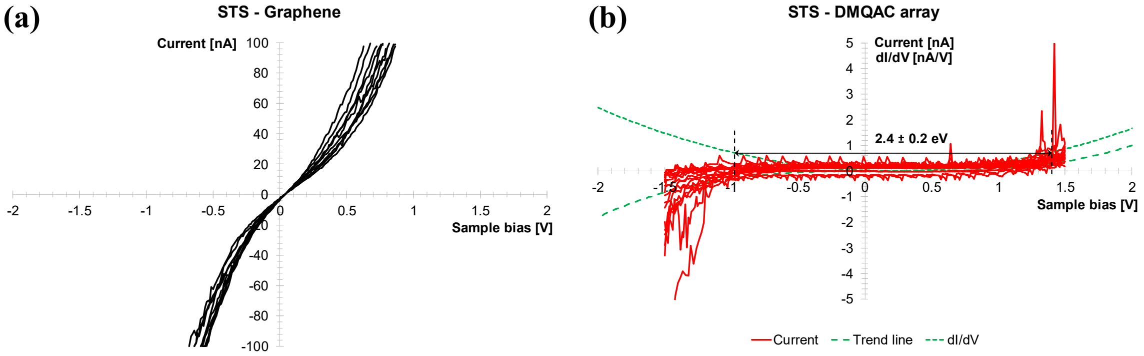

Fig. 8. STS measurements at different locations of three different (but equally prepared) samples. (a) 10 STS measurements of pure graphene. (b) 18 STS measurements of supramolecular DMQAC adsorbates. Further, the indicated trend line and the dedicated dI/dV curve exemplary reveal the determination of a bandgap (for further details, refer to the explanations in the text); the corresponding bandgap of a DMQAC monolayer being found as 2.4 ± 0.2 eV (including twice the standard deviation).

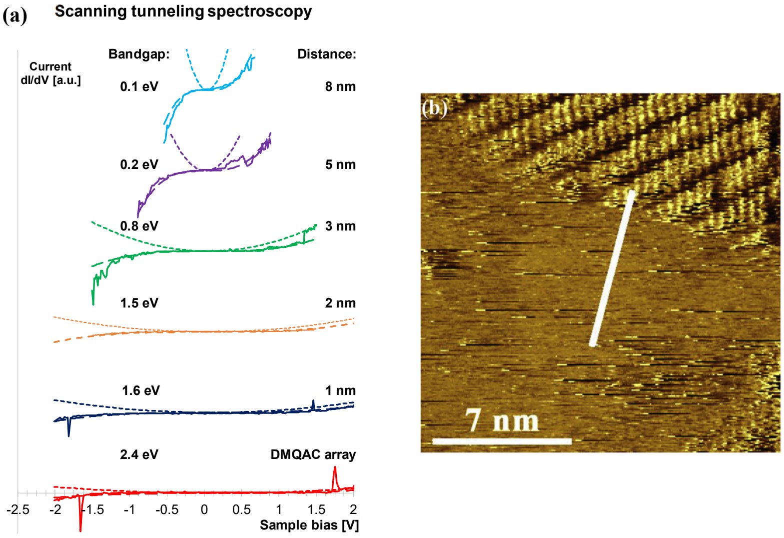

Fig. 9. (a) Example STS measurements, taken at different distances from a DMQAC array (including the calculated trend lines and the dI/dV curves). With the determined bandgaps indicated above the related spectrum, twice the standard deviation was deduced to be ±0.2 eV. (b) STM image of the region, at which the STS measurements were taken. The upper section depicts a DMQAC monolayer and the lower section shows the bare graphene substrate. The measurement points were located on the highlighted white line.

2.4 ± 0.2 eV (including twice the standard deviation), the result hence being in good accordance with the reported HOMO − LUMO gap of DMQAC of 2.3 eV [30].

Regarding the analysis of a potential chemical doping, it was reported that a suitable semiconducting surface adsorbate modifies the electronic properties of the substrate beyond the physical borders of the adsorbate. Hence, it was found that the STS measurements yield a decreasing bandgap in the direction away from the chemical dopant [31,32]. The results of the related test series are shown in Fig. 9. As can be seen, the determined band gap decreases almost linearly in the direction away from the DMQAC array, reaching the detection limit of 0.1 ± 0.2 eV at a distance of 8 nm. The latter result thus signalizes the chemical doping of graphene via supramolecular DMQAC adsorbates, generated via the OSWD.

3. Conclusions

Our approach to thermally trigger the solid-solid wetting of crystalline carbon surfaces by organic semiconductor particles enables an easily applicable technique to achieve monolayers with high surface coverage rates and uniform adsorbate structures. Moreover, graphene samples generated in this way allows for the analysis of possible doping effects via techniques as Raman spectroscopy. Additionally, by using the commercially available pigment DMQAC for the new OSWD approach, clear spectral evidence of chemical doping effects of graphene could be obtained. This finding is further supported by STS analysis, showing evidence of chemical doping by DMQA adsorbate structures. The results hence bring forward new and straightforward to perform approaches for the fabrication and bandgap engineering of low-cost, but large-scale products based on pigment-functionalized graphene, like the printed and potentially flexible carbon based electronics [9].

Acknowledgements

The authors would like to thank Michael Blum for his kind support with the STM measurements using graphene as the substrate material. Heartfelt acknowledgment as well to Michaela Wenner for her assistance in exploring the potentials of sample reworking. We also would like to extend our gratitude to Arthur Wesemann for his contribution with experiments and valuable experiences, in regard to the imaging of organic semiconductor adsorbates via the NaioSTM setup (as a precondition for our STS studies). Also, we would like to thank Neeti Phatak for her support with the proofreading and editing of this publication. The Bayerisches Staatsministerium für Umwelt und Verbraucherschutz is gratefully acknowledged for their funding.

Appendix A. Supplementary data

Supplementary data related to this article can be found at http://dx.doi.org/10.1016/j.carbon.2017.09.043.

References

[1] S. Thompson, S. Parthasarathy, Moore's law: the future of Si microelectronics, Mater. Today 9 (2006) 20–25, http://dx.doi.org/10.1016/S1369-7021(06)71539-5.
[2] P. Avouris, Z. Chen, V. Perebeinos, Carbon-based electronics, Nat. Nanotechnol. 2 (2007) 605–615, http://dx.doi.org/10.1038/nnano.2007.300.
[3] W. Lu, C.M. Lieber, Nanoelectronics from the bottom up, Nat. Mater. 6 (2007) 841–850, http://dx.doi.org/10.1038/nmat2028.
[4] H.-H. Chen, S.H. Su, S.-L. Chang, B.-Y. Cheng, S.W. Chen, H.-Y. Chen, et al., Tailoring low-dimensional structures of bismuth on monolayer epitaxial graphene, Sci. Rep. 5 (2015) 11623, http://dx.doi.org/10.1038/srep11623.
[5] S. Tans, A. Verschueren, C. Dekker, Room-temperature transistor based on a single carbon nanotube, Nature 672 (1998) 669–672, http://dx.doi.org/10.1038/29954.
[6] H. Medina, Y.C. Lin, D. Obergfell, P.W. Chiu, Tuning of charge densities in graphene by molecule doping, Adv. Funct. Mater. 21 (2011) 2687–2692, http://dx.doi.org/10.1002/adfm.201100401.
[7] A.K. Manna, S.K. Pati, Tuning the electronic structure of graphene by molecular charge transfer: a computational study, Chem. An Asian J 4 (2009) 855–860, http://dx.doi.org/10.1002/asia.200800486.
[8] B. Long, M. Manning, M. Burke, B.N. Szafranek, G. Visimberga, D. Thompson, et al., Non-covalent functionalization of graphene using self-assembly of alkane-amines, Adv. Funct. Mater. 22 (2012) 717–725, http://dx.doi.org/10.1002/adfm.201101956.
[9] S. Park, M. Vosguerichian, Z. Bao, A review of fabrication and applications of

carbon nanotube film-based flexible electronics, Nanoscale 5 (2013) 1727–1752, http://dx.doi.org/10.1039/c3nr33560g.

[10] N. Liu, Y. Zhou, N. Ai, C. Luo, J. Peng, J. Wang, et al., High-performance, all-solution-processed organic nanowire transistor arrays with inkjet-printing patterned electrodes, Langmuir 27 (2011) 14710–14715, http://dx.doi.org/10.1021/la2033324.

[11] N. Liu, Y. Zhou, L. Wang, J. Peng, J. Wang, J. Pei, et al., In situ Growing and patterning of aligned organic nanowire arrays via dip coating, Langmuir 25 (2009) 665–671, http://dx.doi.org/10.1021/la8036633.

[12] J.Y. Zheng, Y. Yan, X. Wang, Y.S. Zhao, J. Huang, J. Yao, Wire-on-wire growth of fluorescent organic heterojunctions, J. Am. Chem. Soc. 134 (2012) 2880–2883, http://dx.doi.org/10.1021/ja209815f.

[13] G. Yu, C.M. Lieber, Assembly and integration of semiconductor nanowires for functional nanosystems, Pure Appl. Chem. 82 (2010) 2295–2314, http://dx.doi.org/10.1351/PAC-CON-10-07-06.

[14] B.J. Jordan, Y. Ofir, D. Patra, S.T. Caldwell, A. Kennedy, S. Joubanian, et al., Controlled self-assembly of organic nanowires and platelets using dipolar and hydrogen-bonding interactions, Small 4 (2008) 2074–2078, http://dx.doi.org/10.1002/smll.200800811.

[15] M. Liu, Z. Ji, L. Shang, Top-down fabrication of nanostructures, in: L. Chi (Ed.), Nanotechnology, Vol. 8: Nanostructured SurfacesWILEY-VCH, Weinheim, 2010, pp. 17–35.

[16] D. Zhong, H. Zhang, L. Chi, Surface-supported nanostructures directed by atomic- and molecular-level templates, in: L. Chi (Ed.), Nanotechnology, Vol. 8: Nanostructured SurfacesWILEY-VCH, Weinheim, 2010, pp. 357–369.

[17] S. Kowarik, A. Gerlach, F. Schreiber, Organic molecular beam deposition: fundamentals, growth dynamics, and in situ studies, J. Phys. Condens. Matter 20 (2008), 184005, http://dx.doi.org/10.1088/0953-8984/20/18/184005.

[18] M. Treier, E. Orgiu, L. Zalewski, D. Cho, R. Rieger, K. Müllen, et al., Solid−solid transfer of organic semiconductors for field-effect transistor fabrication, J. Mater. Chem. 20 (2010) 9018, http://dx.doi.org/10.1039/c0jm02173c.

[19] F. Trixler, T. Markert, M. Lackinger, F. Jamitzky, W.M. Heckl, Supramolecular self-assembly initiated by solid−solid wetting, Chem. A Eur. J. 13 (2007) 7785–7790, http://dx.doi.org/10.1002/chem.200700529.

[20] A. Eberle, A. Nosek, J. Büttner, T. Markert, F. Trixler, Growing low-dimensional supramolecular crystals directly from 3D particles, CrystEngComm 19 (2017) 1417–1426, http://dx.doi.org/10.1039/C6CE02348G.

[21] F. Trixler, W.M. Heckl, Various approaches to control solid/solid wetting self-assembly of organic semiconductors with STM, in: A. Méndez-Vilas, J. Diaz (Eds.), Modern Research and Educational Topics in Microscopy, Vol. 2, Formatex, Badajoz, 2007, pp. 534–541.

[22] J.A.A.W. Elemans, S. Lei, S. De Feyter, Molecular and supramolecular networks on surfaces: from two-dimensional crystal engineering to reactivity, Angew. Chem. Int. Ed. 48 (2009) 7298–7332, http://dx.doi.org/10.1002/anie.200806339.

[23] J. Haber, T. Machej, T. Czeppe, The phenomenon of wetting at solid/solid interface, Surf. Sci. 151 (1985) 301–310, http://dx.doi.org/10.1016/0039-6028(85)90468-6.

[24] J. Leyrer, R. Margraf, E. Taglauer, H. Knözinger, Solid-solid wetting and formation of monolayers in supported oxide systems, Surf. Sci. 201 (1988) 603–623, http://dx.doi.org/10.1016/0039-6028(88)90505-5.

[25] F. Bertinchamps, C. Grégoire, E.M. Gaigneaux, Systematic investigation of supported transition metal oxide based formulations for the catalytic oxidative elimination of (chloro)-aromatics, Appl. Catal. B Environ. 66 (2006) 1–9, http://dx.doi.org/10.1016/j.apcatb.2006.02.011.

[26] G. Li, A. Luican, E.Y. Andrei, Scanning tunneling spectroscopy of graphene on graphite, Phys. Rev. Lett. 102 (2009) 1–4, http://dx.doi.org/10.1103/PhysRevLett.102.176804.

[27] A. Castellanos-Gomez, M. Wojtaszek, Arramel, N. Tombros, B.J. Van Wees, Reversible hydrogenation and bandgap opening of graphene and graphite surfaces probed by scanning tunneling spectroscopy, Small 8 (2012) 1607–1613, http://dx.doi.org/10.1002/smll.201101908.

[28] R.J. Hamers, Atomic-resolution surface spectroscopy with the scanning tunneling microscope, Annu. Rev. Phys. Chem. 40 (1989) 531–559, http://dx.doi.org/10.1146/annurev.pc.40.100189.002531.

[29] F.W. Herbert, A. Krishnamoorthy, K.J. Van Vliet, B. Yildiz, Quantification of electronic band gap and surface states on FeS2(100), Surf. Sci. 618 (2013) 53–61, http://dx.doi.org/10.1016/j.susc.2013.08.014.

[30] S.-J. Lim, D.-S. Leem, K.-B. Park, K.-S. Kim, S. Sul, K. Na, et al., Organic-on-silicon complementary metal-oxide-semiconductor colour image sensors, Sci. Rep. 5 (2015) 7708, http://dx.doi.org/10.1038/srep07708.

[31] P. Lauffer, K.V. Emtsev, R. Graupner, T. Seyller, L. Ley, Molecular and electronic structure of PTCDA on bilayer graphene on SiC(0001) studied with scanning tunneling microscopy, Phys. Status Solidi. 245 (2008) 2064–2067, http://dx.doi.org/10.1002/pssb.200879615.

[32] L. Zhao, R. He, K.T. Rim, T. Schiros, K.S. Kim, H. Zhou, et al., Visualizing individual nitrogen dopants in monolayer graphene, Sci. (80-.) 333 (2011) 999–1003, http://dx.doi.org/10.1126/science.1208759.

[33] M. Hiramoto, S. Kawase, M. Yokoyama, Photoinduced hole injection multiplication in p-type quinacridone pigment films, Jpn. J. Appl. Phys. 35 (1996), http://dx.doi.org/10.1143/JJAP.35.L349. Part 2 Lett.

[34] M.W. Iqbal, A.K. Singh, M.Z. Iqbal, J. Eom, Raman fingerprint of doping due to metal adsorbates on graphene, J. Phys. Condens. Matter 24 (2012), 335301, http://dx.doi.org/10.1088/0953-8984/24/33/335301.

[35] W.X. Wang, S.H. Liang, T. Yu, D.H. Li, Y.B. Li, X.F. Han, The study of interaction between graphene and metals by Raman spectroscopy, J. Appl. Phys. 109 (2011) 15–18, http://dx.doi.org/10.1063/1.3536670.

[36] C. Casiraghi, Probing disorder and charged impurities in graphene by Raman spectroscopy, Phys. Status Solidi Rapid Res. Lett. 3 (2009) 175–177, http://dx.doi.org/10.1002/pssr.200903135.

[37] X. Dong, D. Fu, W. Fang, Y. Shi, P. Chen, L.J. Li, Doping single-layer graphene with aromatic molecules, Small 5 (2009) 1422–1426, http://dx.doi.org/10.1002/smll.200801711.

[38] H. Liu, Y. Liu, D. Zhu, Chemical doping of graphene, J. Mater. Chem. 21 (2011) 3335, http://dx.doi.org/10.1039/c0jm02922j.

[39] Z. Ni, Y. Wang, T. Yu, Z. Shen, Raman spectroscopy and imaging of graphene, Nano Res. 1 (2008) 273–291, http://dx.doi.org/10.1007/s12274-008-8036-1.

[40] E.D. Głowacki, R.R. Tangorra, H. Coskun, D. Farka, A. Operamolla, Y. Kanbur, et al., Bioconjugation of hydrogen-bonded organic semiconductors with functional proteins, J. Mater. Chem. C (2015) 6554–6564, http://dx.doi.org/10.1039/C5TC00556F.

[41] E.D. Głowacki, G. Romanazzi, C. Yumusak, H. Coskun, U. Monkowius, G. Voss, et al., Epindolidiones-versatile and stable hydrogen-bonded pigments for organic field-effect transistors and light-emitting diodes, Adv. Funct. Mater. (2014) 1–12, http://dx.doi.org/10.1002/adfm.201402539.

[42] M. Sytnyk, E.D. Głowacki, S. Yakunin, G. Voss, W. Schöfberger, D. Kriegner, et al., Hydrogen-bonded organic semiconductor micro- and nanocrystals: from colloidal syntheses to (Opto-)Electronic devices, J. Am. Chem. Soc. 136 (2014) 16522–16532.

[43] E.D. Głowacki, M. Irimia-Vladu, M. Kaltenbrunner, J. Gsiorowski, M.S. White, U. Monkowius, et al., Hydrogen-bonded semiconducting pigments for air-stable field-effect transistors, Adv. Mater. 25 (2013) 1563–1569, http://dx.doi.org/10.1002/adma.201204039.

[44] E.D. Glowacki, L. Leonat, G. Voss, M. Bodea, Z. Bozkurt, M. Irimia-Vladu, et al., Natural and nature-inspired semiconductors for organic electronics, Org. Semicond. Sensors Bioelectron IV (2011) 8118, http://dx.doi.org/10.1117/12.892467, 81180M–81180M–10.

[45] E.D. Głowacki, M. Irimia-Vladu, S. Bauer, N.S. Sariciftci, Hydrogen-bonds in molecular solids – from biological systems to organic electronics, J. Mater. Chem. B 1 (2013) 3742, http://dx.doi.org/10.1039/c3tb20193g.

[46] T. Wagner, M. Györök, D. Huber, P. Zeppenfeld, E.D. Głowacki, Quinacridone on Ag(111): hydrogen bonding versus chirality, J. Phys. Chem. C 118 (2014) 10911–10920, http://dx.doi.org/10.1021/jp502148x.

[47] E.F. Paulus, F.J.J. Leusen, M.U. Schmidt, Crystal structures of quinacridones, CrystEngComm 9 (2007) 131–143, http://dx.doi.org/10.1039/b613059c.

[48] G. Lincke, On quinacridones and their supramolecular mesomerism within the crystal lattice, Dye. Pigment. 52 (2002) 169–181, http://dx.doi.org/10.1016/S0143-7208(01)00085-7.

[49] A.D. Squires, R.A. Lewis, A.J. Zaczek, T.M. Korter, Distinguishing quinacridone pigments via terahertz spectroscopy: absorption experiments and solid-state density functional theory simulations, J. Phys. Chem. A 121 (2017) 3423–3429, http://dx.doi.org/10.1021/acs.jpca.7b01582.

[50] Q. Zhao, Y. Liu, E.W. Abel, Effect of temperature on the surface free energy of amorphous carbon films, J. Colloid Interface Sci. 280 (2004) 174–183, http://dx.doi.org/10.1016/j.jcis.2004.07.004.

[51] S.K. Rhee, Critical surface energies of Al203 and graphite, J. Am. Ceram. Soc. 55 (1972) 300–303, http://dx.doi.org/10.1111/j.1151-2916.1972.tb11289.x.

[52] D.R. Lide, CRC Handbook of Chemistry and Physics, CRC Press, Boca Raton, 2005, p. 243. Internet Version.

[53] D. McDougall, H. Hattab, M.T. Hershberger, M. Hupalo, M. Horn von Hoegen, P.A. Thiel, et al., Dy uniform film morphologies on graphene studied with SPA-LEED and STM, Carbon 108 (2016) 283–290, http://dx.doi.org/10.1016/j.carbon.2016.06.083.

[54] D. Appy, H. Lei, C.-Z. Wang, M.C. Tringides, D.-J. Liu, J.W. Evans, et al., Transition metals on the (0001) surface of graphite: fundamental aspects of adsorption, diffusion, and morphology, Prog. Surf. Sci. 89 (2014) 219–238, http://dx.doi.org/10.1016/j.progsurf.2014.08.001.

[55] R.M. German, Sintering: From Empirical Observations to Scientific Principles, Butterworth-Heinemann, Oxford, 2014, pp. 71–82, 413-421.

[56] E. del Puerto, C. Domingo, J.V. Garcia Ramos, S. Sanchez-Cortes, Adsorption study and detection of the high performance organic pigments quinacridone and 2,9-dimethylquinacridone on Ag nanoparticles by surface-enhanced optical spectroscopy, Langmuir 30 (2014) 753–761, http://dx.doi.org/10.1021/la403625u.

[57] J.A. Smith, R.M. West, M. Allen, Acridones and quinacridones: novel fluorophores for fluorescence lifetime studies, J. Fluoresc. 14 (2004) 151–171, http://dx.doi.org/10.1023/B: JOFL.0000016287.56322.eb.

[58] P.L. Gentili, C. Clementi, A. Romani, Ultraviolet-visible absorption and luminescence properties of quinacridone-barium sulfate solid mixtures, Appl. Spectrosc. 64 (2010) 923–929, http://dx.doi.org/10.1366/000370210792080993.

[59] M.R. Kagan, R.L. McCreery, Reduction of fluorescence interference in raman-spectroscopy via analyte adsorption on graphitic carbon, Anal. Chem. 66 (1994) 4159–4165, http://dx.doi.org/10.1021/ac00095a008.

[60] L. Xie, X. Ling, Y. Fang, J. Zhang, Z. Liu, Graphene as a substrate to suppress fluorescence in resonance raman spectroscopy, J. Am. Chem. Soc. 131 (2009) 9890–9891, http://dx.doi.org/10.1021/ja9037593.

2.3. Doping Graphene via OSWD - Supporting Information

Supporting Information

Doping Graphene via Organic Solid-Solid Wetting Deposition

Alexander Eberle[a], *Andrea Greiner*[a], *Natalia P. Ivleva*[b], *Banupriya Arumugam*[c], *Reinhard Niessner*[b], *Frank Trixler*[a,d,*]

[a] Department für Geo- und Umweltwissenschaften and Center for NanoScience (CeNS), Ludwig-Maximilians-Universität München, Theresienstraße 41, 80333 München, Germany

[b] Institute of Hydrochemistry, Chair for Analytical Chemistry, Technische Universität München, Marchioninistr. 17, 81377, München, Germany

[c] Institute for Nanoelectronics, Technische Universität München, Theresienstrasse 90, 80333 München, Germany

[d] TUM School of Education, Technische Universität München and Deutsches Museum, Museumsinsel 1, 80538 München, Germany

---

* Corresponding author. Tel.: +49 89 2179 509; fax: +49 89 2179 239.
E-mail address: trixler@lrz.uni-muenchen.de (F. Trixler)

Reproduced by permission of Elsevier Ltd.
https://www.sciencedirect.com/science/article/pii/S0008622317309181

Materials and methods

Sample preparation

As a standard Organic Solid-Solid Wetting Deposition (OSWD) sample for scanning tunnelling microscope (STM) investigations, a dispersion with 2 wt% of the pigment γQAC (5,12-Dihydro-quino[2,3-b]acridine-7,14-dione, purchased as Hostaperm Red E5B02 from Clariant) dispersed in 4 ml of the dispersing agent 8CB (purchased as 4'-n-Octylbiphenyl-4-carbonitrile from Alfa Aesar, item no. 52709-84-9) was prepared. A few drops of this dispersion were then dispensed on a highly ordered pyrolytic graphite (HOPG, supplier NT-MDT, item no. GRBS/1.0), to trigger the OSWD at the interface between the dispersed pigment particles and the HOPG. Besides, single layer graphene on a copper foil (suppliers: Graphene Laboratories, item no. CVD-Cu-2X2, and Graphenea Inc.) was used as the substrate material for further tests. Also, as an alternative sample preparation method (to thermally trigger the OSWD), the HOPG substrate was fully covered with the powdered pigment, but without a catalysing dispersing agent. The covered substrate was then heated up to 240 °C and 270 °C, respectively, using a special hotplate, enabling an accurate temperature control and providing a smooth temperature increase (Stuart SD160, temperature accuracy ± 1.0 °C). In any case, the ready-made STM samples were investigated within days, and as per the previous tests, QAC arrays were observed unaltered in their structure for a minimum of four weeks, unless not influenced via any external forces [1].

Further, for the Raman experiments, single layer graphene on Si/SiO_2 (purchased from Graphene Laboratories, item no. 1ML-SIO2-5P) was used as the substrate material and DMQAC (2,9-Dimethyl-5,12-dihydro-quino[2,3-b]acridine-7,14-dione, purchased as Hostaperm Pink E from Clariant) as the organic semiconductor. In order to induce thermally triggered OSWD on the substrate graphene/Si/SiO_2, a small amount of powdered DMQAC, enough to cover the substrate surface, was added on top of the substrate. The substrate (along with the powdered organic semiconductor atop) was then placed on the previously mentioned hot plate, heating the sample up to approx. 270 °C. Once the sample was heated well for the given temperature, it was taken from the hot plate and the pigment powder was immediately removed from the substrate surface by mechanical shaking. Being still hot, the pigment powder does not adsorb humidity from the surrounding environment and thus does not stick to the substrate surface. Hence, the appropriately prepared Raman samples in the above manner enabled an accurate Raman spectroscopy analysis, being free of measurements artefacts related to traces of bulk pigment particles. Moreover, before performing any Raman measurements, the Raman sample was chilled to room temperature under ambient conditions.

STM and STS settings

Two types of STM systems operating under ambient conditions were used for this study. First was a home-built STM combined with a SPM 100 control system, supplied by RHK Technology Inc.; the scans settings being: bias = 1 V, tunnel current = 300 pA, and the line time = 50 ms. Secondly, a commercial STM, type NaioSTM, supplied by Nanosurf GmbH, was employed for the measurements, as depicted by fig. 5, 8 and 9 within the main article; the scans settings for imaging DMQAC being: bias = 1.5 V, current = 501 pA, and line time = 80 ms, and for imaging graphene being: bias = 50.1 mV, tunnel current = 1 nA, and line time = 60 ms. In addition, the voltage pulses used to improve the scan quality were set in the range between 4.3 and 10 V.

The STS measurements were performed using the NaioSTM. The tunneling distance was adjusted with tunneling parameters being similar to the ones as mentioned above. Each spectrum was acquired within 100 ms; both the STM and the STS measurements being performed under ambient conditions. All STS measurements were performed at randomly distributed positions and from 3 different (but equally prepared) samples, to exclude incidental findings. Further, the graphene samples used for the STS measurements were prepared via the standard OSWD sample preparation method, thereby using a dispersion of DMQAC and 8CB. This preparation method was preferred owing to two reasons: First, STM and STS measurements require a conductive sample, thus excluding graphene on SiO2/Si and making the use of single layer graphene on copper foil mandatory. However, according to the specifications of the manufacturer Graphenea Inc., single layer graphene on the copper foil is only thermally stable up to 60 °C. Tests further in this regard, applying the thermally triggered OSWD sample preparation method to single layer graphene on a copper foil, revealed significant damage of the substrate, thereby making accurate STM and STS measurements impossible for graphene/Cu samples prepared via thermally triggered OSWD. Secondly, OSWD induced by the dispersing agent 8CB enables to achieve STS under controlled ambient conditions without undefined contamination layers. STS experiments with pure

8CB on graphene/Cu yielded no evidence of chemical doping by 8CB adsorbate layers (refer example STS measurements in Fig. 1).

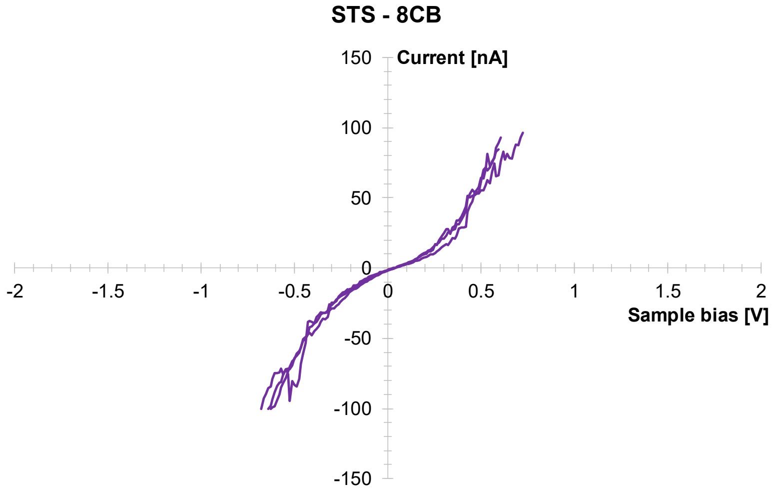

Fig. 1. Example STS measurements of 8CB adsorbate layers atop single layer graphene.

Image processing

For analysing the supramolecular adsorbate structures in the STM images, the software SPIP™ (Scanning Probe Image Processor, Version 2.3000; distributor: Image Metrology A/S) was used. Image distortions by the drift of a STM scan were analysed and corrected by applying two-dimensional Fast Fourier Transformation (FFT) to the images, done by using the known lattice parameters of the substrates as a reference. Autocorrelations of corrected images were employed for measuring the distances and angles in the substrates and the adsorbates. To minimize noise in the final STM images, a selective FFT filtering was applied with thresholding between 15-25 (min.) and 100 (max.).

Determining the surface coverage

To determine the coverage of the HOPG surface by the QAC arrays within a single STM picture, the software Gwyddion (64bit), version 2.42 was used. For this, initially, the QAC arrays via the tool “Mask Editor” were highlighted, followed by the export of single array dimensions by the “Grain distributions” tool, this finally being accompanied by the Microsoft Excel 2013 calculations to determine the coverage ratio. Further, to investigate the average coverage of a STM sample, per sample an area of about 0.7 µm² was analysed. This was done by using a number of STM pictures with high scan resolution and without measurement artefacts, the images were further randomly selected from at least five clearly separated positions on the covered substrate; the average coverage rates, including the double standard deviations, being specified in the current publication.

Raman Spectroscopy

The Raman experiments were performed using a LabRAM HR Evolution Raman System, provided by HORIBA Scientific and controlled via the software LabSpec 6. Further, the tests were performed using a frequency-doubled Nd:YAG laser, having a wave length of 532 nm and applying a laser power output of 0.84 mW on the sample. Besides, a diffraction grating with 600 lines per mm and a confocal pinhole with 100 mm diameter were employed. The wavelength calibration was realized by focusing the laser on a silicon wafer and analysing the first order phonon band of silicon at 520 cm^{-1}. Since the DMQAC powder sample shows no first order phonon band of silicon at 520 cm^{-1}, the wavelength calibration for this sample was done using the DMQAC peak at 1312 cm^{-1}. Furthermore, the intensity correction algorithm of the LabSpec 6 software was used to adjust the Raman intensity variations caused by the Raman measurement system. To compensate for the occurrence of a strong fluorescence effect while analysing the ‘graphene plus DMQAC powder’ samples, the measurements were adjusted via a baseline correction, by applying a polynomial of the sixth degree.

Additional information

8CB

With respect to the result presented in the present publication, it should be noted that 8CB is known to self-assemble stable and well-ordered arrays that can be detected via STM [2] (for the chemical structure of 8CB refer Fig. 3). Having used 8CB in numerous STM experiments, it was found that the 8CB arrays and arrays built by semiconductor molecules can sometimes be imaged at the same time using identical STM scan settings, and sometimes not. In this regard, we propose that the difficulties in imaging both the adsorbate structures simultaneously are related to the orientation of the liquid crystal 8CB with respect to the substrate surface. STM detectable 8CB adsorbate structures form only when the liquid crystal is oriented in such a way that the molecules are aligned parallel to the substrate. So, although no 8CB can be seen in the figures depicted in relation to the reworking experiments, 8CB arrays could however be found on the HOPG surface (refer Fig. 2). Further, we could never find bilayer or multiple layer structures built by alternating layers of QAC and 8CB arrays to date. Thus, it is assumed that the uncovered areas around QAC arrays most likely contain 8CB arrays, although they sometimes cannot be imaged via STM. In addition, results indicate that the QAC arrays exhibit a stronger affinity to the HOPG surface than the 8CB arrays. This is probably attributed to a strong π-π interaction between the fully condensed aromatic ring system of the QAC molecules and the graphene substrate, whereas the 8CB molecule providing just two phenyl groups enabling a π-π interaction and a weakly interacting alkyl chain (for the chemical structure of the 8CB molecule refer to the supporting information). Hence, it is assumed that the QAC molecules compete successfully for array formation, and furthermore that 8CB arrays are expelled by the expanding QAC arrays. The latter assumption is additionally supported by the finding that the reworked HOPG surface almost exclusively contains supramolecular QAC structures, whereas 8CB arrays being hardly found on such a sample.

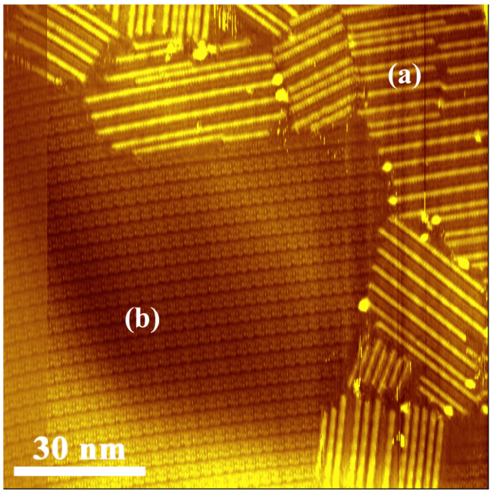

Fig. 2. STM image of a HOPG substrate treated with a dispersion of γQAC and 8CB. (a) Supramolecular QAC array. (b) Array formed by 8CB molecules.

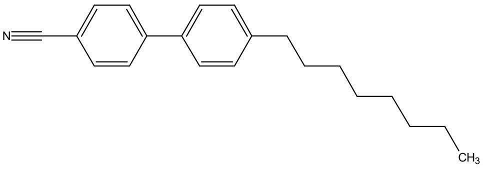

Fig. 3. Chemical structure of the 8CB molecule.

References

[1] A. Eberle, A. Nosek, J. Büttner, T. Markert, F. Trixler, Growing low-dimensional supramolecular crystals directly from 3D particles, CrystEngComm. (2017). doi:10.1039/C6CE02348G.

[2] T.J. McMaster, H. Carr, M.J. Miles, P. Cairns, V.J. Morris, Adsorption of liquid crystals imaged using scanning tunneling microscopy, J. Vac. Sci. Technol. A Vacuum, Surfaces, Film. 8 (1990) 672–674. doi:10.1116/1.576370.

2.4. Revealing the Physicochemical Basis of OSWD

JOURNAL OF THE AMERICAN CHEMICAL SOCIETY
Article
Cite This: J. Am. Chem. Soc. 2018, 140, 1327−1336
pubs.acs.org/JACS

Revealing the Physicochemical Basis of Organic Solid−Solid Wetting Deposition: Casimir-like Forces, Hydrophobic Collapse, and the Role of the Zeta Potential

Alexander Eberle,[†,‡] Thomas Markert,[§] and Frank Trixler*[,†,∥]

[†]Department of Earth and Environmental Sciences and Center for NanoScience (CeNS), Ludwig-Maximilians-Universität München, Theresienstraße 41, 80333 München, Germany
[‡]Helmholtz Institute Erlangen-Nürnberg for Renewable Energy, Egerlandstr. 3, 91058 Erlangen, Germany
[§]Institute of Theoretical Chemistry, Ulm University, Albert-Einstein-Allee 11, 89081 Ulm, Germany
[∥]TUM School of Education, Technical University of Munich and Deutsches Museum, Museumsinsel 1, 80538 München, Germany

Supporting Information

ABSTRACT: Supramolecular self-assembly at the solid−solid interface enables the deposition and monolayer formation of insoluble organic semiconductors under ambient conditions. The underlying process, termed as the organic solid−solid wetting deposition (OSWD), generates two-dimensional adsorbates directly from dispersed three-dimensional organic crystals. This straightforward process has important implications in various fields of research and technology, such as in the domains of low-dimensional crystal engineering, the chemical doping and band gap engineering of graphene, and in the area of field-effect transistor fabrication. However, to date, lack of an in-depth understanding of the physicochemical basis of the OSWD prevented the identification of important parameters, essential to achieve a better control of the growth of monolayers and supramolecular assemblies with defined structures, sizes, and coverage areas. Here we propose a detailed model for the OSWD, derived from experimental and theoretical results that have been acquired by using the organic semiconductor quinacridone as an example system. The model reveals the vital role of the ζ potential and includes Casimir-like fluctuation-induced forces and the effect of dewetting in hydrophobic nanoconfinements. Based on our results, the OSWD of insoluble organic molecules can hence be applied to environmental friendly and low-cost dispersing agents, such as water. In addition, the model substantially enhances the ability to control the OSWD in terms of adsorbate structure and substrate coverage.

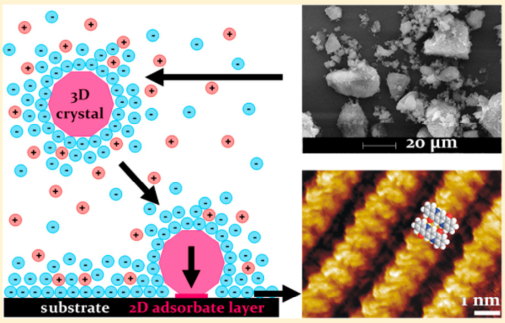

■ INTRODUCTION

Supramolecular self-assembly, utilizing programmable, noncovalent interactions, enables the bottom-up fabrication of low-dimensional nanostructures and adsorbates using organic semiconductor molecules for applications such as carbon-based nanoelectronics[1−7] and crystal engineering.[8−12] There are two common technologies to perform the corresponding bottom-up assembly: vapor deposition and liquid-phase deposition techniques.[13,14] However, both the approaches possess distinct limitations: the vapor deposition methods, like the organic molecular beam deposition,[14,15] are only applicable to few organic substances that survive a thermally enforced vacuum sublimation.[16−20] Liquid-phase deposition techniques, as drop-casting or spin-coating,[16] are based on chemical solutions, thus unable to incorporate most of the organic pigments with promising semiconductive properties, owing to their insolubility in almost all of the liquid media. The latter drawback hence limits the processing of the organic pigments without a chemical functionalization that otherwise enables their dissolution.[16−20] However, the customized synthesis of functionalized semiconductors is expensive, particularly in relation to the standard pigments already being used in the industry.

Hence, due to the above limitations, an alternative deposition approach was developed, termed as the "organic solid−solid wetting deposition" (OSWD).[17−21] This new deposition approach possesses several advantages, such as being environmental friendly, cheap, and both straightforward and quick to perform under ambient conditions. To induce the OSWD, typically a powdered organic semiconductor such as quinacridone, acridone, or perylenetetracarboxylic dianhydride (PTCDA) is dispersed in a dispersing agent and then drop-casted on a substrate, such as graphite, graphene, carbon nanotubes, or MoS_2.[18−20,25] Subsequently, two-dimensional (2D) adsorbates are formed directly from the three-dimen-

Received: September 26, 2017
Published: January 9, 2018

sional (3D) particles, as the dispersed particles get in touch with the substrate. The deposition is driven by the solid−solid wetting effect,[22−24] with a gradient of the surface free energy serving as the driving force. Applications of the OSWD have become relevant, for example, in the fields of low-dimensional crystal engineering on surfaces,[21,26,27] the chemical doping and bandgap engineering of graphene,[19] and in the fabrication of organic field-effect transistors.[16]

However, until now, lack of profound understanding of the physicochemical basis of the OSWD has restricted this technology to a narrow range of suitable dispersing agents. This limitation prevented the broader development of ways to catalyze the basic effect and hence excluded its possible applications in (bio)nanotechnology. Thus, the aim of the current study was to provide a detailed model of the OSWD process by identifying the contributing physical and chemical forces and the required environmental conditions. For this, an example system built by a highly oriented pyrolytic graphite (HOPG) as the substrate and dispersed crystalline particles of the organic semiconductor γ quinacridone (γQAC) as the adsorptive was employed. γQAC was chosen in this regard owing to its absolute insolubility in water[35−38] and in common organic solvents at atmospheric pressure,[30,38] making it thus highly suitable for solid−solid wetting studies. Further, among the various QAC polymorphs that have been identified so far, γQAC was found to be the most stable form,[38] possessing further promising electrical properties, low toxicity, excellent physical and chemical stability,[28−34] and being easily available as a commercial pigment. With the aid of the example system, the OSWD process was explored *ceteris paribus* by analyzing various dispersions in terms of particle size, zeta (ζ) potential, pH, and by imaging QAC adsorbate structures via scanning tunneling microscopy (STM). Additional insights were obtained via force-field simulations and calculations based on a refined DLVO theory that integrates fluctuation-induced forces.

■ THE SPECIFICS OF THE OSWD

How Can the OSWD Be Induced? In a standard OSWD preparation procedure, a fine powder of organic molecular crystals (for instance, organic pigments, organic semiconductors) is mixed with a liquid (as organic liquids, water), with the powder share representing 2−10 wt %. The insoluble molecular crystals form a particle dispersion in the mixture, thereby the liquid acting as the dispersing agent. These dispersed organic crystals are next drop-casted under ambient conditions onto an inorganic substrate, such as graphite. Depending on the chosen dispersing agent, the result of the OSWD can be probed via STM under ambient conditions either directly by scanning within the dispersion or by scanning the sample after the drop-casted dispersion is dried and the dry sample surface is subsequently covered with a thin layer of a liquid alkane. For the latter, a liquid alkane was found to neither trigger OSWD nor form supramolecular assemblies, it just has the function of preventing the formation of a contamination layer, condensed from the air.[39,40] Further, though the preparation procedure is very straightforward in itself, understanding the OSWD formation process, and the outcomes of the technique are very challenging and are the aim of this study.

What Is the Result of the OSWD? OSWD results in the formation of 2D adsorbate monolayers directly from insoluble but dispersed 3D particles.[17−19] Regarding our example system, QAC molecules (Figure 1) form one-dimensional (1D) supramolecular chains via NH···O═C hydrogen bonding. The supramolecular chains have a uniform width of 1.63 nm and can arrange into multiple parallel and side-by-side appearing arrays (Figure 2).[18] In large-scale STM scans, these arrays are imaged as linear features and domains, as can be seen in the Figure 4. Further, QAC bilayer structures were found occasionally, indicating their detectability but absence in most of the images (refer Supporting Information for related example images).[18]

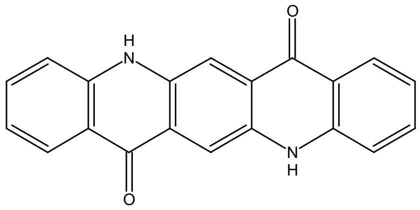

Figure 1. Chemical structure of the QAC molecule.

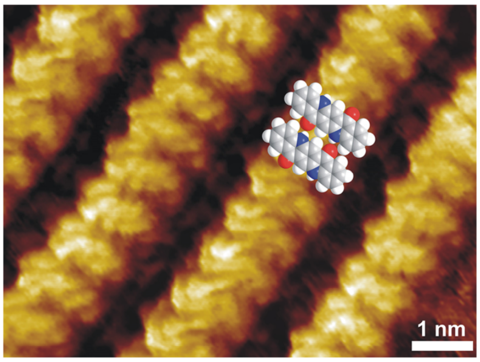

Figure 2. STM close-up view of an QAC adsorbate layer, generated via the OSWD. Additionally, an inlay showing the force field simulated arrangement of two QAC molecules highlights how supramolecular chains are formed via NH···O═C hydrogen bonds.

What Is the Role of the Dispersing Agent? Over a period of several weeks, the simple coverage of the HOPG substrate with dry γQAC powder does not lead to adsorbate structure formation, according to our STM analysis. This result corresponds to previous findings, showing that the OSWD cannot be triggered even by heating up γQAC powder atop a HOPG to a temperature of 160 °C.[19] In addition, experiments were performed to generate QAC adsorbate structures by grinding γQAC powder on a HOPG using a metal spatula. Results revealed that soft grinding does not lead to the formation of supramolecular QAC structures on the HOPG surface, whereas a harsher grinding damages the HOPG surface, making STM analysis thus impossible. In summary, these results hence indicate that at ambient conditions, the OSWD cannot be triggered without a dispersing agent.

Now the question that arises here is why is the presence of a dispersing agent so vital for an OSWD to occur under ambient conditions? To answer this, the impact of different dispersing agents on the performance of the OSWD process was studied to analyze the respective surface coverage with adsorbate arrays. For this, a series of tests were initiated, using both organic liquids and purified water as the dispersing agents. Results revealed that the median of the overall surface coverage of the HOPG by QAC adsorbate structures (including both single

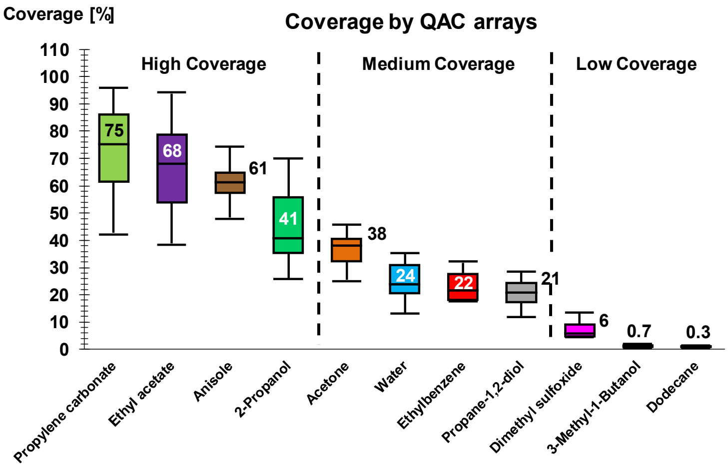

Figure 3. Box plot diagram of the coverage of the HOPG surface by QAC adsorbates, corresponding to the dispersing agents used for the sample preparation. With the specified values referring to the median of the surface coverage, the different samples have been roughly classified into three classes to compare the effectivity of the OSWD in a straightforward way: "High Coverage", comprising samples with an average coverage of 100–40%; "Medium Coverage", comprising samples with an average coverage of 40–15%; and "Low Coverage", incorporating samples with no QAC arrays but single occurring QAC chains with an average coverage of 15–0%.

appearing 1D QAC chains and 2D QAC arrays) differs appreciably, depending on the dispersing agent in use (Figure 3). The lowest median of the surface coverage rate was found when dodecane was employed (0.3 ± 0.3%, including twice the standard deviation), whereas the highest coverage of 75 ± 19% was achieved for the propylene carbonate case. The obtained results hence suggest that the role of the dispersing agent is to catalyze the OSWD process, for it to be occurring under ambient conditions.

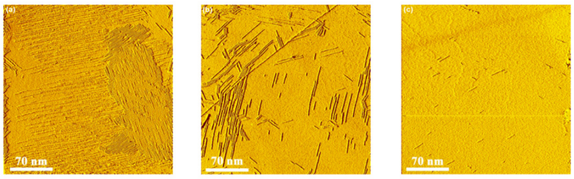

Figure 4. STM images showing exemplary the HOPG surface coverage (SC) by QAC adsorbates that have been generated using different dispersing agents. The surface coverage classified as the "High Coverage": (a) Ethyl acetate, SC = 65 ± 15%; the "Medium Coverage": (b): Propane-1,2-diol, SC = 20 ± 5%; and the "Low Coverage": (c) 3-Methyl-1-butanol, SC = 0.7 ± 0.7%.

■ EXPERIMENTAL IDENTIFICATION OF PARAMETERS INFLUENCING OSWD

The results obtained so far suggest that the quantity of supramolecular adsorbate structures generated via OSWD is related to the properties and conditions of the catalyzing dispersing agent in use. To further investigate this finding, efforts were made to correlate different physical properties of the used dispersing agents to the median of the achieved surface coverage rate. The coefficient of determination R^2 (square of the Pearson correlation coefficient R) was used in this regard to quantify the degree of a potential (linear) correlation (refer Supporting Information for more details on the related scatter plots).

Which Parameters Do Not Influence the OSWD? The results of our investigations yield no correlation between the surface coverage and the viscosity (R^2 = 3%), the permittivity (R^2 = 0.7%), the surface tension (R^2 = 2%), or the vapor pressure (R^2 = 6%) of the investigated dispersing agents. However, worth examining here is could the dispersing agents in any way cause specific modifications to the properties and conditions of the dispersed γQAC crystals? It is a well-known fact that the particle size distribution of a dry powder alters when dispersed, owing to agglomeration and anti-agglomeration processes.[42] Additionally, the size of a nanocrystal influences its surface free energy,[41] indicating a potential relationship between the crystal size and the effectivity of the OSWD process. However, a corresponding analysis yielded R^2 = 34% for a correlation between median particle size and surface coverage, indicating thereby no significant impact of the particle size on the OSWD process (refer Supporting Information for figures depicting the particle size analysis).

Which Parameters Influence an OSWD? An important consequence of the dispersing procedure is the generation of surface charges that induce a ζ potential. The ζ potential is generally known to significantly determine the interdependency of dispersed particles, irrespective of whether the dispersing agent is a polar or nonpolar liquid.[42,43] Additionally, Zhao et al. could demonstrate that the surface free energy of a solid is modified via surface charges,[48] indicating a possible relationship between the ζ potential and the solid−solid wetting processes. Measurements in this regard revealed that each dispersing agent generates its individual ζ potential distribution (refer the Supporting Information for a corresponding diagram depicting all the determined ζ potential distributions).

It has further been shown by Zhao et al. that the surface free energy of a solid drops with an increasing surface charge,[48] suggesting that triggering an OSWD process may be promoted by dispersed γQAC particles, exhibiting a high ζ potential. Based on this, key indicators of the determined ζ potential distributions, representing the strongly charged γQAC fractions, have been examined for a potential correlation. As a result, a significant correlation (R^2 = 74%) was found between the surface coverage and the z33 value, referring to the point where 33% of the ζ potential distribution is more negative and 66% is more positive (Figure 5). The result indicates a significant influence of the ζ potential on the OSWD process, as it can be assumed that the OSWD process is governed by a complex balance of interactions between various components in the system, making the determination of a linear independence of the achieved surface coverage and a physical parameter implausible. It was thus decided to further explore the potential of directing and fine-tuning the OSWD process via modifying the ζ potential.

DOI: 10.1021/jacs.7b10282
J. Am. Chem. Soc. 2018, 140, 1327−1336

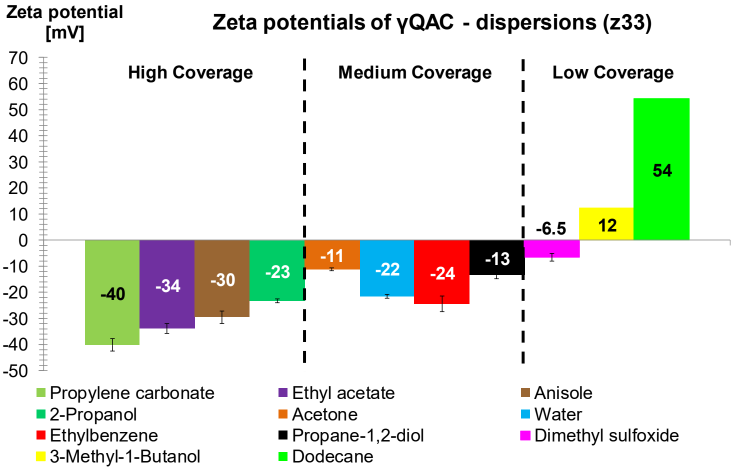

Figure 5. Comparison of the ζ potential values z33 (i.e., the point where 33% of the distribution is more negative and 66% is more positive), derived from γQAC dispersions with varying dispersing agents. The error bars indicate twice the standard deviation. Please note that the measuring method determining the ζ potential distribution failed in dodecane and in 3-methyl-1-butanol. The indicated ζ potential values were thus determined by an alternative measuring method yielding an average value that demonstrates the γQAC crystals in dodecane and in 3-methyl-1-butanol to be conversely charged. However, to guarantee comparability, these average values were not incorporated in the correlation analysis.

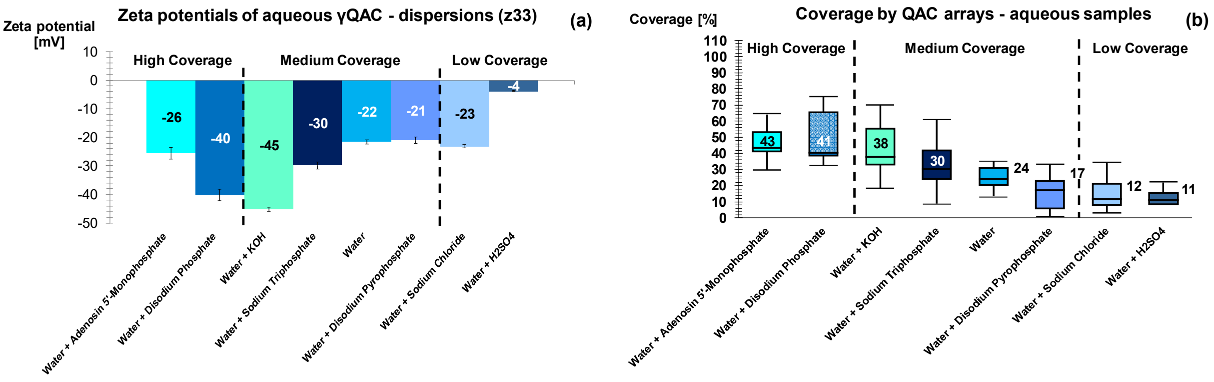

Figure 6. (a) Depicting of the ζ potentials (z33) of aqueous γQAC dispersions modified via different salts, the acid H_2SO_4, and the base KOH. (b) The corresponding median values of the HOPG surface coverage rates.

■ FINE-TUNING ζ POTENTIALS IN AQUEOUS DISPERSIONS TO UNDERSTAND BETTER THE OSWD

The well-established concept describing the origin of the ζ potential is based on the model of the electrical double layer.[44] Dissociated salts play a decisive role within this model (i.e., ions), as they modify the surface charge of dispersed particles and the extent of the diffuse layer. Thus, in order to fine-tune ζ potentials in a *ceteris paribus* approach to obtain a deeper understanding of the OSWD process, modification of the ζ potential with the aid of different salts was attempted. In this regard, phosphate salts, like sodium triphosphate, disodium phosphate, and disodium pyrophosphate, are known to stabilize aqueous dispersions by pushing the ζ potential to a higher electronegative region.[46] Tests were additionally performed using sodium chloride, the most common salt worldwide, and adenosine 5′-monophosphate disodium salt, serving as a main source of energy in biological cells.[45]

Analysis revealed that the addition of salts to the aqueous γQAC dispersions led to modification of the z33 value in the range of −4 to −45 mV (Figure 6a), resulting thus in the median of the surface coverage (SC) of the HOPG to be between 12 and 43% (Figure 6b). Three salts that increased the coverage in this respect were: adenosine 5′-monophosphate disodium (SC = 43%), disodium phosphate (SC = 41%), and sodium triphosphate (SC = 30%). Further, the addition of disodium pyrophosphate (SC = 17%) and sodium chloride (SC = 12%) had a tendency toward constraining the assembly of the QAC arrays.

As the ζ potential is also related to the pH for obvious reasons,[46,47,50] tests were thus performed toward exploring the potential influence of the pH value on the OSWD process. It was found that the addition of salts modifies the pH value (Figure 7), and further analysis revealed a tendency toward a dispersion with a high pH inducing a high surface coverage (Figure 6b). Additional tests revealed that increasing the pH by adding a base (KOH) shifts the ζ potential to a more negative side (Figure 6a) and increases the resulting surface coverage (Figure 6b), whereas such an effect was observed to be reversed by the addition of an acid (e.g., H_2SO_4). Further, the coefficients of determination for the pH (R^2 = 55%) and the z33 of the aqueous samples (R^2 = 58%), show evidence of a

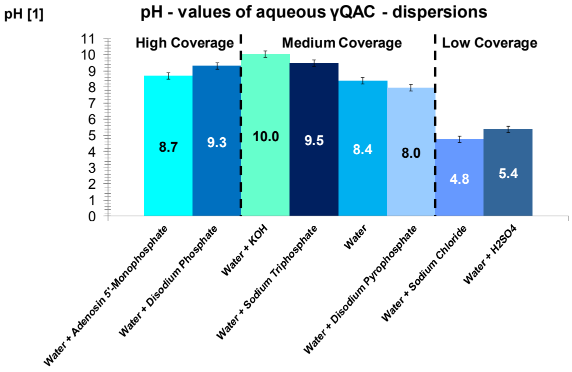

Figure 7. Comparison of the pH values of the analyzed aqueous γQAC dispersions, treated with either salts, H_2SO_4 or KOH.

correlation of these parameters to the surface coverage as well. To evaluate the potential influence of the substrate's surface charge (generated as soon as the HOPG is wetted by a dispersion) on the OSWD process, additional measurements were performed to analyze the ζ potential of graphite particles dispersed within the hitherto analyzed aqueous systems. Results revealed no significant correlation ($R^2 = 26\%$) of the z33 of the HOPG to the achieved surface coverage (Figure 8).

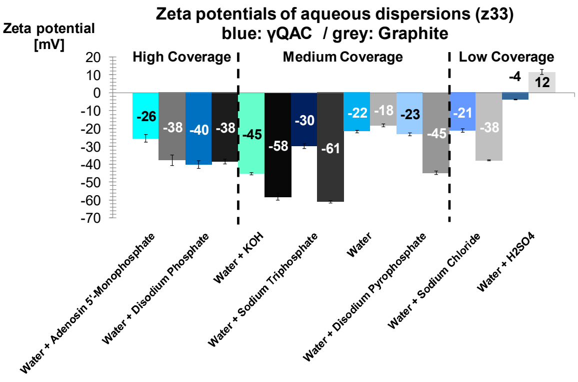

Figure 8. Comparison of the ζ potentials (z33) of dispersed γQAC crystals and graphite powder (equivalent to the z33 of the HOPG surface) in all the tested aqueous systems.

However, a question that arises here is can these results be influenced by chemical interactions related to the performed pH modifications or the addition of a salt? Within the pH range of 1−12, QAC molecules were found to be chemically stable, and the crystal structure of QAC polymorphs was found to be unaffected by pH modifications.[49] Further, experimental results revealed that Na^+, Cl^-, and SO_4^{2-} ions, added to aqueous systems in concentrations of ≥0.1 mol l^{-1}, do not react chemically with QAC (the salt concentrations used within this study were below 0.0043 mol l^{-1}).[49] Thus, for an OSWD process, the participation of pH related chemical processes or chemical reactions between the added salts and QAC can be excluded.

In addition, with γQAC being both chemically inert and strongly hydrophobic,[35−38] the ionization of surface groups and a related strong affinity for ions can be excluded.[50] Moreover, several studies yielded no specific adsorption of ions by hydrophobic surfaces below a salt concentration of 0.01 mol l^{-1}, except for the adsorption of hydroxyl ions.[50] Experimental investigations and molecular dynamics simulations in this regard revealed that the water molecules form an oriented ice-like structure at extended hydrophobic surfaces, as a result of the competition between the tendencies of the liquid to maximize the number of hydrogen bonds and to maximize the packing density.[51] The water structuring makes hydrogen bonds between hydroxyl ions and water molecules energetically favorable, leading to the preferential adsorption of hydroxyl ions and their subsequent stabilization.[50,51] Accordingly, the modification of the ζ potential by the addition of salt is solely related to the simultaneously occurring modification of the pH, but is not related to the adsorption of salt ions, provided that the salt concentration remains low.[50] Thus, referring to the low salt concentrations used within this study, we conclude that supramolecular interactions between the added salts and the surface molecules of the dispersed γQAC particles do not have a significant impact on the via OSWD generated surface coverage.

Summarizing the results obtained so far, it can hence be said that under ambient working conditions, triggering of the OSWD requires a catalyzing dispersing agent. Outcomes further indicate that the gradient of the surface free energy between an organic semiconductor and the substrate surface is related to the ζ potential. Besides, fine-tuning the ζ potential and the related pH via salts, acid or base added to aqueous dispersions enables the control of the OSWD in terms of the surface coverage, opening the way to a deeper understanding of the OSWD process via theoretical approaches.

■ THEORETICAL APPROACHES TOWARD UNDERSTANDING THE OSWD

DLVO Calculations. To further explore this potential interdependency among the OSWD surface coverage, the gradient of the surface free energy (between an organic semiconductor and the substrate), the related ζ potential, and the pH, an appropriate mathematical model was used. This was done to simulate the approach of a charged semiconductor crystal (γQAC) toward the substrate (HOPG) surface and to approximate the related gradient of the surface free energy. In this regard, it was hardly possible to calculate the local surface free energy, especially when the special case of a solid−solid wetting process is involved. However, the DLVO theory, in this respect, presented itself as a suitable model, enabling the calculation of the potential energy of the interaction between two particles by simply summing up the attractive (i.e., van der Waals) and the repulsive (i.e., double layer or Poisson−Boltzmann, respectively) components, as a function of their separation.[42]

Further, though the traditional DLVO model has well demonstrated its validity in describing colloidal dispersions,[43] it is comprised solely of the repulsive forces between like-charged particles, described via the Poisson−Boltzmann theory, entirely neglecting the fluctuation-induced forces, that is, the interactions due to correlations in charge fluctuations and the effects of induced polarization charges at the dielectric discontinuities (i.e., the image charges).[55−61] As the origin of these fluctuation-induced forces can be described similar to the origin of the Casimir effect, they are often called "Casimir-like" forces.[58,59] Under certain conditions, as they can prevail in complex nanosystems, these Casimir-like forces attain a sufficiently large magnitude, such that the solution of the Poisson−Boltzmann equation remains no longer valid. For instance, intensive charge

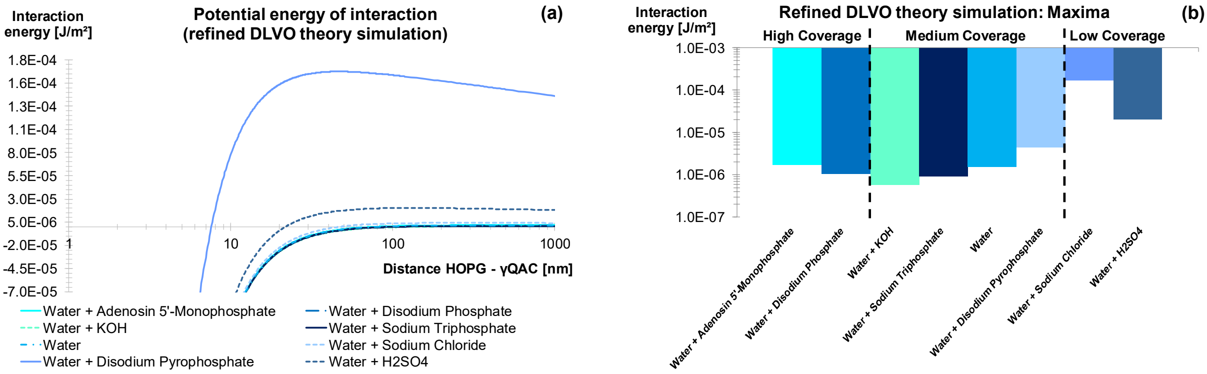

Figure 9. Refined DLVO simulations of the investigated aqueous samples, including fluctuation-induced forces (calculations done using solely the concentration of the H_3O^+ ions), with results depicting: (a) the complete interaction energy functions and (b) comparison of the interaction energy maxima.

fluctuations can turn the repulsive interaction between two like-charged particles into an attractive one.[56−61] Thus, to incorporate forces induced by the fluctuations of the counter-ions, the surface layer-charges, and the coupling of both, the traditional DLVO theory, as per the work of Lukatsky and Safran, was modified and termed the "refined DLVO theory".[64] The related simulations can be applied for particle separations significantly smaller than the Goy−Chapman length, which is approximately 10 μm for our aqueous systems.

According to several estimations, measurements and force field calculations (for details, refer the Supporting Information), we concluded that the interactions among the semiconductor crystal and the underlying substrate surface can be best described by the DLVO model for the plate-like interactions.[42] The performed refined DLVO simulations, based on this model, consider solely H_3O^+ ions, the related concentrations being derived from the corresponding pH values. Now, why is the focus set on H_3O^+ ions? Answering this, it can be said that one of the major parameters affecting the DLVO simulation is the concentration of counterions, forming the diffuse part of the electrical double layer. Hence, considering the positively charged counterions being present in the different aqueous systems, as explored in this study, results revealed the consistent presence of H_3O^+, whereas the phosphate salts and the sodium chloride delivering Na^+ and KOH delivering K^+, respectively. These ions differing significantly in their spatial extensions, an OSWD can however only take place if a semiconductor crystal is located well within the operating distance of the π−π interactions that drive the deposition of the molecules during the OSWD process, that is, within approximately 3.8 Å.[53]

Considering the dimensions of the phosphate salts (roughly calculated by adding up the van der Waals diameters), the spatial extent of the smallest ion in this respect, disodium phosphate, was estimated to be 11.88 Å.[54] Hence, the two opposing double layers, consisting at least of two layers of phosphate ions and two layers of Na^+ ions (4.54 Å), would have a smallest layer thickness of 32.84 Å, thereby making the probability of wide-stretching phosphate salts directing the OSWD very unlikely. Further, it was found that the structuring of water molecules around hydrophobic objects (such as γQAC particles and the HOPG substrate)[35−38] prevents the adsorption of salt ions, as stated above. Additionally, the findings of molecular dynamics simulations show that small hard (nonpolarizable) ions, such as alkali cations, are repelled from the surface of a hydrophobic object within a range of approximately 4 Å, in accordance with the standard Onsager−Samaras theory.[50-52] Nevertheless, simulations considering the actual salt concentration of the investigated aqueous samples, by applying both the traditional and the refined DLVO theory, were performed in addition; the results derived using the actual salt concentrations, however, depicting no correlation to the corresponding surface coverage. A detailed discussion of these simulations can be found in the Supporting Information.

The results of the appropriate, refined DLVO simulations considering solely H_3O^+ ions revealed that although for all the samples the curve progressions are similar in nature, the repulsive energy barrier level (i.e., the interaction energy maximum) of the sample modified with disodium phosphate is significantly higher than for all the other aqueous samples (Figure 9a). In depth analysis in this regard revealed that the repulsive energy barrier decreases exponentially with increasing pH (with all other conditions being kept identical), since the refined DLVO theory corresponds in mathematical terms to a logarithm function (a diagram depicting this finding can be found in the Supporting Information). As a result, a potential correlation between the interaction energy maxima (Figure 9b) and the achieved surface coverage cannot be evaluated by determining the coefficient of determination R^2 directly using linear regression methods. Consequently, a logarithm function was fit to the data as regression function, and the regression function was transformed in a quasilinear function using logarithmic principles. The coefficient of determination thus obtained yields $R^2 = 47\%$, indicating a correlation between interaction energy barrier and surface coverage.

Results further revealed that modifying the catalyzing aqueous dispersion via ions does not only affect the ζ potential of the dispersed semiconductor particles but also modifies the interaction forces between the semiconductor particle and the substrate.

Force Field Calculations. The fundamental question that required understanding for the development of an OSWD model is how a γQAC crystal geometrically interacts with the substrate surface during the OSWD process. The findings of previous experiments showed that the migration of the adsorbed QAC molecules (which is related to the surface diffusion) is limited up to temperatures of 160 °C.[19] Further, the interactions that drive the deposition of the molecules during the OSWD process have a limited operating range, with a maximum of approximately 3.8 Å for the case of $\pi-\pi$ interactions.[53] This indicates that a distinct supramolecular QAC array is built by the detachment of a single crystal face of a γQAC crystal in contact to the substrate surface. To test the feasibility of the assumption of such a detachment, force field calculations were performed. This was done to compare the binding energies of the QAC molecules within different crystal faces of a γQAC nanoparticle with their interaction to a (0001) graphite surface, in order to investigate if γQAC crystal faces exist that contribute to the OSWD process. Such calculations allow for the simulation of relatively large chemical systems, such as complex organic crystals with sizes of several unit cells (Figure 10).

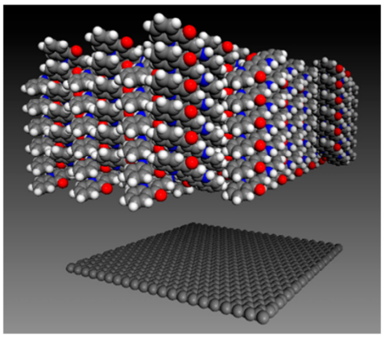

Figure 10. Force field calculated simulation of a γQAC crystal facing a HOPG substrate.

Initial calculations were performed using the Dreiding force field. Results revealed that a γQAC crystal comprises at least one crystal face ((010)) that would release molecules upon contact to the graphite substrate, owing to the comparative lower binding energy of the former (Figure 11). To estimate the accuracy of the obtained energy values, γQAC crystals were modeled with twice the number of γQAC unit cells in each of the directions (refer the Supporting Information). The results indicated an error of ±1.5 kcal/mol, with all the deviations following a physical plausible trend: a slight decrease in the energy values with an increasing crystal size. For further verification of the results, two additional force fields for comparative studies were used: universal force field (UFF) and consistent valence force field (CVFF). Comparison of these results with the Dreiding values revealed that the energy relation between the (010) crystal face of the γQAC and the graphite substrate could be reproduced with all the used force fields (Figure 11). Moreover, the energy values obtained via the Dreiding force field and the UFF have been found to be in the same size range as the published lattice energies of the γQAC.[62] This is in contrast to the CVFF calculations, which are well-known to overestimate the cohesive energies of the aromatic molecules (such as QAC) by 80% in comparison to the experimental values.[63]

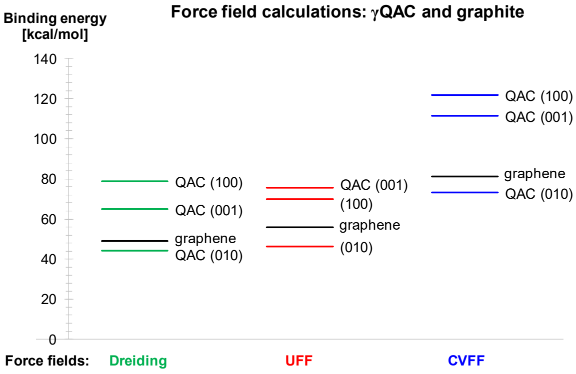

Figure 11. Results of the force field calculations. The image displays the calculated binding energies of a QAC molecule within specific crystal faces of a γQAC crystal (colored lines), and of a single QAC molecule adsorbed on a (0001) graphite layer (black lines), derived from three different force fields, viz. the Dreiding, the UFF, and the CVFF.

Summing it up, the results of the force field calculations support the assumption that a distinct supramolecular QAC array is built by the detachment of a single crystal face of a γQAC crystal in contact with the graphite surface. However, the sum of our experimental and theoretical results requires participation of additional forces to the OSWD process, which plays an important role for proposing a suitable model of the OSWD. This is done next.

■ THE OSWD MODEL: GROWTH OF 2D ADSORBATES DIRECTLY FROM 3D PARTICLES

Based on the above results, the following model (Figure 12) is proposed: The dispersing agent charges the surfaces of both the dispersed organic crystals and the wetted substrate, thereby generating ζ potentials. The generated potential depends on the dispersing agent in use and further on the pH, in the case of aqueous dispersions.

Crystal−Surface Distance $\leq$100 nm. A dispersed organic crystal, approaching the substrate surface by Browninan motion, encounters a repulsive barrier at a distance of about 100 nm. This barrier is generated by the double layer forces originating from the charge distribution around the surfaces. However, clearly negative charged crystals are able to overcome the repulsive energy barrier, since the level of the barrier decreases with an increasing negative ζ potential, according to our refined DLVO calculations. The interplay of the Poisson−Boltzmann related, van der Waals, and fluctuation-induced (Casimir-like, respectively) forces leads to attractive interactions between the dispersed particles and the substrate surface. Further, such an attraction increases with a decrease in distance (between the organic crystal and the substrate surface), as revealed by the refined DLVO approach.

Crystal−Surface Distance $\leq$10 nm. At a distance of about 10 nm and below, the proposed model incorporates an additional force, arising from the hydrophobicity of both the substrate and the dispersed organic semiconductor crystals.[35−38] This additional force can be traced back to a phenomenon that is hardly accessed experimentally or by simulations, owing to its repercussions depending on numerous parameters: the dewetting in a hydrophobic confinement.[67,68] Such a confinement arises when two hydrophobic surfaces approach each other. At small separations of few nanometers, water or another polar organic liquid between the two hydrophobic surfaces becomes metastable (with respect to its vapor), and hence a dewetting transition is triggered, resulting in attractive interactions.[69−71] For the case of fully nonpolar dispersing agents, the expulsion of adsorbed liquid-phase molecules was reported due to the collision among the

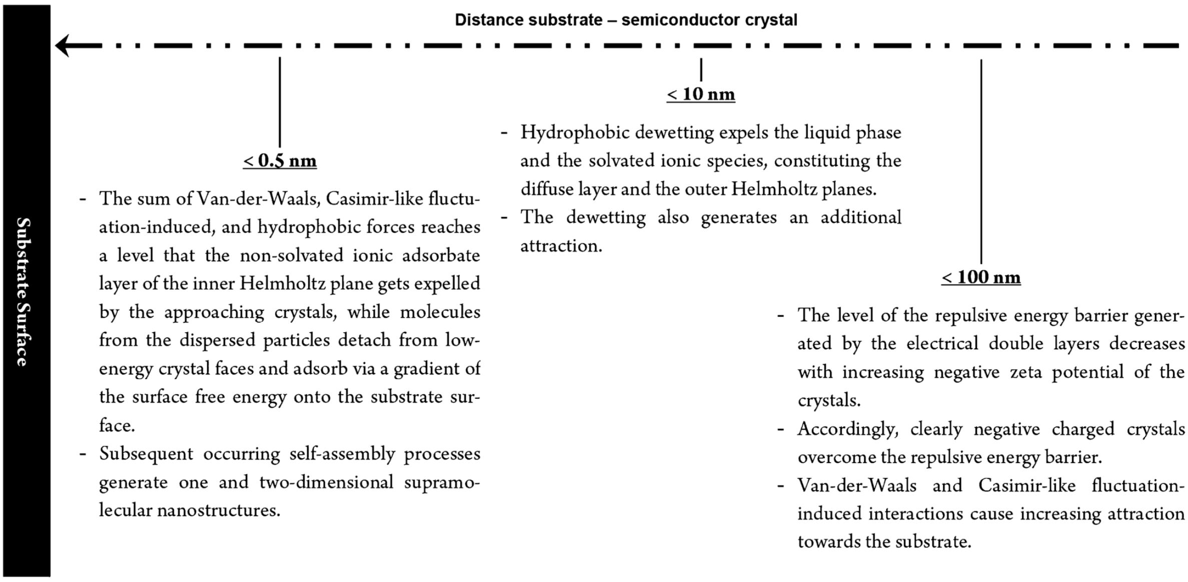

< 0.5 nm

- The sum of Van-der-Waals, Casimir-like fluctuation-induced, and hydrophobic forces reaches a level that the non-solvated ionic adsorbate layer of the inner Helmholtz plane gets expelled by the approaching crystals, while molecules from the dispersed particles detach from low-energy crystal faces and adsorb via a gradient of the surface free energy onto the substrate surface.
- Subsequent occurring self-assembly processes generate one and two-dimensional supramolecular nanostructures.

< 10 nm

- Hydrophobic dewetting expels the liquid phase and the solvated ionic species, constituting the diffuse layer and the outer Helmholtz planes.
- The dewetting also generates an additional attraction.

< 100 nm

- The level of the repulsive energy barrier generated by the electrical double layers decreases with increasing negative zeta potential of the crystals.
- Accordingly, clearly negative charged crystals overcome the repulsive energy barrier.
- Van-der-Waals and Casimir-like fluctuation-induced interactions cause increasing attraction towards the substrate.

Figure 12. Summary of the major processes a semiconductor crystal goes through, as it approaches the substrate surface.

dispersed particles (say, owing to the Brownian motion),[67,72] there being however a lack of appropriate publications analyzing this effect in detail. Nevertheless, from the analogous results, as presented, it can be strongly said that an associated dewetting effect prevails for the nonpolar dispersing agents. Further, our STM results and the limited operating distance of the molecular orbital interactions exclude the presence of an additional, dispersing agent's adsorbate layer, between the semiconductor monolayer and the substrate surface. Thus, it can be proposed that during the approach of the semiconductor crystal toward the substrate, the liquid-phase molecules and the weakly bonded ionic species within the diffuse layer are expelled by the hydrophobic dewetting effects. This is followed by the expulsion of the solvated ions constituting the outer Helmholtz planes of the involved surfaces (as per the Gouy−Chapman−Stern−Graham model of the electrical double layer).[44,66]

Crystal−Surface Distance ≤0.5 nm. The remaining nonsolvated ionic adsorbates, forming the inner Helmholtz planes, induce a steric barrier at a separation of approximately 5 Å between the dispersed organic particles and the substrate. The results of the refined DLVO simulations indicated that when using aqueous dispersions, the inner Helmholtz planes contain a higher share of low-dimensional ionic species, as compared to the composition of the diffuse layer. This phenomenon is referred to the specific adsorption capacities of hydrophobic surfaces, as they generate a layer of ice-like structured water molecules that selectively adsorb hydroxyl ions, whereas other ions are repelled.[50-52] However, the sum of all the attractive forces, including the hydrophobic dewetting interaction, reaches such a level at this separation that the remaining ionic adsorbates of the inner Helmholtz planes are also expelled, thereby eliminating the steric barrier. Such a model was further found in accordance with the findings of corresponding experiments.[67,72] Hence, it can be proposed that a strong physical contact between the organic crystal and the substrate surface is established during the expulsion of the inner Helmholtz planes. Further, the simultaneous expulsion of the ionic adsorbates and the strong, direct physical contact between the semiconductor crystals and the substrate surface triggers the OSWD, if the facing semiconductor crystal plane exhibits a lower binding energy as compared to the substrate surface. Consequently, the semiconductor molecules detach from the semiconductor crystal and attach to the substrate surface.

An essential part of the molecule detachment can be attributed to the properties and conditions of the involved electrical double layers, provided by the inner Helmholtz layers. We propose in this regard that the double layer forces, including Poisson−Boltzmann related and fluctuation induced forces, distinctly strengthen the attraction toward the substrate surface. Hence, the gradient of the surface free energy is modified, and thereby the detachment of the semiconductor molecules is catalyzed. In this respect, the ζ potential z33 was introduced as a comparative value, indicating that more negative is the z33 value, higher is the ultimately generated substrate surface coverage. Further, it can be said that the semiconductor molecules finally attach themselves to the substrate surface via noncovalent bonding, and for the case of a graphitic substrate, mainly via the $\pi-\pi$ stacking. As a result, self-assembly processes are initiated, driven by intermolecular forces and diffusion processes, and directed via epitaxy,[65] leading to the assembly of supramolecular surface adsorbates. However, in accordance with the STM experimental findings, it can be said that the transfer and the assembly of the QAC arrays is completed within seconds or less.[17,20]

■ CONCLUSIONS

Our OSWD model is based on the complex interaction of several basic forces, such as the Casimir-like fluctuation-induced forces, the dewetting-induced hydrophobic collapse, and the electric double layer forces. The model identifies the most important parameters affecting the OSWD process, most notable of them being the ζ potential. Changing the dispersing agent alters the ζ potential and the latter hence allows the selection and modification of the dispersing agents accordingly, as to enable different processing technologies. This became

DOI: 10.1021/jacs.7b10282
J. Am. Chem. Soc. 2018, 140, 1327−1336

especially workable for the aqueous dispersing systems, where adjusting the final surface coverage became straightforward, by the modification of the ζ potential using phosphate salts, acid, or base. All the discovered possibilities of control are not locally restricted and do not require a subsequent rework of the fabricated sample. The identified characteristics of the OSWD point toward the fabrication of low-cost, but large-scale products, as the printed and potentially flexible carbon-based electronics[73] or highly efficient systems to capture carbon dioxide.[74] Further, owing to the identification of water as a suitable dispersing agent, all kinds of nontoxic applications are thus imaginable.

■ MATERIALS AND METHODS

Refined DLVO Simulation, including Fluctuation-Induced forces. To include all kinds of fluctuation-induces forces, we adjusted the traditional DLVO simulation as per the work of Lukatsky and Safran.[64] This enhanced term for the calculation of the potential energy of interaction V_{eT} consists of three subterms: one describing the attractive van der Waals interaction, a second describing the unscreened Poisson−Boltzmann repulsion, and a third treating the effect of fluctuation-induced forces, expressed as

$$V_{eT}(\mathrm{h}) = -\frac{H_{123}}{12\pi} \times \frac{1}{h^2} - \frac{kT}{\pi\lambda l_B}\ln(h) + \frac{7kT}{4\pi\lambda^2}\ln(h) \qquad (1)$$

where h is the separation between the HOPG and the γQAC surface; H_{123} is the Hamaker constant for the system HOPG (index 1), dispersing agent (index 2), and γQAC (index 3); k is the Boltzmann's constant; T is the temperature; λ is the Gouy−Chapman length; and l_B is the Bjerrum length.

Further detailed information describing the single calculations and parameters necessary to perform the refined DLVO simulations can be found in the Supporting Information.

■ ASSOCIATED CONTENT

Supporting Information

The Supporting Information is available free of charge on the ACS Publications website at DOI: 10.1021/jacs.7b10282.

> Experimental details concerning the STM, the ζ potential, the particle size, and the pH measurements. STM pictures related to all the tested dispersing agents, of how to distinguish monolayer from bilayer adsorbate structures, and related to STM measurement artifacts. Detailed correlation analysis related to the physical properties of the examined dispersing agents and scatter plots relating the surface coverage to the particle size, the ζ potential, the pH, and the interaction energy maximum of the investigated systems. Experimental details and results concerning scanning electron microscopy measurements. Further information about the charging mechanism in aqueous systems, leaky dielectrics, and fully nonpolar media. Detailed description on how the surface coverage rate was determined. The specifications of the performed force field calculations. Detailed information on how the γQAC crystal size was calculated via a back calculation and how a suitable DLVO model was chosen. A detailed description of the single calculations and the parameters necessary to perform the traditional as well as the refined DLVO simulations. A detailed discussion of the performed traditional DLVO simulations and further results related to the refined DLVO simulation, including a comparative study exploring the influence of the pH on the DLVO calculations (PDF)

■ AUTHOR INFORMATION

Corresponding Author
*Trixler@lrz.uni-muenchen.de
ORCID
Alexander Eberle: 0000-0002-8067-2522

Notes

The authors declare no competing financial interest.

■ ACKNOWLEDGMENTS

The authors would like to thank Martina Zeiler from the Papiertechnische Stiftung in München for her kind support regarding the ζ potential measurements. Futhermore, we thank Veronika Schömig from the Technische Universität München, Fachgebiet für Selektive Trenntechnik, for her quick and smooth support, enabling us to perform a series of particle size measurements. Big thanks as well go to Manfred Seidel from the Deutsche Museum, München, for all his aid in the field of chemistry and much more. We also acknowledge Klaus Macknapp from the Deutsche Museum, München, for his help and support regarding the SEM analysis. Further, we thank Neeti Phatak for her support with the proofreading and editing of the document. We additionally thank our colleague Andrea Greiner, who came up with the idea of displaying the determined surface coverage via a box plot diagram. Last, but certainly not the least, we thank Wolfgang W. Schmahl and Guntram Jordan for their excellent idea of performing DLVO theory related simulations. The Bayerisches Staatsministerium für Umwelt and Verbraucherschutz and the mentoring program of the Nanosystems Initiative Munich (NIM) are sincerely acknowledged for their funding.

■ REFERENCES

(1) Avouris, P.; Chen, Z.; Perebeinos, V. *Nat. Nanotechnol.* **2007**, *2*, 605−15.

(2) Lu, W.; Lieber, C. M. *Nat. Mater.* **2007**, *6*, 841−50.

(3) Chen, H.-H.; Su, S. H.; Chang, S.-L.; Cheng, B.-Y.; Chen, S. W.; Chen, H.-Y.; Lin, M.-F.; Huang, J. C. a. *Sci. Rep.* **2015**, *5*, 11623.

(4) Tans, S.; Verschueren, A.; Dekker, C. *Nature* **1998**, *672*, 669−672.

(5) Medina, H.; Lin, Y. C.; Obergfell, D.; Chiu, P. W. *Adv. Funct. Mater.* **2011**, *21*, 2687−2692.

(6) Manna, A. K.; Pati, S. K. *Chem. - Asian J.* **2009**, *4*, 855−860.

(7) Long, B.; Manning, M.; Burke, M.; Szafranek, B. N.; Visimberga, G.; Thompson, D.; Greer, J. C.; Povey, I. M.; MacHale, J.; Lejosne, G.; Neumaier, D.; Quinn, A. J. *Adv. Funct. Mater.* **2012**, *22*, 717−725.

(8) Liu, N.; Zhou, Y.; Ai, N.; Luo, C.; Peng, J.; Wang, J.; Pei, J.; Cao, Y. *Langmuir* **2011**, *27*, 14710−14715.

(9) Liu, N.; Zhou, Y.; Wang, L.; Peng, J.; Wang, J.; Pei, J.; Cao, Y. *Langmuir* **2009**, *25*, 665−671.

(10) Zheng, J. Y.; Yan, Y.; Wang, X.; Zhao, Y. S.; Huang, J.; Yao, J. *J. Am. Chem. Soc.* **2012**, *134*, 2880−2883.

(11) Yu, G.; Lieber, C. M. *Pure Appl. Chem.* **2010**, *82*, 2295−2314.

(12) Jordan, B. J.; Ofir, Y.; Patra, D.; Caldwell, S. T.; Kennedy, A.; Joubanian, S.; Rabani, G.; Cooke, G.; Rotello, V. M. *Small* **2008**, *4*, 2074−2078.

(13) Liu, M.; Ji, Z.; Shang, L. In *Nanotechnology, Vol. 8: Nanostructured Surfaces*; Chi, L., Ed.; Wiley-VCH: Weinheim, 2010; pp 17−35.

(14) Zhong, D.; Zhang, H.; Chi, L. In *Nanotechnology, Vol. 8: Nanostructured Surfaces*; Chi, L., Ed.; Wiley-VCH: Weinheim, 2010; pp 357−369.

(15) Kowarik, S.; Gerlach, A.; Schreiber, F. *J. Phys.: Condens. Matter* **2008**, *20*, 184005.

(16) Treier, M.; Orgiu, E.; Zalewski, L.; Cho, D.; Rieger, R.; Müllen, K.; Samorì, P. *J. Mater. Chem.* **2010**, *20*, 9018.

(17) Trixler, F.; Markert, T.; Lackinger, M.; Jamitzky, F.; Heckl, W. *Chem. - Eur. J.* **2007**, *13*, 7785−7790.

(18) Eberle, A.; Nosek, A.; Büttner, J.; Markert, T.; Trixler, F. *CrystEngComm* **2017**, *19*, 1417.

(19) Eberle, A.; Greiner, A.; Ivleva, N. P.; Arumugam, B.; Niessner, R.; Trixler, F. *Carbon* **2017**, *125*, 84−92.

(20) Trixler, F.; Heckl, W. M. In *Modern Research and Educational Topics in Microscopy*; Méndez-Vilas, A., Diaz, J., Eds.; Formatex: Badajoz, 2007; Vol. 2, pp 534−541.

(21) Elemans, J. A. A. W.; Lei, S.; De Feyter, S. *Angew. Chem., Int. Ed.* **2009**, *48*, 7298−7333.

(22) Haber, J.; Machej, T.; Czeppe, T. *Surf. Sci.* **1985**, *151*, 301−310.

(23) Leyrer, J.; Margraf, R.; Taglauer, E.; Knözinger, H. *Surf. Sci.* **1988**, *201*, 603−623.

(24) Bertinchamps, F.; Grégoire, C.; Gaigneaux, E. M. *Appl. Catal., B* **2006**, *66*, 1−9.

(25) Trixler, F. *Curr. Org. Chem.* **2013**, *17*, 1758−1770.

(26) Furukawa, S.; De Feyter, S. *Top. Curr. Chem.* **2008**, *287*, 87−133.

(27) Koepf, M.; Chérioux, F.; Wytko, J. A.; Weiss, J. *Coord. Chem. Rev.* **2012**, *256*, 2872−2892.

(28) Głowacki, E. D.; Tangorra, R. R.; Coskun, H.; Farka, D.; Operamolla, A.; Kanbur, Y.; Milano, F.; Giotta, L.; Farinola, G. M.; Sariciftci, N. S. *J. Mater. Chem. C* **2015**, *3*, 6554−6564.

(29) Głowacki, E. D.; Romanazzi, G.; Yumusak, C.; Coskun, H.; Monkowius, U.; Voss, G.; Burian, M.; Lechner, R. T.; Demitri, N.; Redhammer, G. J.; Sünger, N.; Suranna, G. P.; Sariciftci, S. *Adv. Funct. Mater.* **2015**, *25*, 776−787.

(30) Sytnyk, M.; Głowacki, E. D.; Yakunin, S.; Voss, G.; Schöfberger, W.; Kriegner, D.; Stangl, J.; Trotta, R.; Gollner, C.; Tollabimazraehno, S.; Romanazzi, G.; Bozkurt, Z.; Havlicek, M.; Sariciftci, N. S.; Heiss, W. *J. Am. Chem. Soc.* **2014**, *136*, 16522−16532.

(31) Głowacki, E. D.; Irimia-Vladu, M.; Kaltenbrunner, M.; Gsiorowski, J.; White, M. S.; Monkowius, U.; Romanazzi, G.; Suranna, G. P.; Mastrorilli, P.; Sekitani, T.; Bauer, S.; Someya, T.; Torsi, L.; Sariciftci, N. S. *Adv. Mater.* **2013**, *25*, 1563−1569.

(32) Glowacki, E. D.; Leonat, L.; Voss, G.; Bodea, M.; Bozkurt, Z.; Irimia-Vladu, M.; Bauer, S.; Sariciftci, N. S. *Proc. SPIE* **2011**, *8118*, 81180M−81180M−10.

(33) Głowacki, E. D.; Irimia-Vladu, M.; Bauer, S.; Sariciftci, N. S. *J. Mater. Chem. B* **2013**, *1*, 3742.

(34) Wagner, T.; Györök, M.; Huber, D.; Zeppenfeld, P.; Głowacki, E. D. *J. Phys. Chem. C* **2014**, *118*, 10911−10920.

(35) Sue, K.; Usami, T.; Arai, K.; Kasai, H.; Nakanishi, H.; Hiaki, T. *J. Chem. Eng. Data* **2007**, *52*, 714−717.

(36) De Feyter, S.; Gesquière, A.; De Schryver, F. C.; Keller, U.; Müllen, K. *Chem. Mater.* **2002**, *14*, 989−997.

(37) Keller, U.; Müllen, K.; De Feyter, S.; De Schryver, F. C. *Adv. Mater.* **1996**, *8*, 490−493.

(38) Paulus, E. F.; Leusen, F. J. J.; Schmidt, M. U. *CrystEngComm* **2007**, *9*, 131−143.

(39) Räder, H. J.; Rouhanipour, A.; Talarico, A. M.; Palermo, V.; Samorì, P.; Müllen, K. *Nat. Mater.* **2006**, *5*, 276−280.

(40) Cousty, J.; Pham Van, L. *Phys. Chem. Chem. Phys.* **2003**, *5*, 599−603.

(41) Nanda, K. K.; Maisels, A.; Kruis, F. E.; Fissan, H.; Stappert, S. *Phys. Rev. Lett.* **2003**, *91*, 106102.

(42) Stokes, R. J.; Evans, D. F. *Fundamentals of Interfacial Engineering*; Wiley-VHC, Weinheim, 1997; pp 34−41, 121−163.

(43) Berg, J. C. *An Introduction to Interfaces and Colloids*; World Scientific: Singapore, 2010; pp 455−466, 540−582.

(44) Hunter, R. J. *Zeta Potential in Colloid Science*, 3rd ed.; Academic Press: London; 1988; pp 1−55.

(45) Levy, E.; Cerveny, S.; Ermolina, I.; Puzenko, A.; Feldman, Y. *J. Chem. Phys.* **2012**, *140*, 194502.

(46) Singh, Y.; Deshpande, R. J.; Subramanian, S. *Proceedings of the International Seminar on Mineral Processing Technology*; Allied Publishers: Chennai, 2006.

(47) Chibowski, E. *J. Colloid Interface Sci.* **1979**, *69*, 326−329.

(48) Zhao, Q.; Liu, Y.; Abel, E. W. *J. Colloid Interface Sci.* **2004**, *280*, 174−183.

(49) Jakešová, M.; Apaydin, D. H.; Sytnyk, M.; Oppelt, K.; Heiss, W.; Sariciftci, N. S.; Głowacki, E. D. *Adv. Funct. Mater.* **2016**, *26*, 5248.

(50) Tandon, V.; Bhagavatula, S. K.; Nelson, W. C.; Kirby, B. J. *Electrophoresis* **2008**, *29*, 1092−1101.

(51) Tandon, V.; Kirby, B. J. *Electrophoresis* **2008**, *29*, 1102−1114.

(52) Vrbka, L.; Mucha, M.; Minofar, B.; Jungwirth, P.; Brown, E. C.; Tobias, D. J. *Curr. Opin. Colloid Interface Sci.* **2004**, *9*, 67−73.

(53) Janiak, C. *J. Chem. Soc. Dalt. Trans.* **2000**, *0*, 3885−3896.

(54) Mantina, M.; Chamberlin, A. C.; Valero, R.; Cramer, C. J.; Truhlar, D. G. *J. Phys. Chem. A* **2009**, *113*, 5806−5812.

(55) Attard, P.; Kjellander, R.; Mitchell, D. J.; Jonsson, B. *J. Chem. Phys.* **1988**, *89*, 1664−1680.

(56) Lau, A. W. C.; Pincus, P. *Phys. Rev. E: Stat. Phys., Plasmas, Fluids, Relat. Interdiscip. Top.* **2002**, *66*, 041501.

(57) Lau, A. W. C.; Lukatsky, D. B.; Pincus, P.; Safran, S. A. *Phys. Rev. E: Stat. Phys., Plasmas, Fluids, Relat. Interdiscip. Top.* **2002**, *65*, 051502.

(58) Kardar, M.; Golestanian, R. *Rev. Mod. Phys.* **1999**, *71*, 1233−1245.

(59) Bartolo, D.; Ajdari, A.; Fournier, J.-B.; Golestanian, R. *Phys. Rev. Lett.* **2002**, *89*, 230601.

(60) Hansen, J. P.; Lowen, H. *Annu. Rev. Phys. Chem.* **2000**, *51*, 209−242.

(61) Golestanian, R. *Pramana* **2005**, *64*, 1029−1038.

(62) Panina, N.; Leusen, F. J. J.; Janssen, F. F. B. J.; Verwer, P.; Meekes, H.; Vlieg, E.; Deroover, G. *J. Appl. Crystallogr.* **2007**, *40*, 105.

(63) Feng, J.; Pandey, R. B.; Berry, R. J.; Farmer, B. L.; Naik, R. R.; Heinz, H. *Soft Matter* **2011**, *7*, 2113.

(64) Lukatsky, D. B.; Safran, S. A. *Phys. Rev. E: Stat. Phys., Plasmas, Fluids, Relat. Interdiscip. Top.* **1999**, *60*, 5848−5857.

(65) Hooks, D. E.; Fritz, T.; Ward, M. D. *Adv. Mater.* **2001**, *13*, 227−241.

(66) Jacobasch, H. J.; Simon, F.; Weidenhammer, P. *Colloid Polym. Sci.* **1998**, *276*, 434−442.

(67) Christenson, H. K.; Claesson, P. M. *Adv. Colloid Interface Sci.* **2001**, *91*, 391−436.

(68) Hammer, M. U.; Anderson, T. H.; Chaimovich, A.; Shell, M. S.; Israelachvili, J. *Faraday Discuss.* **2010**, *146*, 299−308.

(69) Remsing, R. C.; Xi, E.; Vembanur, S.; Sharma, S.; Debenedetti, P. G.; Garde, S.; Patel, A. J. *Proc. Natl. Acad. Sci. U. S. A.* **2015**, *112*, 8181−8186.

(70) Huang, B. J. B. X.; Margulis, C. J. *Proc. Natl. Acad. Sci. U. S. A.* **2004**, *100*, 11953−11958.

(71) Berne, B. J.; Weeks, J. D.; Zhou, R. *Annu. Rev. Phys. Chem.* **2009**, *60*, 85−103.

(72) Leong, Y. K.; Scales, P. J.; Healy, T. W.; Boger, D. V.; Buscall. *J. Chem. Soc., Faraday Trans.* **1993**, *89*, 2473−2478.

(73) Park, S.; Vosguerichian, M.; Bao, Z. *Nanoscale* **2013**, *5*, 1727−52.

(74) Apaydin, D. H.; Głowacki, E. D.; Portenkirchner, E.; Sariciftci, N. S. *Angew. Chem., Int. Ed.* **2014**, *53*, 6819−6822.

DOI: 10.1021/jacs.7b10282
J. Am. Chem. Soc. 2018, 140, 1327−1336

2.5. Revealing the Physicochemical Basis of OSWD – Supporting Information

Supporting Information:

Revealing the Physicochemical Basis of Organic Solid-Solid Wetting Deposition: Casimir-like Forces, Hydrophobic Collapse, and the Role of the Zeta Potential

Alexander Eberle,[†,‡] Thomas Markert,[§] and Frank Trixler*[,†,∥]

[†]Department of Earth and Environmental Sciences and Center for NanoScience (CeNS), Ludwig-Maximilians-Universität München, Theresienstraße 41, 80333 München, Germany

[‡]Helmholtz Institute Erlangen-Nürnberg for Renewable Energy, Egerlandstr. 3, 91058 Erlangen, Germany

[§]Institute of Theoretical Chemistry, Ulm University, Albert-Einstein-Allee 11, 89081 Ulm, Germany

[∥]TUM School of Education, Technical University of Munich and Deutsches Museum, Museumsinsel 1, 80538 München, Germany

Reprinted with permission from the *J. Am. Chem. Soc.*, 2018, 140 (4), pp 1327–1336. Copyright © 2018 American Chemical Society. https://pubs.acs.org/doi/full/10.1021/jacs.7b10282

Table of Contents

1. STM sample preparation and scan setting

To prepare a standard scanning tunneling microscope (STM) sample, using a dispersion with 2 wt. % of pigment, 82 mg of powdered γQAC (5,12-Dihydro-quino[2,3-b]acridine-7,14-dione, CAS 1047-16-1, purchased as Hostaperm Red E5B02 from Clariant) was dispersed in 4 ml of the desired dispersing agent. In this regard, the dispersing agents used were: propane-1,2-diol (CAS 57-55-6, from Sigma Aldrich, item no. 82280), 3-methyl-1-butanol (CAS 123-51-3, from Sigma Aldrich, item no. 59090), acetone (CAS 67-64-1, from Sigma Aldrich, item no. 34850), anisole (CAS 100-66-3, from Sigma Aldrich, item no. 10520), dimethyl sulfoxide (CAS 67-68-5, from Sigma Aldrich, item no. 472301), ethyl acetate (CAS 141-78-6, from Sigma Aldrich, item no. 45767), ethylbenzene (CAS 100-41-4, from Sigma Aldrich, item no. 03080), 2-Propanol (CAS 67-63-0, from Sigma Aldrich, item no. 34965), propylene carbonate (CAS 108-32-7, from Sigma Aldrich, item no. 310328), dodecane (CAS 112-40-3, purchased from Sigma Aldrich, item no. D221104), and purified water. For some cases where aqueous samples were used, additionally 0.5 wt. % salt (corresponding to 21 mg for a sample having a volume of 4 ml) was added to the sample mix. Tests were conducted using the salts sodium triphosphate (pentabasic, CAS 7758-29-4, from Sigma Aldrich, item no. 72061), disodium phosphate (dihydrate, CAS 10028-24-7, purchased as di-Natriumhydrogenphosphat-Dihydrat, from Merck Millipore, item no. 1065801000), disodium pyrophosphate (purchased as sodium pyrophosphate dibasic, CAS 7758-16-9, from Sigma Aldrich, item no. 71501), sodium chloride (CAS 7647-14-5, unknown supplier, but purity determined via XPS analysis: ≥ 99,99 %), and adenosine 5'-monophosphate disodium (salt, CAS 4578-31-8, from Sigma Aldrich, item no. 01930). At times, when mentioned, 1 µl of a 2 M potassium hydroxide (KOH) solution (CAS 1310-58-3, pellets purchased from Carl Roth, item no. P747.1), or 2 µl of a 1 M sulfuric acid (H_2SO_4) solution (CAS 7664-93-9, from Walter CMP, item no. 016-020-00-8), was alternatively added.

To begin with, a few drops of the dispersion were dispensed on a highly ordered pyrolytic graphite (HOPG, purchased from NT-MDT, item no. GRBS/1.0). If the dispersing agent didn't vaporize after an exposure time of 10 – 20 minutes, as in the case of propane-1,2-diol, 3-methyl-1-butanol, anisole, dimethyl sulfoxide, ethylbenzene, propylene carbonate, and purified water, the HOPG was dried by a special hotplate, enabling an accurate temperature control and providing a smooth temperature increase (Stuart SD160, temperature accuracy ± 1.0 °C). Once the sample was dried, it was immediately taken off the hotplate. Note, that the heating up of pure γQAC powder to 160 °C without a dispersing agent was unable to induce an OSWD,[1-2] and all the dispersing agents vaporized below 160 °C. Further, creation of two-dimensional QAC arrays, without a dispersing agent, was only possible by heating pure γQAC powder to 240 °C.[1-2]

The ready-made STM samples being investigated within days; as per the previous tests, QAC arrays were revealed to not change their structure for a minimum of four weeks, provided they are not influenced via any external forces.[1] For the STM measurements, we used a home-built STM combined with a SPM 100 control system, supplied by RHK Technology. The scans settings were: bias = 1 V, tunnel current 300 = pA, and the line time = 50 ms. Further, the voltage pulses used to improve the scan quality were located in the range of 4.3 and 10 V. The STM measurements being performed under ambient conditions, a thin layer of dodecane was generally applied on top of the HOPG surface to increase the measurement quality.[6] Extensive tests revealed, that a mixture of dodecane and γQAC, without another dispersing agent, was unable to generate two-dimensional QAC structures and that the dodecane by itself could not form supramolecular assemblies at room temperatures.[7] Besides, to conduct a STM measurement under ambient conditions without dodecane was very challenging, mainly due to the occurrence of a thin contamination layer of adsorbed water on top of the HOPG surface,[3-5] which otherwise was found to be successfully removed using the hydrophobic dodecane.

2. Further STM example pictures

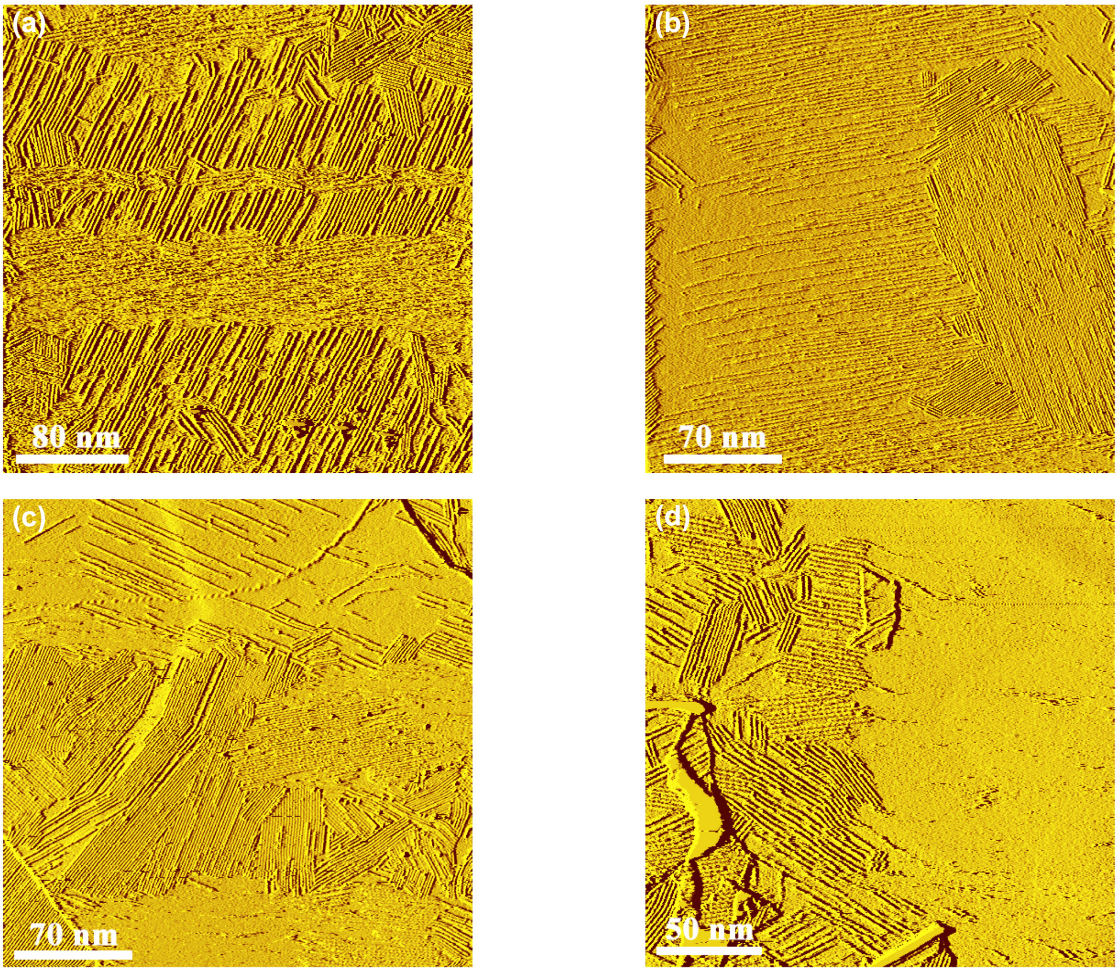

Figure S1. STM images showing exemplary the HOPG surface coverage (SC) by QAC adsorbates, depending on the dispersing agent in use. The surface coverage classified as the "High Coverage": (a) Propylene carbonate, SC = 75 ± 19 %; (b) Ethyl acetate, SC = 68 ± 15 %; (c) Anisole, SC = 61 ± 9 %; and (d) 2-Propanol, SC = 41 ± 14 %.

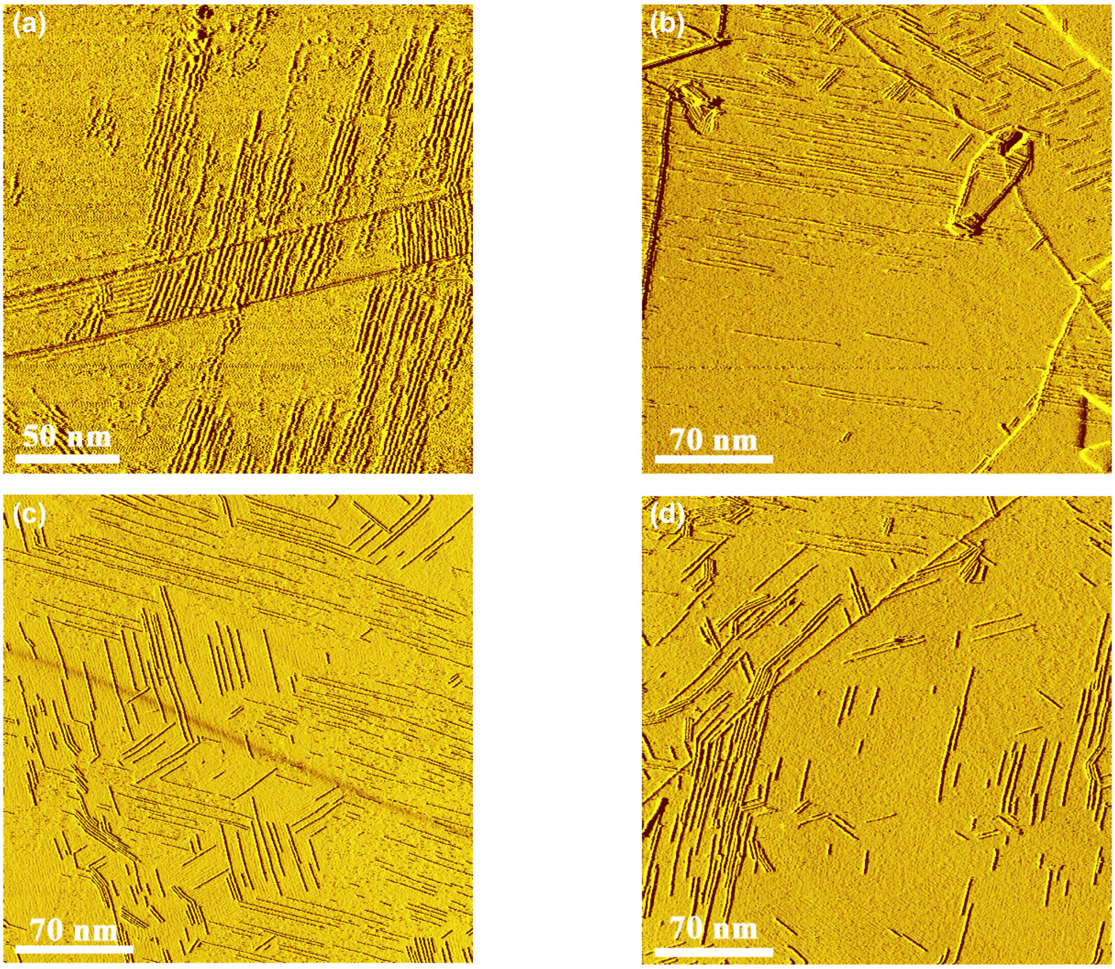

Figure S2. STM images showing exemplary the HOPG surface coverage (SC) by QAC adsorbates, depending on the dispersing agent in use. The surface coverage classified as the "Medium Coverage": (a) Acetone, SC = 38 ± 7 %; (b) Purified Water, SC = 24 ± 7 %; (c) Ethylbenzene, SC =22 ± 4 %; and (d) Propane-1,2-diol, SC = 21 ± 5 %.

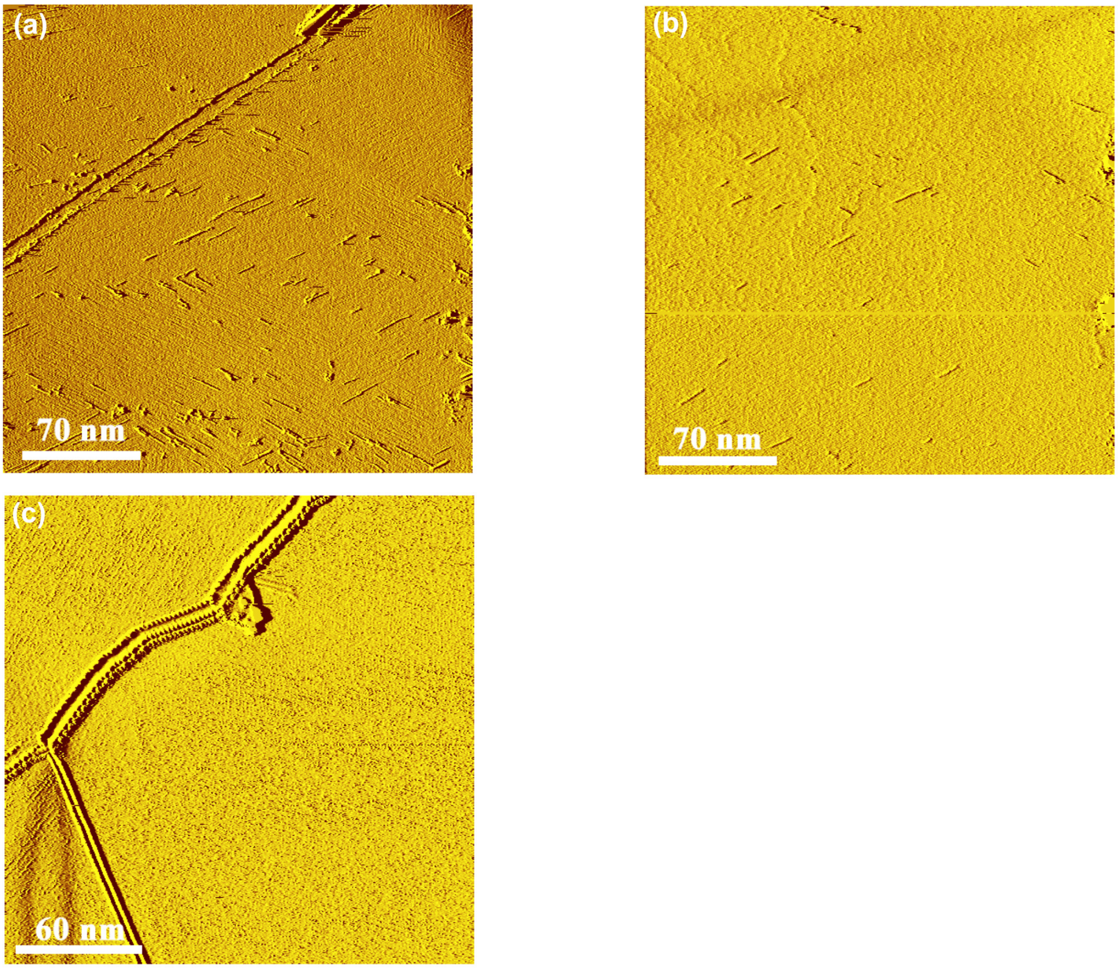

Figure S3. STM images showing exemplary the HOPG surface coverage (SC) by QAC adsorbates, depending on the dispersing agent in use. The surface coverage classified as the “Low Coverage”: (a) Dimethyl sulfoxide, SC = 6 ± 4 %; (b) 3-Methyl-1-Butanol, SC = 0.7 ± 0.7 %; and (c) Dodecane, SC = 0.3 ± 0.3 %.

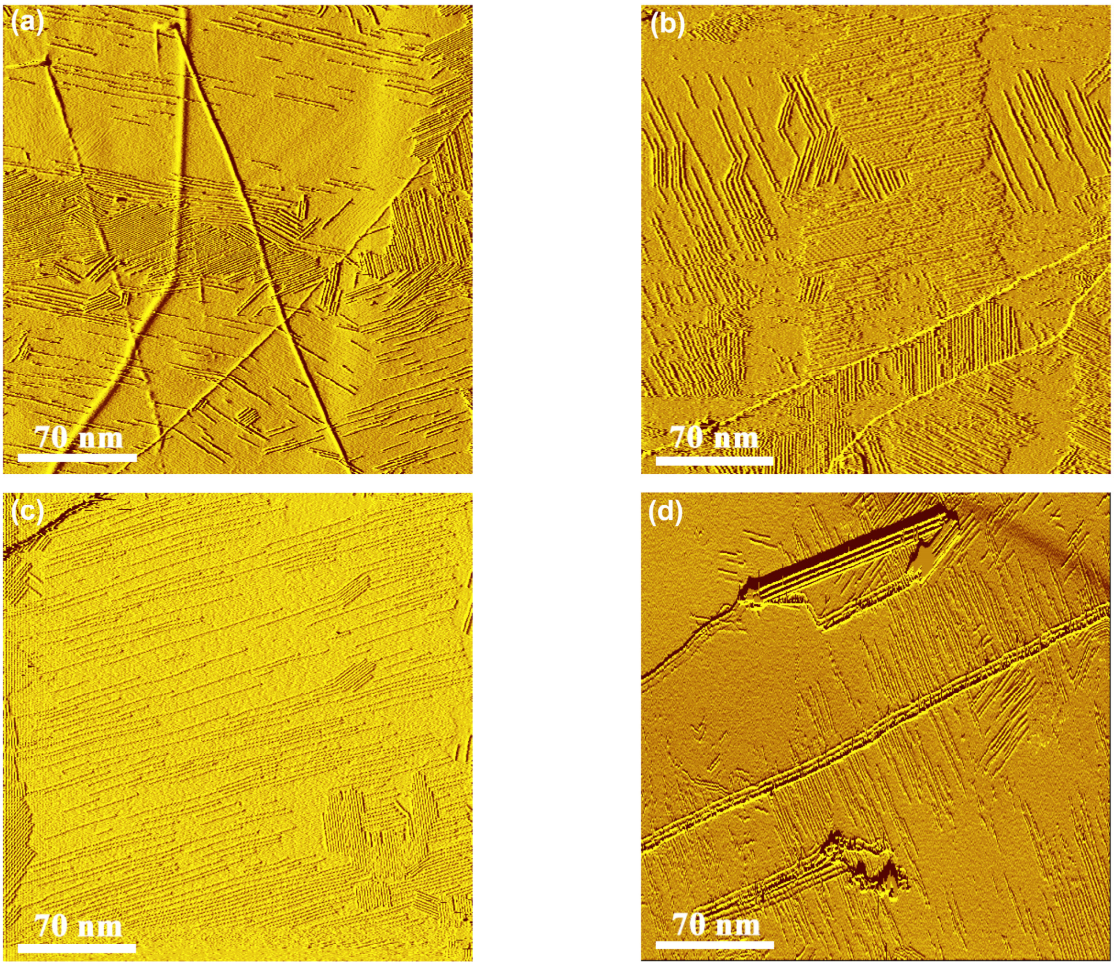

Figure S4. These STM example pictures show QAC surface adsorbates, generated atop a HOPG surface via aqueous γQAC dispersions that have been modified by adding different salts or the base KOH. Classified as the "High Coverage": (a) Adenosine 5'-monophosphate disodium, SC = 43 ± 11 %; and (b) Disodium phosphate, SC = 41 ± 13 % Classified as the "Medium Coverage": (c) KOH, SC = 38 ± 14 %; and (d) Sodium triphosphate, SC = 30 ± 19 %.

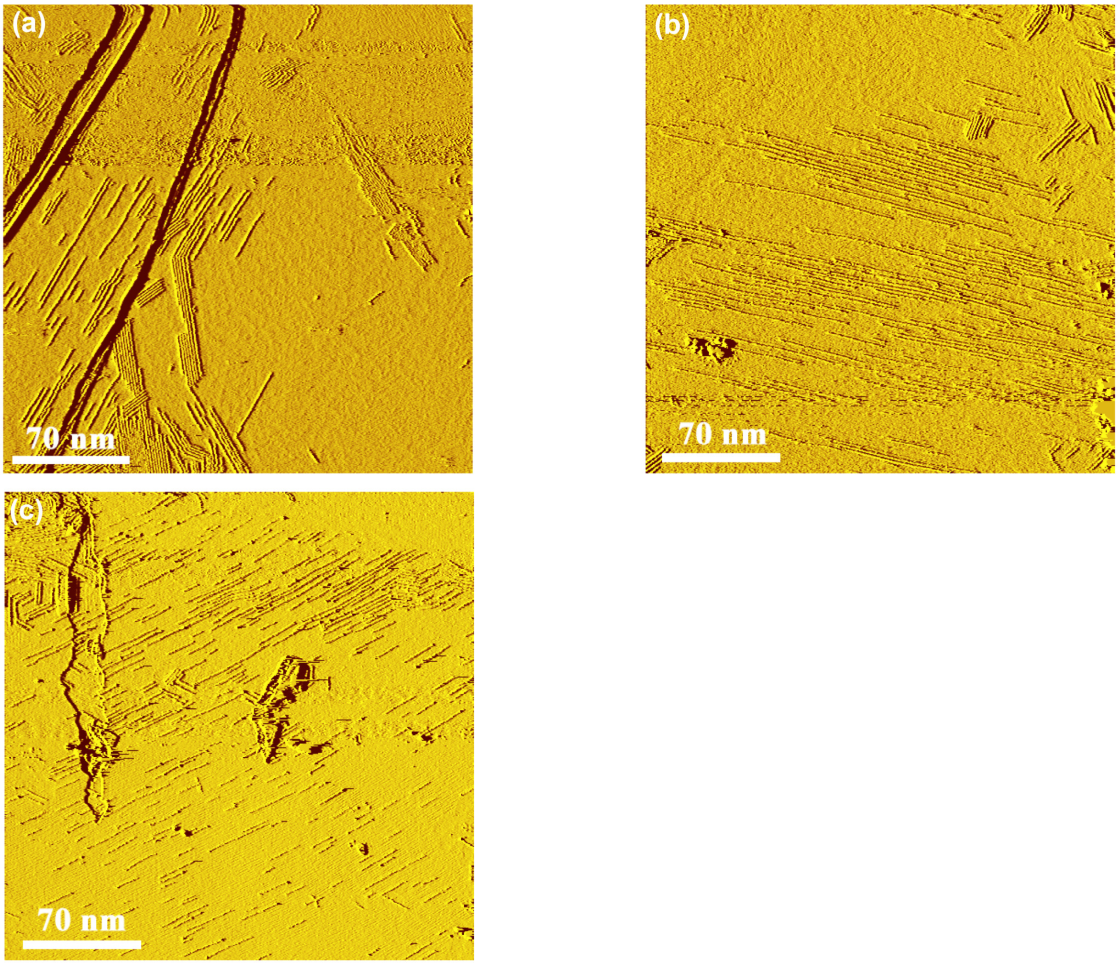

Figure S5. These STM example pictures show QAC surface adsorbates, generated atop a HOPG surface via aqueous γQAC dispersions that have been modified by adding different salts or the acid H_2SO_4. Classified as the “Medium Coverage”: (a) Disodium pyrophosphate, SC = 17 ± 10 %. Classified as the “Low Coverage”: (b) Sodium chloride, SC = 12 ± 13 %; and (c) H_2SO_4, SC = 11 ± 7 %.

3. Distinction between monolayer and bilayer adsorbate structures via STM

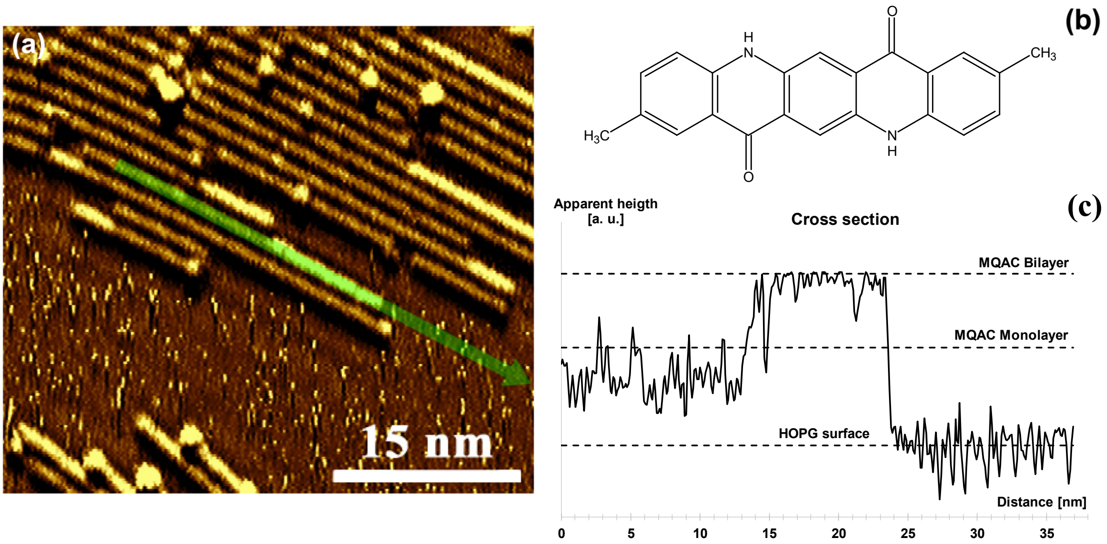

Figure S6. (a) STM picture of methylated quinacridone (MQAC) adsorbate structures. MQAC has almost the same chemical structure as QAC, but exhibits two additional methyl groups that support the formation of bilayer structures via steric interactions,[2] making thus the location and analysis of such bilayer structures much easier as compared to QAC bilayer structures. The linear features within the picture represent 1D MQAC chains that are built in the same way as supramolecular QAC chains are formed.[2] The significantly brighter sections atop of these linear features indicate plane-parallel bilayer structures, built as a supramolecular MQAC chain is formed directly on top of another one. (b) Chemical structure of MQAC. (c) Cross section of a plane-parallel MQAC bilayer, taken in the area marked with a green arrow in (a). Note that the apparent height is declared in arbitrary units, since the apparent height determined via STM depends on the STM scan settings, making accurate topographical measurements hardly possible.

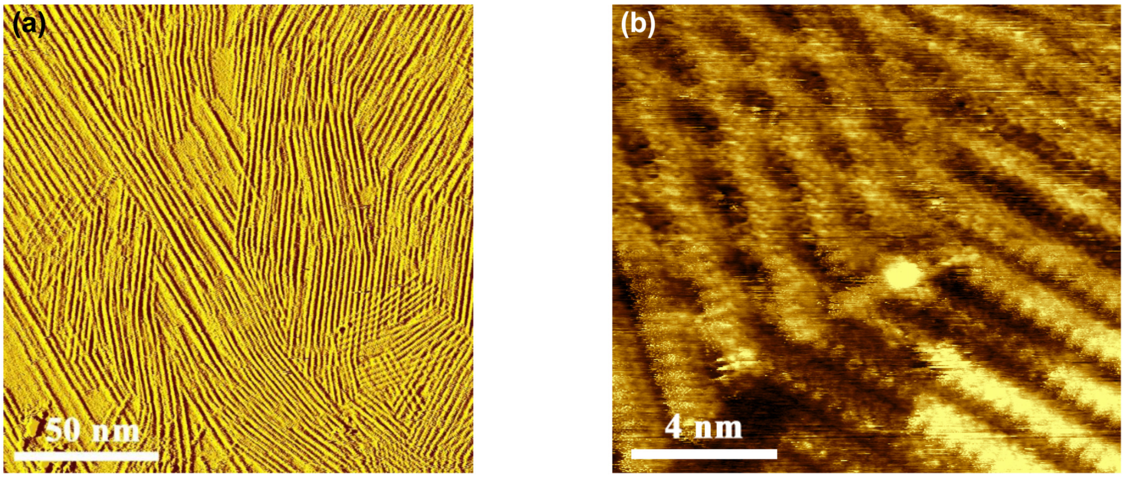

Figure S7. (a) STM picture of supramolecular QAC adsorbates atop a HOPG substrate. Two overlapping QAC arrays forming a bilayer exhibiting a crisscross structure can e.g. be seen in the bottom right corner. Note that it is hard to find QAC bilayer structures, making a detailed analysis challenging.[1] (b) Close-up view of QAC bilayer with a crisscross structure.

4. STM measurement artifacts

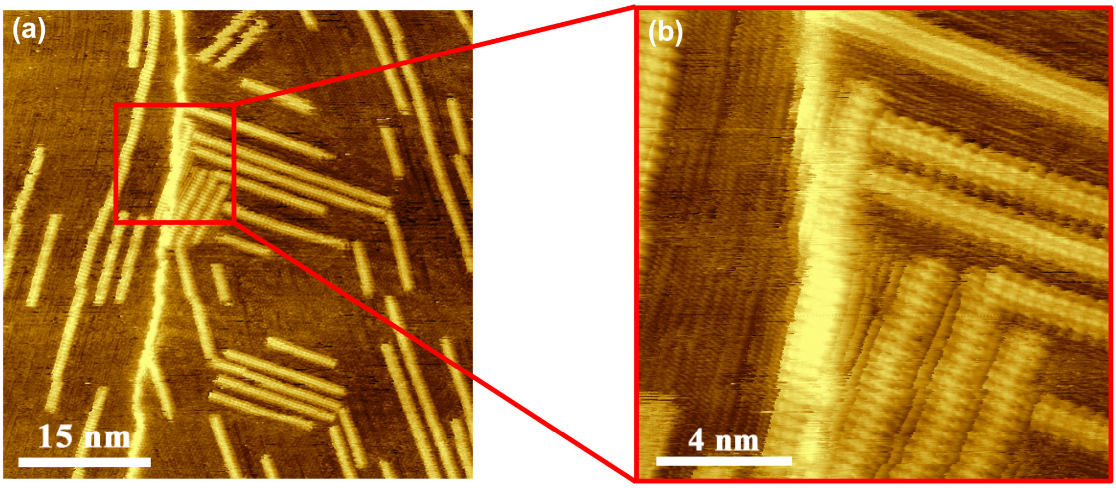

Figure S8. (a) STM picture of supramolecular QAC adsorbates on a HOPG. Additionally, chain-like structures can be seen next to the QAC structures, however, these structures are neither related to surface adsorbates nor to the substrate surface, but are related to measurement artefacts, them being the result of a poor quality of the STM tip and the ambient measurement conditions. Such measurement artefacts can be determined easily, since their size does not scale correctly: an increase in the magnification factor does not increase the size of these structures, as can be seen in (b). Further, related experiments have shown that these structures cannot be removed mechanically (by lowering the tip – substrate – distance), in contrast to actual adsorbates (like QAC molecules).

5. Determining the surface coverage

To determine the coverage of the HOPG surface by the QAC arrays within a single STM picture, the software Gwyddion (64bit), version 2.42 was used. For this, initially, the supramolecular QAC adsorbates (i.e. 1D chains and 2D arrays) via the tool “Mask Editor” were highlighted, followed by the export of single array dimensions by the tool “Grain distributions”, finally accompanied by the Microsoft Excel 2013 calculations to determine the coverage ratio. Further, to investigate the average coverage of a STM sample, we analyzed per sample an area of about 0.7 µm², using a number of STM pictures with high scan resolution and without measurement artefacts, randomly selected from at least 5 clearly separated positions of the covered substrate; the average coverage rates including the double standard deviations being specified in the current publication. Calculations revealed high doubled standard deviations, indicating the dependence of the coverage by QAC arrays on different positions of a STM sample. Nevertheless, the average coverage rates of different samples treated with different dispersing agents were observed to differ significantly higher in value.

6. Correlating physical properties of the dispersing agents to the surface coverage

Referring to the article text, an analysis was performed to reveal a potential correlation between specific physical parameters of the dispersing agents in use and the achieved surface coverage. Going into detail, contribution of the viscosity to the OSWD process was expected, since the viscosity appeared to influence the mobility of the dispersed QAC crystals, and hence their ability to contact the HOPG surface (Figure S9). Further, a correlation between the dispersing agents' relative permittivity, indicating the dispersing agents' polarity, and the final surface coverage with QAC arrays was expected, since the polarity probably modifies the gradient of the surface free energy (Figure S10). Additional analysis was performed, since during the sample preparation, it was eye-catching to see that the dispersing agents spanned a huge range of different surface tensions and vapor pressures. Whereas some dispersions formed stable drops, others were seen spreading over the whole HOPG surface, and the γQAC powder was found partially forming an independent phase, especially when water was used as the dispersing agent. Further, whereas some dispersing agents were seen evaporating at room temperatures within minutes, others required a significant longer time to do so. For the related results, refer to Figure S11 and Figure S12.

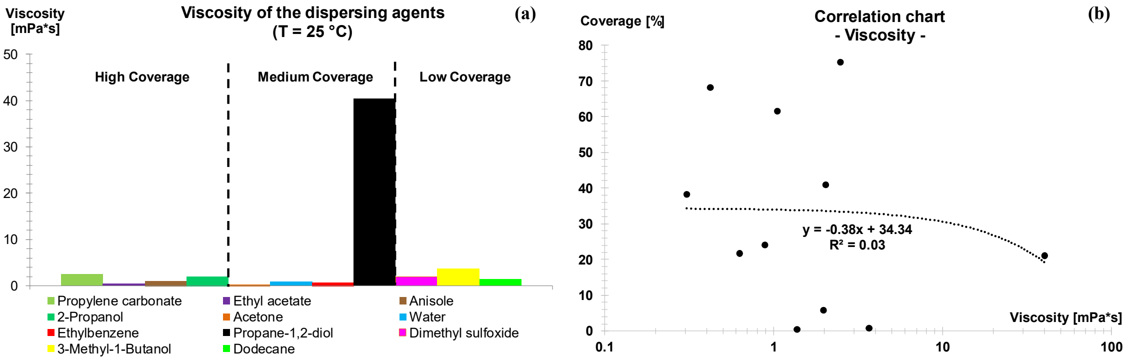

Figure S9. (a) The viscosity of the catalyzing dispersing agents in use,[8,9] classified according to the achieved surface coverage. (b) Scatter plot relating the median of the achieved surface coverage to the dispersing agent's viscosity. To avoid confusion, note that the nonlinear appearance of the regression line is related to the logarithmical scale of the x-axis.

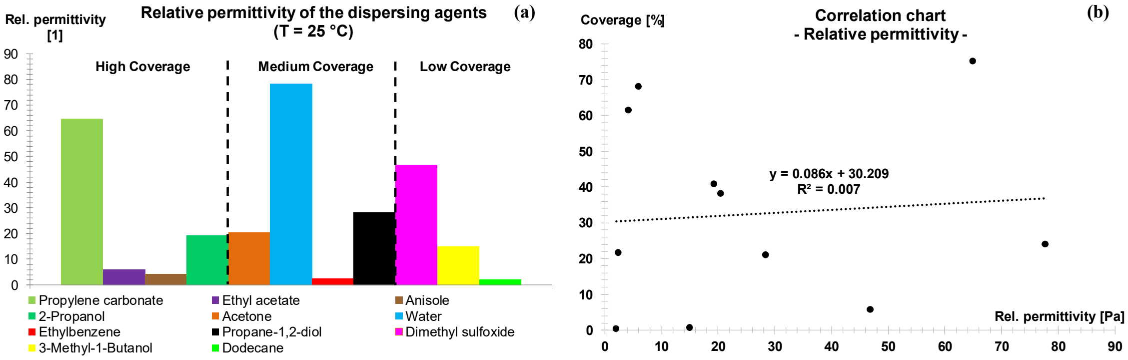

Figure S10. (a) The relative permittivity of the catalyzing dispersing agents in use,[9] classified according to the achieved surface coverage. (b) Scatter plot relating the median of the achieved surface coverage to the dispersing agent's relative permittivity.

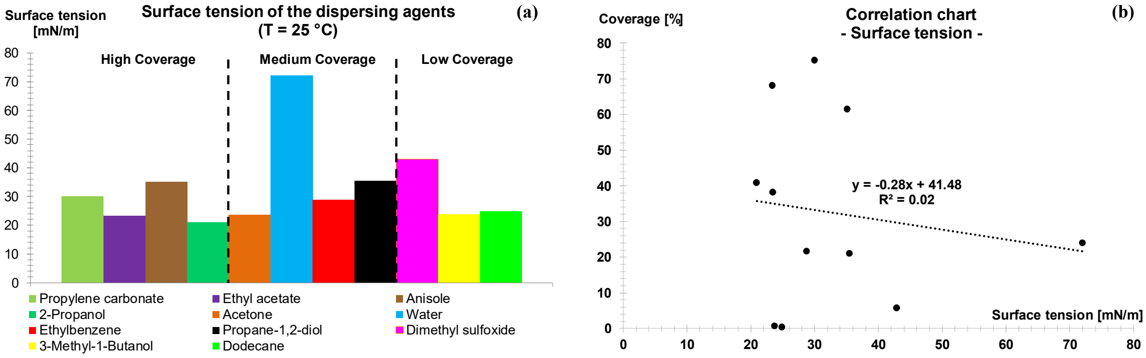

Figure S11. (a) The surface tension of the catalyzing dispersing agents in use,[9,10] classified according to the achieved surface coverage. (b) Scatter plot relating the median of the achieved surface coverage to the dispersing agent's surface tension.

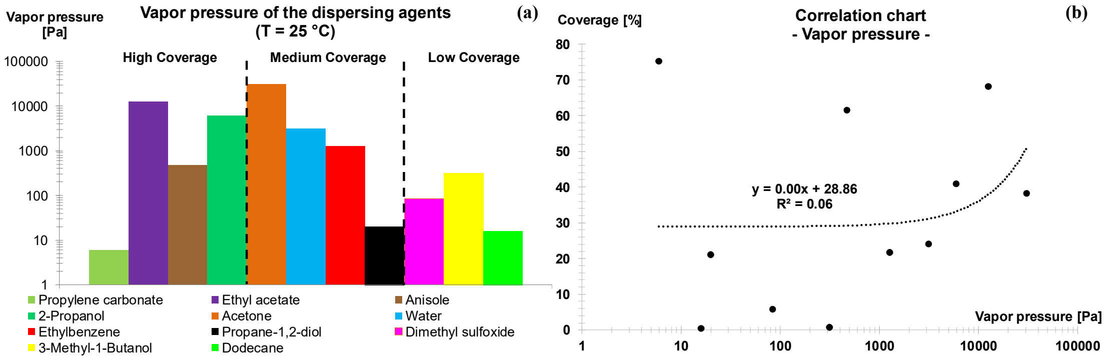

Figure S12. (a) The vapor pressure of the catalyzing dispersing agents in use,[9,11] classified according to the achieved surface coverage. (b) Scatter plot relating the median of the achieved surface coverage to the dispersing agent's vapor pressure. To avoid confusion, note that the nonlinear appearance of the regression line is related to the logarithmical scale of the x-axis.

7. Particle size measurements

For these measurements, we used a high-end dispersion analyzer, LUMiSizer 6112-95 from LUM. Further, for the analysis, 400 µl of sample, containing 0.5 wt. % pigment, and in some cases, additional of 0.125 wt. % salt, was used.

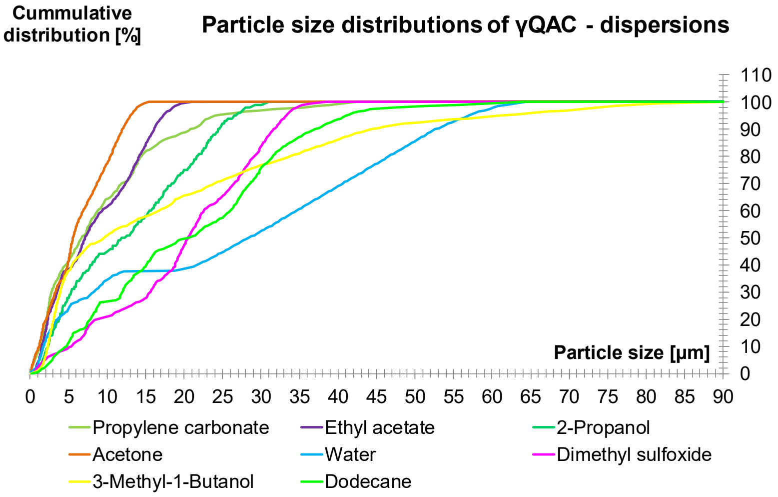

Figure S13. The cumulative distributions of the analyzed γQAC dispersions as a function of the particle size.

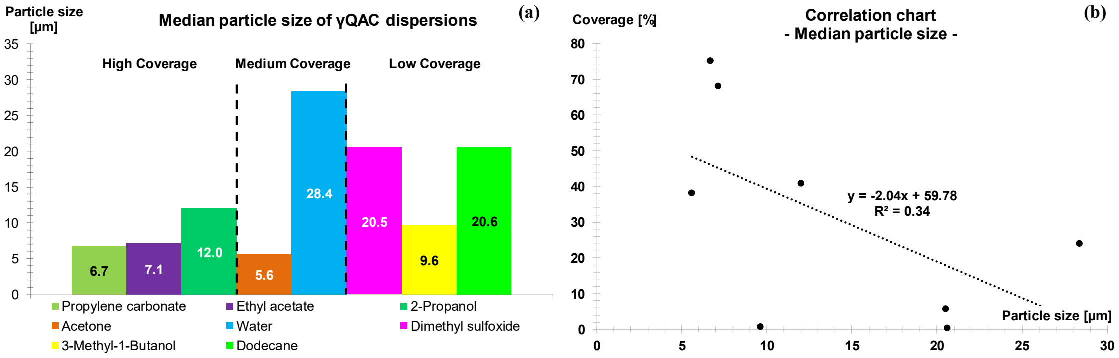

Figure S14. **(a)** Median particle size (equivalent diameter) of powdered γQAC, dispersed in different dispersing agents. **(b)** Scatter plot relating the median of the achieved surface coverage to the median of the particle size distribution.

8. Zeta potential measurements

All the zeta (ζ) potential measurements were performed using a Zetasizer Nano ZS ZEN 3600 system from Malvern; 4 ml samples with 0.1 wt. % of γQAC or graphite powder (from Alfa Aesar, item no. 14735) being used in this regard. Further, to determine the ζ potential distribution, three measuring cycles (each measuring cycle comprising of 30 single measurements) were performed per sample. The averaged results of a measuring cycle as a distribution of ζ potentials z_{mi} were displayed by the Zetasizer Nano ZS ZEN 3600, where z_{mi} represents the mean value of a ζ potential interval i, and the related intensities I_i (i.e. the total counts per ζ potential interval). This kind of representation corresponds to the type of display used for particle size distributions.[12] Further, the relative quantity $\Delta I(z_{mi})$ is determined via the total intensity I_{total}, as:

$$\Delta I(z_{mi}) = \frac{I_i}{I_{total}} \tag{1}$$

The sum of these relative values $\Delta I(z_{mi})$, starting with the most negative ζ potential z_{mmin} and going until z_{mi}, leads to the cumulative distribution $I(z_i)$, as:

$$I(z_i) = \sum_{z_{mmin}}^{z_{mi}} \Delta I(z_{mi}) \tag{2}$$

Worth noting here is that z_i is the upper value of the ζ potential interval i, due to plotting of the cumulative distribution against the upper interval value.[12] Further, Figure S15 shows the averaged cumulative distributions of the analyzed γQAC dispersions, derived by averaging 90 single ζ potential measurements per sample. Referring to the explanations in the article, both the z50 (the median value of the cumulative ζ potential distribution) and the z33 (the point where 33 % of the distribution is more negative and 66 % of the distribution is more positive) were derived from the corresponding cumulative distribution, employing linear interpolation, as:

$$zNN(I) = z_{i-1} + \frac{z_i - z_{i-1}}{I_i - I_{i-1}} (I - I_{i-1}) \tag{3}$$

Where zNN is the desired ζ potential, I the corresponding value of the cumulative distribution, the index i being related to the upper value of corresponding interval, and the index $i-1$ being related to the lower value of the corresponding interval. Note: the double standard deviation was employed to estimate the quality of the derived value. Further, as the distribution-measurements failed for the dispersing agents dodecane and 3-methyl-1-butanol, a monomodal measurement mode that determines only the median value had to be used. Though these monomodal measurements are just roughly comparable to the other measurements, they however indicated that the ζ potential of the γQAC crystals in dodecane and in 3-methyl-1-butanol is reverse to the ζ potentials in the other dispersing agents.

A comparison of the median values of the distributions (z50) indicated that the samples with a high z50 have a tendency of generating a high surface coverage, as can be seen in the Figure S16, however, the determined coefficient of determination $R^2 = 38$ % yielded no significant correlation to the surface coverage in this respect (in contrast to the z33 value, being discussed in the article text).

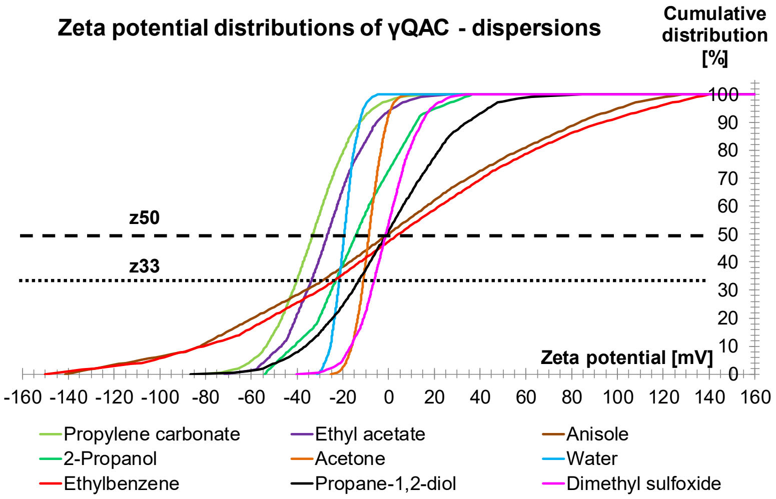

Figure S15. The cumulative distributions of the analyzed γQAC dispersions as a function of the ζ potential. The intersection of a sample's cumulative distribution and the dashed line yields the median value z50, while the intersection with the dotted line yields the z33.

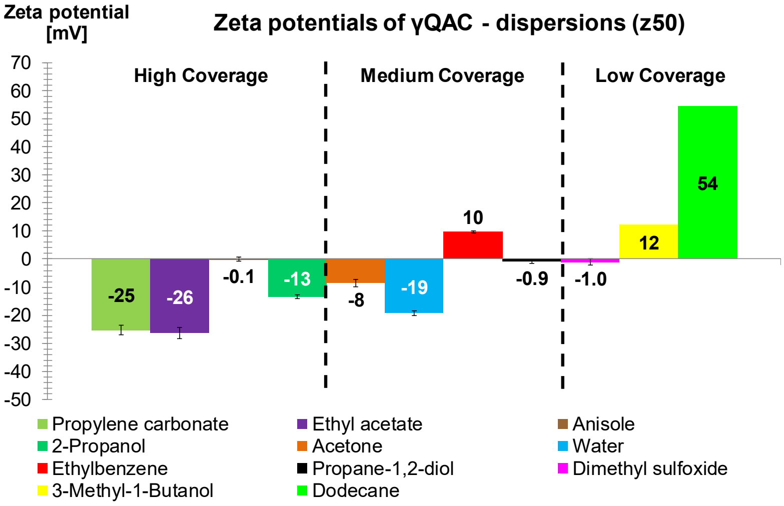

Figure S16. Comparison of the median values (z50) of the ζ potential distributions of γQAC dispersions with varying dispersing agents. The error bars indicate twice the standard deviation.

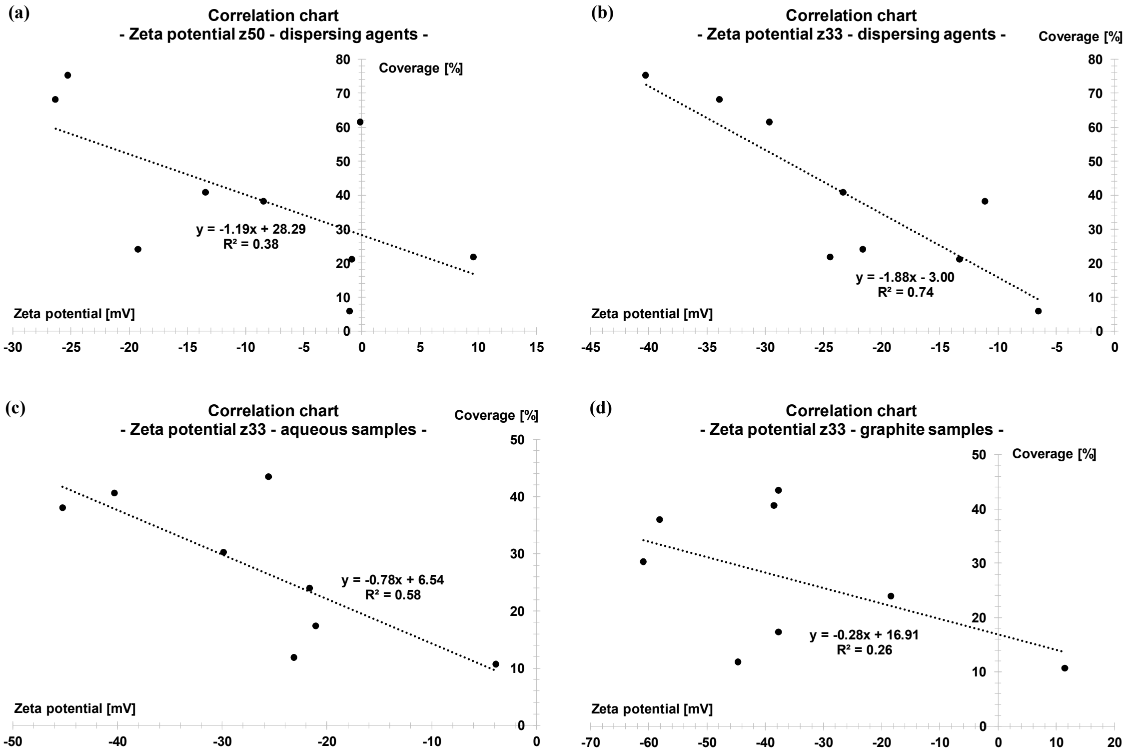

Figure S17. Scatter plots relating the median of the surface coverage of samples prepared with different dispersing agents to (a) the median of the ζ potential distribution z50 and (b) the z33 value of the ζ potential distribution. Further, scatter plots relating the median of the achieved surface coverage to (c) the ζ potential z33 of aqueous γQAC dispersions (modified with different salts, KOH, or H_2SO_4) and (d) the ζ potential z33 of aqueous dispersions containing dispersed graphite particles (instead of γQAC).

9. The origin of the ζ potential in in aqueous, moderate polar, and non-polar systems.

The dispersing of any object in an aqueous system generates a surface charge and thereby a ζ potential, arising mainly due to the adsorption of ionic species from the liquid phase or by the dissociation of surface molecules.[19,26] The charging mechanism in leaky dielectrics accord with aqueous systems, since the dissociation of ionic compounds is possible.[26-30] However, the Bjerrum length, the distance between ions required for stable dissociation, is significantly higher for fully non-polar media than for aqueous or moderately polar liquids. Further, the occurrence of ionic species is unlikely for the fully non-polar media according to the thermodynamic principles.[26,29,31-33] However, as substantial ζ potentials have long been investigated in non-polar media, it calls for the presence of some other charging mechanism in such media.[26,29-35] A key role in this regards can be attributed to polar impurities, particularly water, that are adsorbed to particle surfaces enabling dissociation processes. Reverse micelles play another important role in this respect: whereas on one hand they help to screen the surface charges and polar adsorbate layers from their non-polar environment, on the other hand, these reverse micelles (and probably other structures) carry charges themselves, obtained via proton transfers, as a result of non-specific thermal interactions. Further, indications were found that the charging of particles that are dispersed in organic liquids is related to molecular charge transfers, being the result of donor-acceptor interactions.[28] The letter results were found by analysing a number of organic liquids, including leaky dielectrics and non-polar media.

10. pH measurements

pH measurements were conducted using the pH meter "Checker" from HANNA, allowing a measurement accuracy of ± 0.2 pH. The sample composition was similar to that of the STM samples: 4 ml sample containing 2 wt. % pigment, and if necessary, additional 0.5 wt. % of salt. Further, prior to each pH measurement, the pH meter was calibrated using either a neutral (7.01), an acidic (pH 4.01), or a basic (pH 10.01) buffer solution, as per the nature of the analyzed sample.

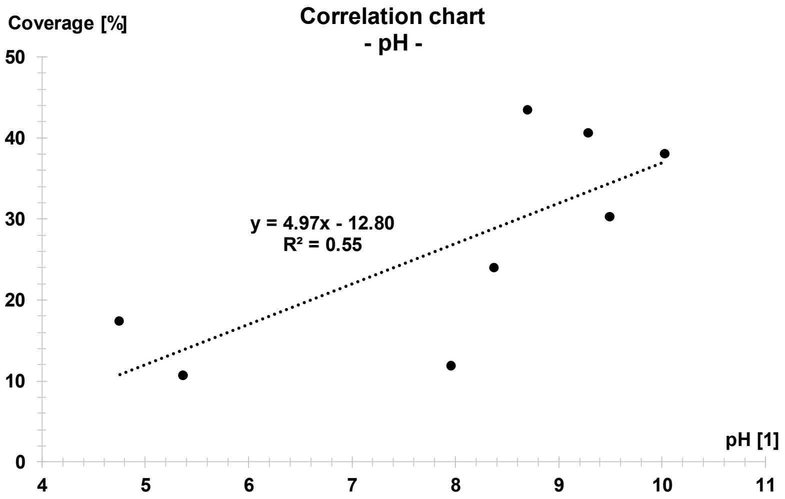

Figure S18. Scatter plot relating the median of the achieved surface coverage to the pH.

11. Scanning electron microscope measurements

The corresponding measurements have been performed using the scanning electron microscope 440i from Zeiss; the chief scan settings being as: working distance of either 3 or 5 mm and extra-high tension of 20.00 kV. Further, the SE1 detector was used for such measurements.

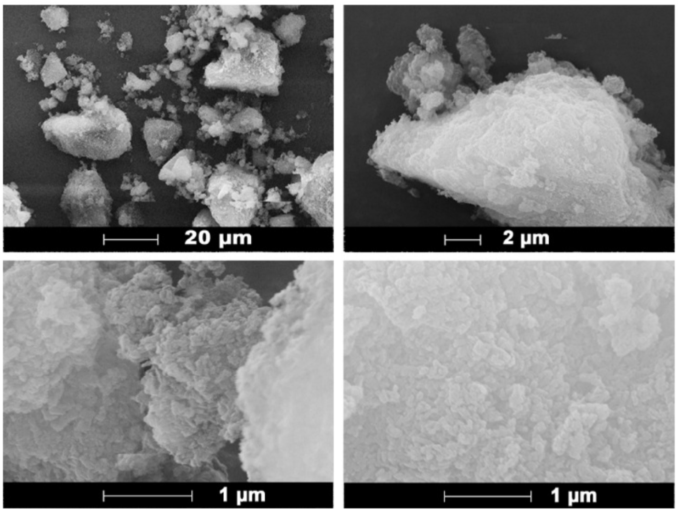

Figure S19. Scanning electron microscopy (SEM) pictures of γQAC crystals with increasing magnifications.

12. Force field calculations

Classical molecular mechanics calculations have been employed to determine both the binding energy of an organic semiconductor molecule (OSM) within a surface plane of a crystal (comprising of these OSMs) and the adsorption energy of an OSM on a graphite slab (0001). For analysis, three different force fields of the Accelrys' Materials Studio package have been applied, viz. the Dreiding force field, the Universal force field (UFF), and the Consistent Valence force field (CVFF).[13-15] To assign partial charges to the atoms of OSM's atoms, the Gasteiger method, for Dreiding and UFF, has been applied.[16] However, an explicit assignment of a partial charging method is not required for CVFF, since this force field already includes a charging method.[17-18]

Besides, the geometry optimization calculations (3D-periodic) of the crystals' unit cell have been performed according to the so-called "ultra-fine" setting, which corresponds to the convergence threshold values, as shown in the Table S1. However, for all the other calculations comprising larger systems (2D-periodic), due to the huge amount of molecules involved, the so-called "fine" setting has been applied (the terms "fine" and "ultra-fine" refer to settings within Accelrys' Materials Studio).

Table S1. Convergence threshold values

	Fine	**Ultra-fine**
Energy [kcal / mol]	$1 * 10^{-4}$	$2 * 10^{-5}$
Force [kcal / (mol Å)]	0.005	0.001
Stress [GPa]	0.005	0.001
Displacement [Å]	$5 * 10^{-5}$	$1 * 10^{-5}$

To determine the adsorption energy of an OSM on graphite, a 2D-periodic system was built with four graphene layers, with the bottom layer fixed. In a distance of 500 Å above these layers, an OSM was set. A geometry optimization calculation was performed to obtain the energy of the relaxed graphite layers plus the energy of an isolated OSM. Next, the OSM was moved on top of the graphite surface (distance about 3.5Å), and the geometry optimization was repeated to obtain the energy of the system where the OSM interacts with the graphite surface. The adsorption energy of the OSM on graphite could then be calculated from the difference between both the energy values.

The binding energy of an OSM located within the surface layer of an OSM crystal was calculated in a similar way. Calculations were performed for the three main crystal plains of the OSM crystal (refer Figure S20 for the crystal planes of γQAC). A small OSM crystal was built by repeating the unit cell of the OSM crystal in the three directions. Further, a 2D-periodic system was created containing the small OSM crystal (periodically repeated in two directions); the bottom crystal layer (of the non-periodic direction) being kept fixed. Depending on the γQAC crystal plane in use for the performed calculations, the nanocrystals were built by: for the crystal plane (100) by 6 x 6 x 3 γQAC unit cells, and for both the crystal planes (010) and (001) by 3 x 6 x 3 γQAC unit cells. Further, an initial geometry optimization calculation was performed to obtain a crystal with a relaxed surface. A second geometry optimization calculation was performed after one OSM of the surface layer had been moved away from the surface by a distance of 500 Å (refer Figure S21). The difference between both the energy values then led to the binding energy of an OSM within a surface layer.

Further, to roughly estimate the error within the binding/adsorption energy calculations, the energies were calculated once again with a system doubled in each of the direction. Such a calculation was performed only for one certain system, and one force field (QAC with Dreiding force field), owing to the long computing times (of several months) for such a largely extended system.

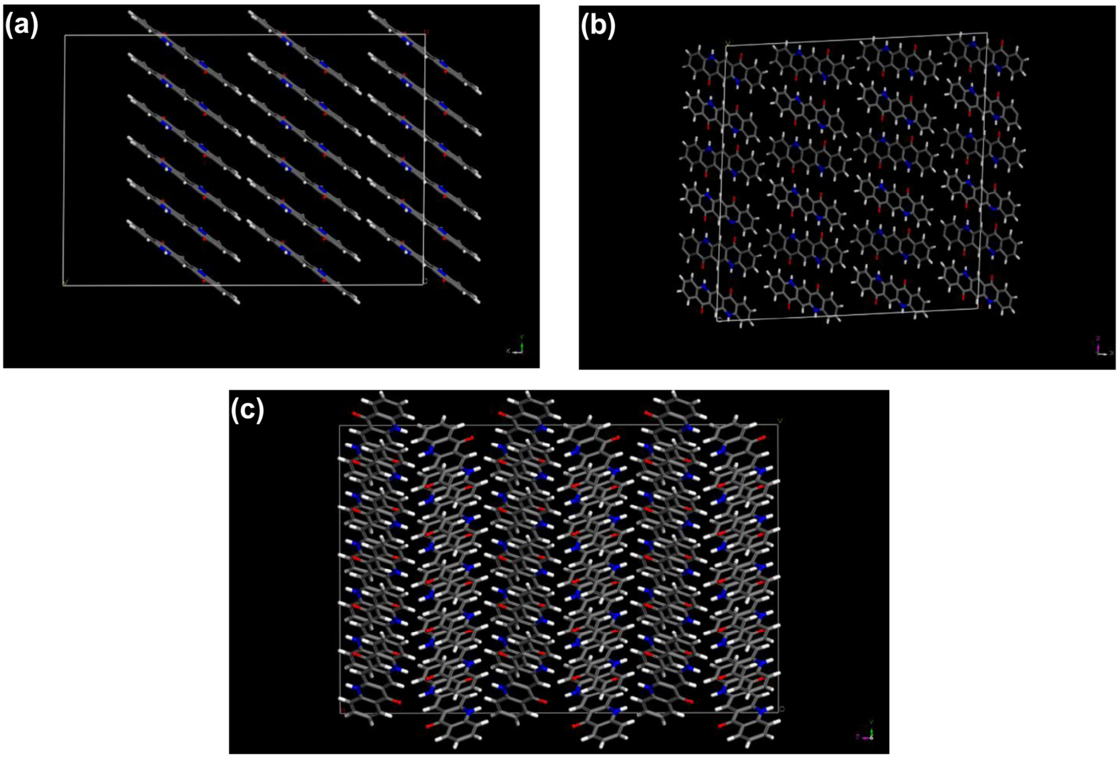

Figure S20. Example images depicting the crystal planes of a γQAC nanocrystal, with: (a) the crystal plane (001), (b) the crystal plane (010), and (c) the crystal plane (100).

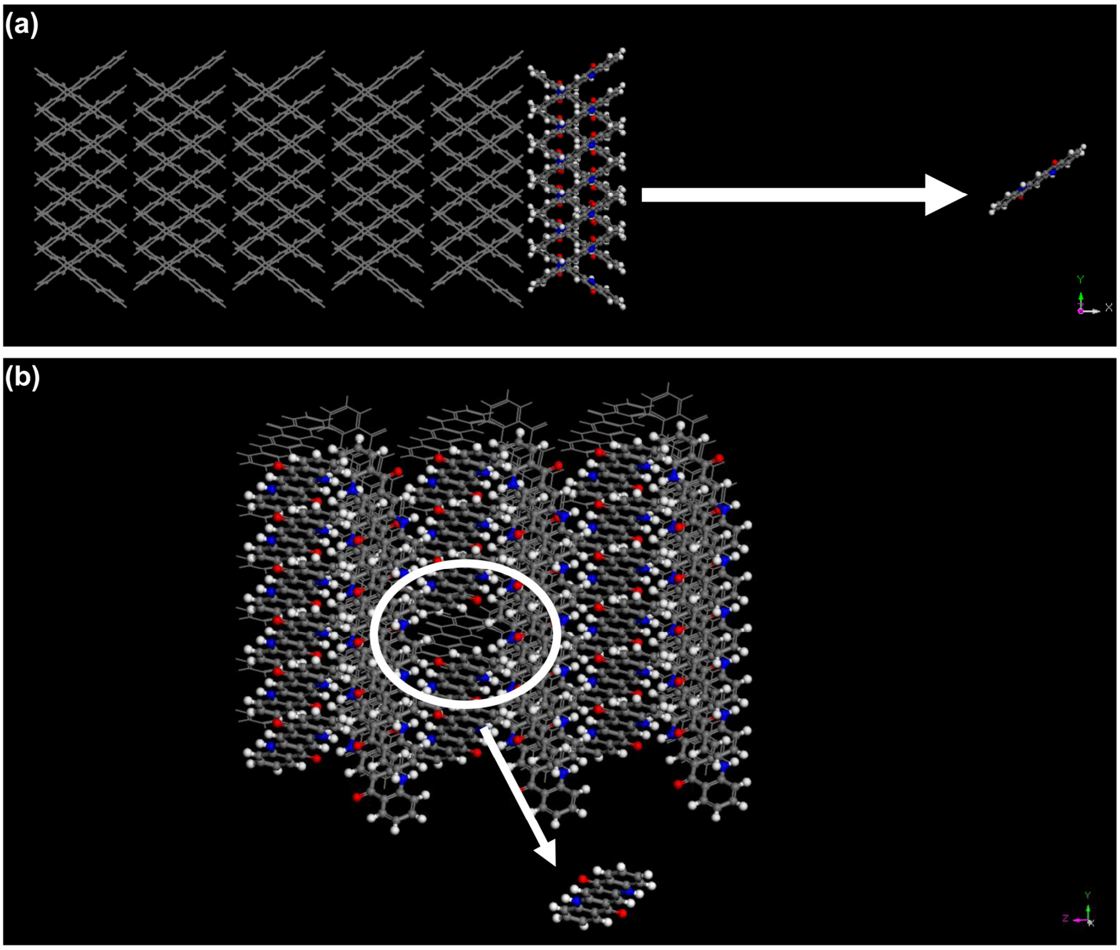

Figure S21. Example images depicting how one OSM is moved away from a (100) surface crystal plane of a nanocrystal, in order to determine its binding energy via force field calculations, with: (a) side view and (b) top view. Note: the distance between OSM and nanocrystal depicted in these example images is not true to scale, i.e. it is lower than the one used for the force field calculations (i.e. lower than 500 Å).

13. Back calculation determining the γQAC crystal dimensions and a suitable DLVO model

The question had to be assessed whether a γQAC crystal interacts as a whole with the substrate surface during the OSWD process, then for its shape being considered as a spherical shaped particle (Figure S19). However, powdered γQAC, as commercial semiconductors in general, does not comprise of mono-crystals, but agglomerated particles having very uneven resulting surfaces (Figure S19). Referring to the limited operating range of the π-π interactions, a γQAC agglomerate might therefore just partially interact with the HOPG surface, hence the interacting section, potentially, being considered as plate-like for such a case. To explore the above, the following approach was pursued: based on the number of QAC molecules, constituting well-defined, two-dimensional supramolecular arrays, the idea was to determine the dimensions of the source-crystals and compare them with the actual measured particle sizes.

The force field calculations discussed in the article text and the limited operating range of π-π interactions led to the assumption that a cohesive (010) crystal face delivers the QAC molecules to form a single cohesive, two-dimensional array, via the OSWD. Based on this assumption, a rough calculation to determine the equivalent diameter of a single γQAC crystal, having a (010) crystal face with the desired amount of QAC molecules, was performed. Since each unit cell of a γQAC crystal lattice contains 2 QAC molecules,[20] the quantity of QAC molecules N_M in the crystal face (010) can thus be given by the relation (using the variable n = {1; 2; 3; 4; …}:

$$N_M(n) = 2\,n^2 \tag{4}$$

Using the above equation, the volume of the unit cell V_{UC},[20] and the given quantity of QAC molecules N_M, the volume of the original γQAC crystal V_{QAC} can be related as:

$$V_{QAC} = \left(\frac{N_M}{2}\right)^{\frac{3}{2}} * V_{UC} \tag{5}$$

The equivalent diameter D_e of the γQAC crystal can hence be calculated by the formula:

$$D_e = 2 * \sqrt[3]{\frac{V_{QAC}}{\pi} * \frac{3}{4}} \tag{6}$$

Example values for these variables can be found in Table S2, showing exemplary the results of these back calculations.

In this regard, the number of the QAC molecules constituting an array was found to be in the range of 30 – 2655 molecules. Hence, the results of the related back calculations revealed that the equivalent diameters of the detaching γQAC crystals were in the range of 4 – 41 nm. Comparing these results with the measured values of 5.6 – 28.4 µm (Figure S14 (a)), it was hence deduced that just a tiny part of a γQAC crystal (approx. 0.3 – 1 ppm of its surface) interacts with the HOPG surface. Consequently, it was concluded that the interactions among the semiconductor crystal and the underlying substrate surface can be best described by the DLVO model for the plate-like interactions.[19]

Table S2. Example values of the variables used in the performed back calulations

n [1][a]	$N_M(n)$ [1][b]	V_{QAC} [nm³][c]	D_e [nm][d]
4	32	44	4
10	200	691	11
15	450	2334	16
20	800	5532	22
25	1250	10804	27
30	1800	18669	33
34	2312	27177	37
37	2738	35024	41

[a]The variable n. [b]The dedicated quantity of QAC molecules within the crystal face (010) N_M. [c]The volume of the related γQAC crystal V_{QAC}. [d]The thus calculated equivalent diameter D_e of the γQAC crystal.

14. Traditional DLVO simulations – relevant equations

The potential energy of interaction $\mathrm{V_T(h)}$ as a function of the separation h between the HOPG and the γQAC surface was determined as per the DLVO theory for parallel plates,[19] as:

$$V_T(h) = \left(-\frac{H_{123}}{12\,\pi} * \frac{1}{h^2}\right) + \left(\frac{64\,c_{i0}\,k\,T\,\Gamma_1\,\Gamma_3\,e^{(-\kappa h)}}{\kappa} * \frac{1000\,N_{Av}}{1}\right) \tag{7}$$

Where H_{123} is the Hamaker constant for the system: HOPG (index 1), dispersing agent (index 2), and the γQAC (index 3), given as:

$$H_{123} = \left(\sqrt{H_{11}} - \sqrt{H_{22}}\right) * \left(\sqrt{H_{33}} - \sqrt{H_{22}}\right) \tag{8}$$

Further, the Hamaker constant H_{ii} for the individual phases can be written as:

$$H_{ii} = \left(\frac{\rho\,N_{Av}\,\pi}{M}\right)^2 * \frac{3}{4} * \frac{\alpha^2\,\hbar\nu}{(4\,\pi\,\varepsilon_0)^2} \tag{9}$$

The polarizability α in the above equation, being determined via the Clausius-Mosotti relation,[21] as:

$$\alpha = \left(\frac{\varepsilon_r - 1}{\varepsilon_r + 2}\right) * \frac{M}{\rho} * \frac{3\,\varepsilon_0}{N_A} \tag{10}$$

The reverse Debye screening length κ was calculated by the relation (ε_r refers here to the dispersing agent):

$$\kappa = \sqrt{\frac{1000\,e_0^2\,N_{Av}\,\sum z_i^2\,c_{i0}}{\varepsilon_r\,\varepsilon_0\,k\,T}} \tag{11}$$

And the Goy-Chapman coefficients Γ_i calculated by:

$$\Gamma_i = \frac{|z_i|\,e_0\,\Phi_i}{4\,k\,T} \tag{12}$$

The constants used in these equations being: the molar electrolyte concentration c_{i0}, the Boltzmann's constant k, the temperature T (293,15 K), the Avogadro's number N_{Av}, the density ρ, the molar mass M, the ionization energy $\hbar\nu$,[23-25] the vacuum permittivity ε_0, the relative permittivity ε_r, the valence including the sign z_i, the electronic charge e_0, and the surface potential (the ζ potential) Φ_i.

15.Traditional DLVO simulations – results

In the course of the presented study, additional simulations were performed utilizing the traditional DLVO theory. The appropriate results are described below. To start with, calculations were done using all the positively charged ions present within the different aqueous systems: H_3O^+ being always present, the phosphate salts and sodium chloride delivering Na^+, KOH delivering K^+. The results of these calculations being demonstrated in the Figure S22; as can be seen, the single interaction energy functions exhibit strongly varying trends in the positive range, specifying the repulsive energy barrier (Figure S22, (a)). A comparison of the energy barrier maxima (Figure S22, (b)) reveals a trend towards aqueous systems catalyzing a high substrate surface coverage to exhibit a distinct repulsive energy barrier, whereas the systems water + sodium chloride, water + disodium pyrophosphate, and water + H_2SO_4 do not feature any repulsive energy barrier. However, such result being not conclusive, since a distinct repulsive energy barrier prevents a physical contact between substrate and dispersed semiconductor crystal, what was found to be a basic requirement for both the OSWD and the solid-solid wetting effects in general.[36-40]

Referring to the explanations in the main article, further DLVO calculations were performed by solely considering the concentration of the H_3O^+ - ions, taken from the previously measured pH values. Results revealed a distinctly lesser level and a flattened trend of the interaction energy functions (Figure S23, (a)), with only the sample modified with disodium phosphate displaying a narrow and tall repulsive energy peak. Further, the comparison of the energy barrier maxima yielded the water + H_2SO_4 sample to not feature any repulsive energy barrier and such result being still not conclusive (Figure S23, (b)).

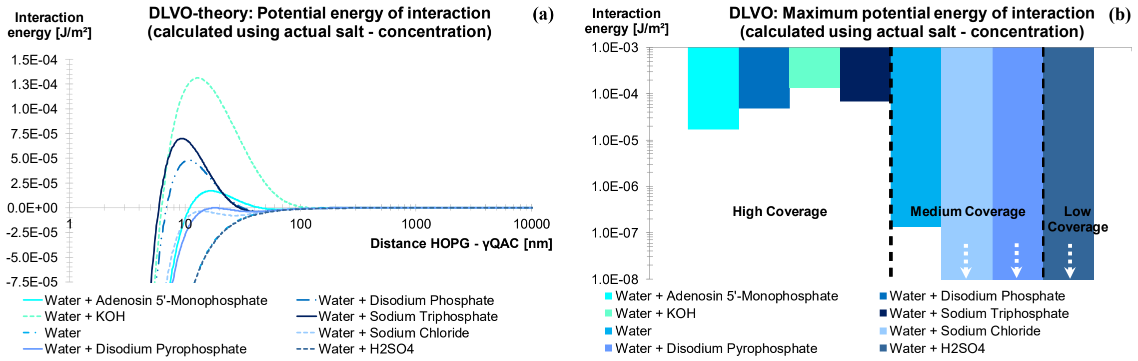

Figure S22. Simulation of the potential energy of interaction for the aqueous systems. (a) The complete interaction energy functions. (b) Comparison of the interaction energy maxima. Note: the samples water + sodium chloride, water + disodium pyrophosphate, and water + H_2SO_4 do not feature a repulsive energy barrier.

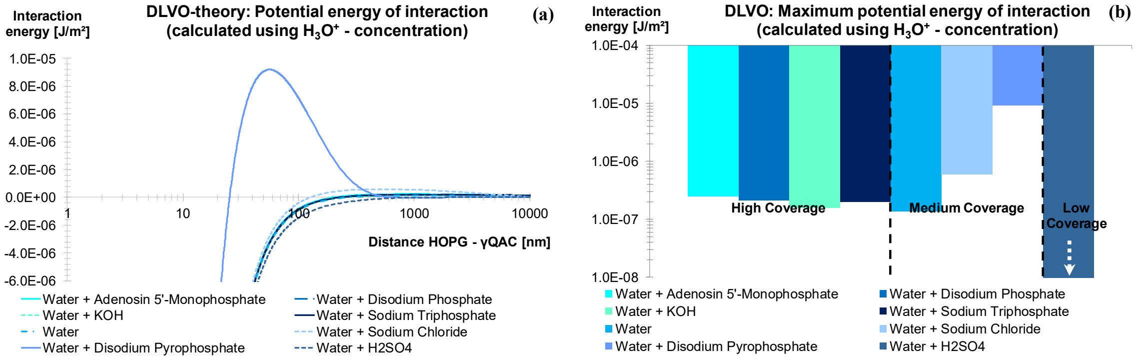

Figure S23. DLVO simulations by using solely the concentration of H_3O^+ - ions to determine the repulsive double layer forces. (a) The complete interaction energy functions. (b) Comparison of the interaction energy maxima. Note, that the sample water + H_2SO_4 does not feature a repulsive energy barrier.

16. Refined DLVO simulations – relevant equations

As is described in the article, the traditional DLVO simulations performed during this study were adjusted, in accordance with the work of Lukatsky and Safran, so as to include all kinds of fluctuation-induces forces.[22] The calculations are valid for particle separations that are significantly smaller than the Goy-Chapman length, which is approx. 10 µm in our aqueous systems. This enhanced term for the calculation of the potential energy of interaction $\mathrm{V_{eT}}$ consists of three sub-parts: the attractive Van-der-Waals interaction (calculated again via the Hamaker theory V_H), a new term for the unscreened Poisson-Boltzmann repulsion V_{PB}, and an additional term for the fluctuation-induced forces V_{ff}, expressed as:

$$\mathrm{V_{eT}(h)} = V_H + V_{PB} + V_{ff} \tag{13}$$

$$V_H(h) = -\frac{H_{123}}{12\,\pi} * \frac{1}{h^2} \tag{14}$$

Note, that the originally determined interaction pressures Π_n by Lukatsky and Safran, were by us converted into the interaction energies V_n,[19] via the relation:

$$V_n(h) = -\int \Pi_n dh \tag{15}$$

As a result, the Poisson-Boltzmann repulsion V_{PB} and the fluctuation-induced forces V_{ff}, are related as:

$$V_{PB}(h) = -\frac{k\,T}{\pi\,\lambda\,l_B}\ln(h) \tag{16}$$

$$V_{ff} = \frac{7\,k\,T}{4\,\pi\,\lambda^2}\ln(h) \tag{17}$$

The Gouy-Chapman length λ is calculated by:

$$\lambda = \frac{1}{2\,\pi\,l_B\,\sigma_0} \tag{18}$$

The Bjerrum length l_B is calculated by (ε_r refers here and below to the dispersing agent):

$$l_B = \frac{e_0^2}{4\,\pi\,\varepsilon_r\,\varepsilon_0 k\,T} \tag{19}$$

The total surface charge number density σ_0 is calculated by: [19]

$$\sigma_0 = \frac{1}{2}\left(\frac{\varepsilon_r\,\varepsilon_0\,\kappa\,(\Phi_1 + \Phi_3)}{e_0}\right) \tag{20}$$

17. Refined DLVO simulations – calculations using the actual salt-concentration

Via the refined DLVO theory, additional simulations were performed using all the positively charged ions present within the different aqueous systems (Figure S24). Analyzing the calculated interaction energy functions, results revealed one significant repulsive energy barrier related to the sample water + KOH. As stated before, a distinct repulsive energy barrier would significantly limit the potential of triggering the OSWD, making the latter result not conclusive as it does not match the experimental results that were obtained in this regard.

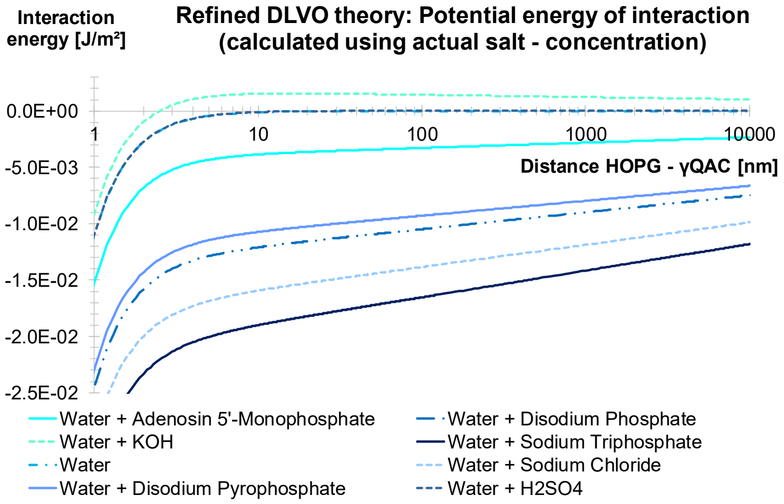

Figure S24. Interaction energy functions, determined via refined DLVO simulations using all the positively charged ions present within the different aqueous systems.

18. Refined DLVO simulations – determining factors and additional results

In order to further explore the nature of the refined DLVO theory and to evaluate the validity of the results presented so far, an attempt was also made to identify those factors that determine the refined DLVO theory. The following parameters remain constant when comparing the model systems investigated: the fundamental physical constants k, ε_0, e_0, N_{Av}, and π, as well as the material constants M, $\hbar\nu$, z_i, ρ, and ε_r. Thus, the molar electrolyte concentration c_{i0}, the ζ potential Φ_i and the temperature T were identified as potentially decisive influencing factors. According to the explanations in the main article text, it was found that the simulated hydrophobic surfaces adsorb exclusively hydroxyl ions within the applied salt concentrations.[41-43] Consequently, a logarithmic relationship of the form $\Phi_i = a \log c_{i0}$ results between the ζ potential of dispersed objects and the hydroxyl ion concentration within the corresponding dispersing agents.[43-45]

Based on this, a comparative study was conducted, performing refined DLVO simulations for the pH values 1 – 14, at T = 293.15 K (refer Figure S25). The corresponding ζ potentials were calculated using logarithmic regression functions determined from experimentally measured values (refer Figure S25 (c)). The results of the comparative study show that the repulsive energy barrier becomes smaller and smaller with increasing pH. This is in good agreement with the results of the model systems actually investigated and presented in the main article text.

In addition, a similar comparative study was carried out, this time however for T = 363.15 K, to analyze the influence of temperature on the refined DLVO simulations. The results are almost identical to the previous ones, with the only difference that the level of the repulsive energy barrier has generally decreased slightly (refer Figure S26). Thus, it can be deduced that the temperature has no significant influence on the DLVO calculations, in the temperature range relevant for the OSWD application. Please note that the temperature dependence of the constants ρ und ε_r of the dispersing agent was taken into account in the performed calculations.

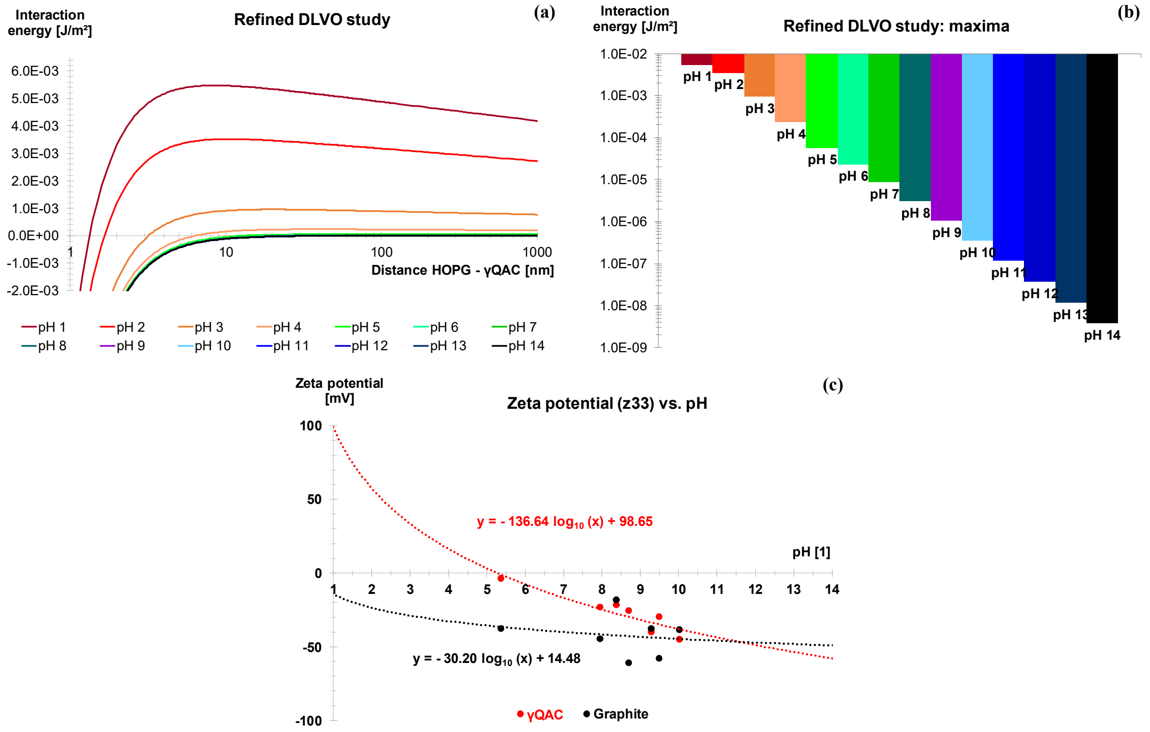

Figure S25. Results of a comparative study, performing refined DLVO simulations for different pH values, at T = 293.15 K. The corresponding ζ potentials were extrapolated using logarithmic regression functions (refer (c)). (a) The complete interaction energy functions. (b) Diagram showing the calculated DLVO maxima, whereby the DLVO maximum decreasing with increasing pH value. (c) The experimentally determined ζ potentials of γQAC and graphite particles at different pH values and the logarithmic regression functions based thereon.

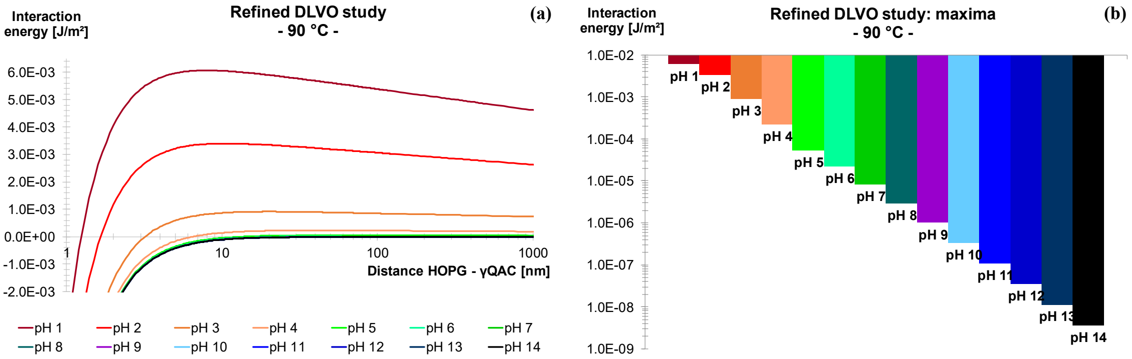

Figure S26. Results of an additional comparative refined DLVO study, this time performed for T = 363.15 K (corresponding to 90 °C). (a) The complete interaction energy functions and (b) the related DLVO maxima.

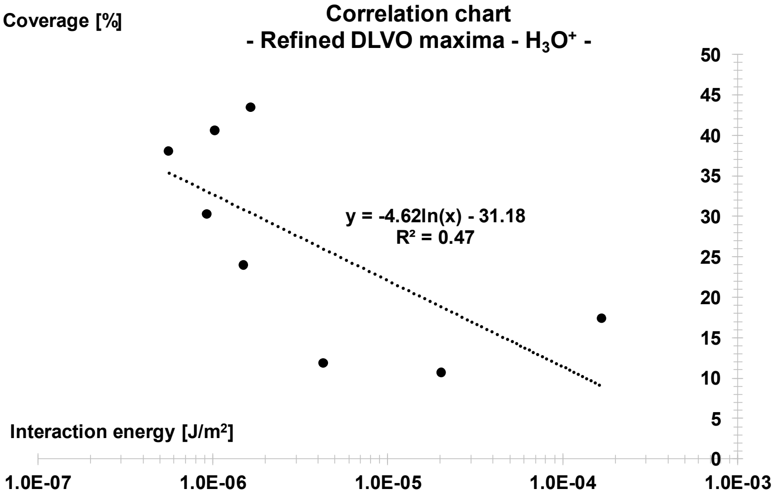

Figure S27. Scatter plot relating the median of the achieved surface coverage to the repulsive energy barrier, determined via refined DLVO calculations (considering solely the concentration of H_3O^+ ions).

REFERENCES

(1) Eberle, A.; Nosek, A.; Büttner, J.; Markert, T.; Trixler, F. *CrystEngComm* **2017**, *19*, 1417.

(2) Eberle, A.; Greiner, A.; Ivleva, N. P.; Arumugam, B.; Niessner, R.; Trixler, F. *Carbon* **2017**, *125*, 84-92.

(3) Hong, Y. A.; Hahn, J. R.; Kang, H. *J. Chem. Phys.* **1998**, *108*, 4367.

(4) Nagy, G. *J. Electroanal. Chem.* **1996**, *409*, 19–23.

(5) Nagy, G. *Electrochim. Acta* **1995**, *40*, 1417–1420.

(6) Räder, H. J.; Rouhanipour, A.; Talarico, A. M.; Palermo, V.; Samorì, P.; Müllen, K. *Nat. Mater.* **2006**, *5*, 276–280.

(7) Cousty, J.; Pham Van, L. *Phys. Chem. Chem. Phys.* **2002**, *5*, 599–603.

(8) Pal, A.; Dass, G.; Kumar, A. *J. Chem. Eng. Data* **1998**, *44*, 2–5.

(9) Lide, D. R. *CRC Handbook of Chemistry and Physics;* CRC Press: Boca Raton, Internet Version 2005; pp. 995, 999, 1136-1163, 1189-1193, 2422-2429.

(10) ChemSpider, *http://www.chemspider.com/Chemical-Structure.7636.html*, (accessed February 2016).

(11) PubChem, https://pubchem.ncbi.nlm.nih.gov/compound/7924#section=Top, (accessed November 2017).

(12) Hess, W. F. *Chem. Eng. Technol.* **2004**, *27* (6), 624.

(13) Mayo, S.L.; Olafson, B.D.; Goddard, W.A.I. *J. Phys. Chem.* **1990**, *101*, 8897–8909.

(14) Rappe, A. K.; Casewit, C. J.; Colwell, K. S.; Goddard, W. A.; Skiff, W. M. *J. Am. Chem. Soc.* **1992**, *114* (25), 10024.

(15) Dauber-Osguthorpe, P.; Roberts, V. A.; Osguthorpe, D. J.; Wolff, J.; Genest, M.; Hagler, A. T. *Proteins Struct. Funct. Genet.* **1988**, *4* (1), 31.

(16) Gasteiger, J.; Marsili, M. *Tetrahedron* **1980**, *36* (22), 3219.

(17) Hagler, A. T.; Lifson, S.; Dauber, P. *J. Am. Chem. Soc.* **1979**, *101* (18), 5122.

(18) Hagler, A. T.; Dauber, P.; Lifson, S. *J. Am. Chem. Soc.* **1979**, *101* (18), 5131.

(19) Stokes, R. J.; Evans, D. F. *Fundamentals of Interfacial Engineering*, Wiley-VHC, Weinheim, **1997**, pp. 34-41, 121-163.

(20) Panina, N.; Leusen, F. J. J.; Janssen, F. F. B. J.; Verwer, P.; Meekes, H.; Vlieg, E.; Deroover, G. *J. Appl. Crystallogr.* **2007**, *40*, 105–114.

(21) Wedler, G.; Freund H. J. *Lehrbuch der Physikalischen Chemie*; Wiley-VHC: Weinheim, 2012; pp 617.

(22) Lukatsky, D. B.; Safran, S. A. *Phys. Rev. E* **1999**, *60*, 5848–5857.

(23) Slattery, D. *Dye. Pigment.* **2001**, *49*, 21–27.

(24) Bohme, D. K. *Chem. Rev.* **1992**, *92*, 1487–1508.

(25) Bruggeman, P.; Schram, D.; González, M. A.; Rego, R.; Kong, M. G.; Leys, C. *Plasma Sources Sci. Technol.* **2009**, *18*, 25017–13.

(26) Berg, J. C. *An Introduction to Interfaces and Colloids*, World Scientific, Singapore, **2010**, pp. 455-466, 540-582.

(27) Labib, M. E.; Williams, R. *Colloid Polym. Sci.*, **1986**, 264, 533–541.

(28) Labib, M. E.; Williams, R. *J. Colloid Interface Sci.*, **1984**, 97, 356–366.

(29) Fu, R.; Prieve, D. C. *Langmuir*, **2007**, 23, 8048–8052.

(30) Mysko, D.; Berg, J. C. *Ind. Eng. Chem. Res.*, **1993**, 32 (5), 854–858.

(31) Mcnamee, C. E.; Tsujii, Y.; Matsumoto, M. *Langmuir*, **2004**, 1791–1798.

(32) Sainis, S. K.; Germain, V.; Mejean, C. O.; Dufresne, E. R. *Langmuir*, **2008**, 24, 1160–1164.

(33) Prieve, D. C.; Hoggard, J. D.; Fu, R.; Sides, P. J.; Bethea, R. *Langmuir*, **2008**, 24, 1120–1132.

(34) Hsu, M. F.; Dufresne, E. R.; Weitz, D. A. *Langmuir*, **2005**, *21*, 4881–4887.

(35) Briscoe, W. H.; Horn, R. G. *Langmuir*, **2002**, 18, 3945–3956.

(36) Trixler, F.; Markert, T.; Lackinger, M.; Jamitzky, F.; Heckl, W. *Chem. Eur. J.* **2007**, *13*, 7785-7790.

(37) Trixler, F.; Heckl, W.M. In *Modern Research and Educational Topics in Microscopy*; Méndez-Vilas, A., Diaz, J., Eds.; Formatex: Badajoz, 2007; Vol. 2, pp 534-541.

(38) Haber, J.; Machej, T.; Czeppe, T. *Surf. Sci.* **1985**, *151*, 301–310.

(39) Leyrer, J.; Margraf, R.; Taglauer, E.; Knözinger, H. *Surf. Sci.* **1988**, *201*, 603–623.

(40) Bertinchamps, F.; Grégoire, C.; Gaigneaux, E. M. *Appl. Catal. B Environ.* **2006**, *66*, 1–9.

(41) Vrbka, L.; Mucha, M.; Minofar, B.; Jungwirth, P.; Brown, E. C.; Tobias, D. J. *Curr. Opin. Colloid Interface Sci.* **2004**, *9*, 67-73.

(42) Tandon, V.; Kirby, B. J. *Electrophoresis* **2008**, *29*, 1102-1114.

(43) Tandon, V.; Bhagavatula, S. K.; Nelson, W. C.; Kirby, B. J. *Electrophoresis* **2008**, *29*, 1092-1101.

(44) Singh, Y.; Deshpande R. J.; Subramanian, S. *Proceedings of the International Seminar on Mineral Processing Technology*, Chennai, 2006.

(45) Chibowski, E. *J. Colloid Interface Sci.* **1979**, *69*, 326–329.

3. Summary and Outlook

3.1. The Physico-chemical Basis of the OSWD

3.1.1. Theoretical and Experimental Findings

The Organic Solid-Solid Wetting Deposition (OSWD) technique enables the assembly of 1D and 2D supramolecular architectures directly from the 3D organic source crystals, without their need of being dissolved, melted or undergoing evaporation. Summarizing the outcomes of the present dissertation, it can thus be said that the in-depth analysis of the OSWD model systems provided an insight into the fundamental physico-chemical basis of the OSWD technique. For working temperatures of up to (and at least) 160 °C, the OSWD could not be executed using the organic semiconductor in the form of a dry powder. However, at such moderate temperatures, the OSWD process could be triggered for the powdered organic semiconductor dispersed within a suitable dispersing agent and it's subsequent drop-casting onto the substrate surface. In this regard, it was revealed that low-cost organic and aqueous dispersing agents are suitable for triggering and directing the OSWD.

Findings further unveiled the outcome of the OSWD to be significantly dependent on the choice of the dispersing agent. Exploration of the OSWD model systems via *ceteris paribus* approaches disclosed the zeta potential of the dispersed crystals and further the pH of the aqueous OSWD model systems, to be the most influencing parameters affecting the technique's outcome. However, no significant correlation was found between the OSWD's performance and the physical parameters viscosity, permittivity, surface tension, and vapour pressure of the dispersing agent in use; the same being applicable for the particle size of the dispersed organic semiconductor crystals. Moreover, refined DLVO theory simulations to study the approach of a semiconductor crystal towards the substrate surface enabled the identification of the participating attractive and repulsive interactions at the fundamental level, along with an assessment of the related surface free energy's gradient. Finally, additional force field calculations further revealed the means via which the semiconductor crystals would geometrically interact with the substrate surface, during the OSWD process.

3.1.2. The Fundamental Model of the OSWD Process

A fundamental model of the OSWD process was proposed based on the deeper insight gained into it via the experimental and theoretical findings, the model being able to describe the importance of various forces at different crystal-surface distances (refer Figure 3.1). Briefly summarizing the model, semiconductor crystals that approach the substrate surface initially encounter a repulsive barrier at a distance of about 100 nm, the barrier having its origin in the electrical double layers that surround all objects in contact with the dispersing agent. As the level of the barrier decreases with an increasing negative zeta potential, the clearly negatively charged crystals become capable of overcoming it. Subsequently, the interplay of Poisson-Boltzman related, Van-der-Waals, and Casimir-like fluctuation-induced forces causes an increasing attraction towards the substrate surface.

At a distance of about 10 nm and below, the liquid-phase molecules and the weakly bonded ionic species get expelled by the hydrophobic dewetting effects, followed by the solvated ions constituting the outer Helmholtz planes of the involved surfaces [58,74]. The origin of such dewetting effects lie in the hydrophobicity of both the semiconductor crystals and the substrate surface, such effects being reported for aqueous, polar, and fully nonpolar dispersing agents [67-72]. The remaining, non-solvated, ionic adsorbates induce a steric barrier below a separation of 1 nm between the semiconductor crystals and the substrate surface. As far as the aqueous systems are concerned, the barrier comprises of ice-like structured water molecules and selectively adsorbed hydroxyl ions [75-77]. However, the sum of all the attractive forces, including the hydrophobic dewetting interaction, reaches such a level at this separation that the inner Helmholtz planes get as well expelled, thereby eliminating the steric barrier [67,72]. Consequently, a direct physical contact between a semiconductor crystal and the substrate surface is established.

This triggers the OSWD process, provided the binding energy of the molecules within the facing semiconductor crystal plane is lower as compared to that of the molecules adsorbed on the substrate surface, and that the attraction of semiconductor molecules towards the substrate surface is strengthened. Such strengthening in turn being attributed to the Poisson−Boltzmann related and fluctuation induced forces provided by the inner Helmholtz planes. Consequently, the gradient of the surface free energy is modified, thereby catalysing the detachment of the semiconductor molecules from the semiconductor crystal via the OSWD. In this respect, a comparative value was introduced, the zeta potential z33 (the point within a zeta potential distribution where 33 % of the distribution is more negative and 66 % is more positive), whereby the more negative the z33 value, higher being the generated substrate surface coverage. All this results in the attachment of the semiconductor molecules to the substrate surface via noncovalent bonding; the interaction being π–π stacking for graphitic substrates. Subsequently, the occurring self-assembly processes define the structure of the formed supramolecular array. It was found that the surface diffusion of the adsorbed semiconductor molecules is limited up to temperatures of 160 °C, thereby limiting the detachment of molecules from the semiconductor crystal to the outermost surface layer and thus, the ability to grow long-range ordered monolayers. This, as a result, leads in to a distinct and a defined domain structure by the generated surface coverage; the transfer and the assembly of the supramolecular arrays being completed within seconds or less.

Besides, a new sample preparation technique was developed, thermally triggering the OSWD without the need of applying a dispersing agent. To achieve the required gradient of the surface free energy and to supply the required activation energy, both the substrate and the powdered semiconductor atop were heated up to a temperature of 240 °C and beyond. It was found that at such temperatures, the accelerated and enhanced surface diffusion processes enabled the adsorbed semiconductor molecules to migrate more extensively across the substrate surface – apart from the thermal annealing effects that additionally occurred. Consequently, the thermally triggered OSWD leads to the formation of extended and well-ordered adsorbate layers.

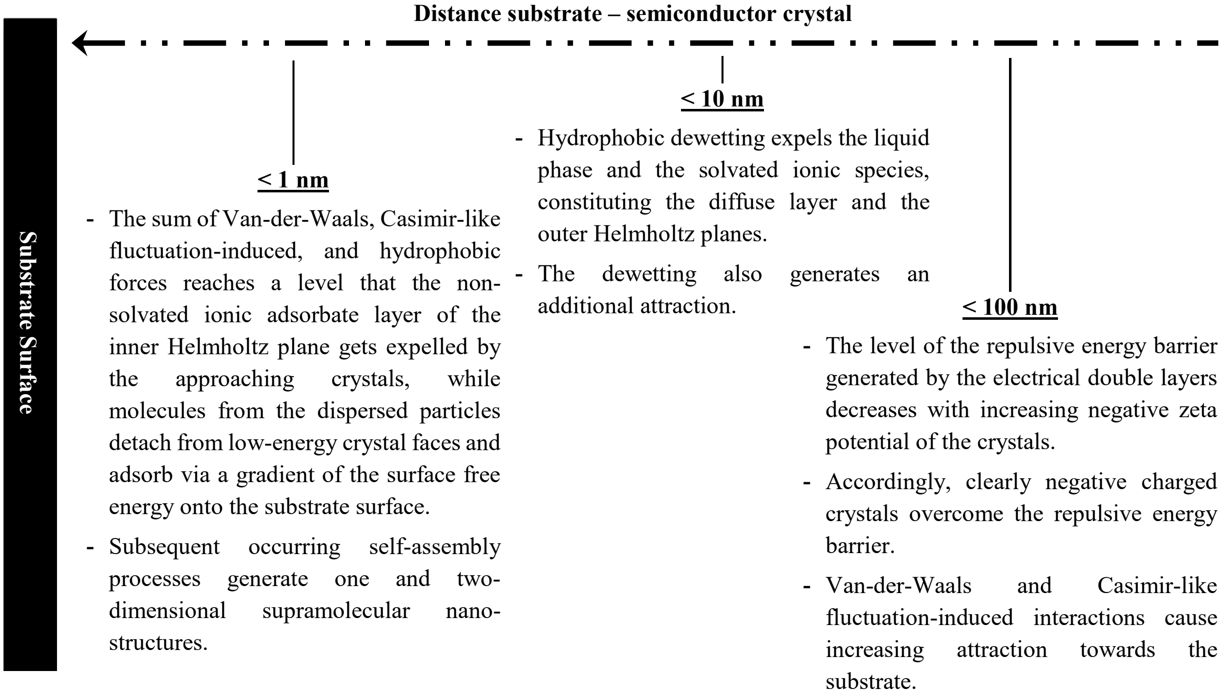

< 1 nm

- The sum of Van-der-Waals, Casimir-like fluctuation-induced, and hydrophobic forces reaches a level that the non-solvated ionic adsorbate layer of the inner Helmholtz plane gets expelled by the approaching crystals, while molecules from the dispersed particles detach from low-energy crystal faces and adsorb via a gradient of the surface free energy onto the substrate surface.
- Subsequent occurring self-assembly processes generate one and two-dimensional supramolecular nano-structures.

< 10 nm

- Hydrophobic dewetting expels the liquid phase and the solvated ionic species, constituting the diffuse layer and the outer Helmholtz planes.
- The dewetting also generates an additional attraction.

< 100 nm

- The level of the repulsive energy barrier generated by the electrical double layers decreases with increasing negative zeta potential of the crystals.
- Accordingly, clearly negative charged crystals overcome the repulsive energy barrier.
- Van-der-Waals and Casimir-like fluctuation-induced interactions cause increasing attraction towards the substrate.

Figure 3.1 Summary of the major processes that the dispersed semiconductor crystals undergo, as they approach the substrate surface. Reprinted with permission from the *J. Am. Chem. Soc.*, 2018, 140 (4), pp 1327–1336. Copyright © 2018 American Chemical Society. https://pubs.acs.org/doi/full/10.1021/jacs.7b10282

3.2. Novel Ways to Direct and Control the OSWD

An exploration of the possibilities to control the OSWD in detail revealed several novel approaches, as to direct the related supramolecular self-assembly at will. In this respect, the topmost proposition was by choosing (or preparing) an apt dispersing agent. It was found that the same type of semiconductor molecule was able to generate different supramolecular assemblies and that certain dispersing agents reproducibly favour the development of specific supramolecular assemblies. For instance, applying the dispersing agent ethylbenzene to the organic semiconductor gamma quinacridone (γQAC) leads to the formation of distinct 1D assemblies, instead of 2D domains. Thus, the generation of a particular assembly can be achieved by carefully choosing a specific dispersing agent, thereby particularly adjusting the zeta potential of the dispersed semiconductor crystals to an appropriate value. Moreover, it was found that the selection of the dispersing agent also considerably determines the degree of substrate surface coverage that can be achieved via OSWD. Hence, directing the OSWD at will via modifications of the zeta potential became straightforward for the aqueous dispersing systems – using phosphate salts, acid or base.

Additional approaches to control the OSWD driven assembly of surface adsorbates were revealed by developing new and enhanced sample preparation methods. For instance, gently rubbing the semiconductor crystals against the substrate in the presence of a catalysing dispersing agent significantly increases the achieved surface coverage. Besides, directional rubbing allows modification in the size and the orientation of the generated supramolecular arrays. Moreover, the newly developed, thermally triggered sample preparation approach enables the generation of extended and well-ordered monolayers (in contrast to the so far created substrate coverage exhibiting a distinctly defined domain structure), in a straightforward way. Beyond that, the high mechanical stability the surface adsorbates generated via the OSWD enables structural modifications on the nanoscale level, by means of tip-based scanning probe nanolithography [23].

3.3. Assessing the Potentials of the OSWD

To assess the potentials of the OSWD technology, particularly in the field of carbon-based (nano)electronics, in-depth investigations were performed using Raman spectroscopy and Scanning Tunneling Spectroscopy (STS). Respective results clearly made the chemical doping of graphene via OSWD evident, thereby revealing the applicability of the technique in the fabrication of carbon-based semiconductor devices. As the properties of a bandgap depend both on the chemical structure and the orientation of the doping surface adsorbate [73], and since the OSWD enables the modification of both the above factors, the technique further presents itself as a promising approach for the future bandgap engineering of graphene. Moreover, the OSWD provides reproducible results in terms of the structure and the coverage rate of the generated surface adsorbates, provided that the samples are prepared under identical conditions. Similarly, all the discovered possibilities to steer the OSWD process are not locally restricted and do not require an extensive sample post-processing. The presented rubbing technique is nevertheless a promising approach for a straightforwardly applicable reworking step that significantly increases the performance of the OSWD process. In summary, thus it can be said that the OSWD approach presents itself as a freely up-scalable methodology.

Additionally, the technique also allows for a wide range of applications in different processing technologies, owing to the fact that it can be triggered and controlled in several ways. Keeping in mind the varying requirements of dispersion-based processing techniques like the inkjet-printing, the drop-casting or the spin-coating, the OSWD enables the selection of a suitable dispersing agent solely based on the appropriate physical properties of the dispersing agent. The properties and conditions required to trigger the OSWD process (refer chapter ‘3.1.2 The Fundamental Model of the OSWD Process’) can be provided by addition of suitable additives to the dispersion, like the phosphate salts, acid or base, and/or by applying the presented reworking step. Besides, with respect to the durability of the generated surface adsorbates, the adsorbates generated via the OSWD were found to resist humidity and water, were thermally stable up to 300 °C at least, and were temporally stable for a minimum of 36 days. Earlier investigations moreover revealed the potential use of an alkyd resin, providing a resistant protection layer, without damaging the supramolecular structures [19]. Further, as water was identified as a suitable dispersing agent, OSWD made all kinds of non-toxic applications, as in a living organism or in the food industry, imaginable.

In conclusion, thus it can be said that the OSWD technique points towards an industrial application for the fabrication of low-cost, but large-scale products based on pigment-functionalized substrates, like graphene or carbon nanotubes (CNTs). For instance, a highly-promising prospect would be to apply the OSWD technique to the field of printed and flexible carbon-based electronics, as to perform the essential bandgap engineering. Flexible electronics combine the outstanding electric properties of graphene-based materials (high intrinsic carrier mobility, conductivity, and mechanical flexibility) with flexible and even transparent plastic-based substrates. The utilisation of printing technologies facilitates a customer-specific fabrication in practically freely scalable quantities and at very low production costs. The combination of both the technologies has already enabled the development of both advanced and entirely new types of electronic devices, such as active-matrix organic light-emitting diode (AMOLED) displays that are additionally sensitive to the strength of the applied pressure, for future generations of flexible displays, electronic papers and touch screens.

Further, flexible pressure and strain sensors now enable the real time monitoring of human motion or biological signals such as breathing and phonation. Besides, flexible light-emitting diodes (LEDs) and solar cells have been presented that can conform to non-flat surfaces, such as the exterior and interior structures of buildings and homes. Flexible and lightweight sensors based on chemically doped CNTs enable the detection of various chemical and biological species such as hydrogen (H_2), nitrogen dioxide (NO_2), ammonia (NH_3), carbon monoxide (CO), dimethyl methylphosphonate (DMMP), 2,4,6-trinitrotoluene (TNT), ethanol, glucose, and dopamine, with a detection limit of several ppm. Such sensors were found to be flexible and lightweight enough to be placed on biological surfaces, the human body, textiles or to be used in aerospace applications (refer [9] for the whole section). Summing-up it can be hence said that for the OSWD technique, numerous possible applications already exist, especially when it comes to the area of printed and flexible carbon-based electronics.

Bibliography

[1] Thompson, S. and Parthasarathy, S. (2006): Moore's law: the future of Si microelectronics, *Materials Today*, 9 (6), pp. 20–25. doi: 10.1016/S1369-7021(06)71539-5.

[2] Avouris, P., Chen, Z. and Perebeinos, V. (2007): Carbon-based electronics, *Nature nanotechnology*, 2 (10), pp. 605–15. doi: 10.1038/nnano.2007.300.

[3] Lu, W. and Lieber, C. M. (2007): Nanoelectronics from the bottom up., *Nature materials*, 6 (11), pp. 841–50. doi: 10.1038/nmat2028.

[4] Chen, H.-H., Su, S. H., Chang, S.-L., Cheng, B.-Y., Chen, S. W., Chen, H.-Y., Lin, M.-F. and Huang, J. C. a. (2015): Tailoring low-dimensional structures of bismuth on monolayer epitaxial graphene, *Scientific Reports*, 5, p. 11623. doi: 10.1038/srep11623.

[5] Tans, S., Verschueren, A. and Dekker, C. (1998): Room-temperature transistor based on a single carbon nanotube, *Nature*, 672 (1989), pp. 669–672. doi: 10.1038/29954.

[6] Medina, H., Lin, Y. C., Obergfell, D. and Chiu, P. W. (2011): Tuning of charge densities in graphene by molecule doping, *Advanced Functional Materials*, 21 (14), pp. 2687–2692. doi: 10.1002/adfm.201100401.

[7] Manna, A. K. and Pati, S. K. (2009): Tuning the electronic structure of graphene by molecular charge transfer: A computational study, *Chemistry - An Asian Journal*, 4 (6), pp. 855–860. doi: 10.1002/asia.200800486.

[8] Long, B., Manning, M., Burke, M., Szafranek, B. N., Visimberga, G., Thompson, D., Greer, J. C., Povey, I. M., MacHale, J., Lejosne, G., Neumaier, D. and Quinn, A. J. (2012): Non-covalent functionalization of graphene using self-assembly of alkane-amines, *Advanced Functional Materials*, 22 (4), pp. 717–725. doi: 10.1002/adfm.201101956.

[9] Park, S., Vosguerichian, M. and Bao, Z. (2013): A review of fabrication and applications of carbon nanotube film-based flexible electronics., *Nanoscale*, 5 (5), pp. 1727–52. doi: 10.1039/c3nr33560g.

[10] Liu, N., Zhou, Y., Ai, N., Luo, C., Peng, J., Wang, J., Pei, J. and Cao, Y. (2011): High-performance, all-solution-processed organic nanowire transistor arrays with inkjet-printing patterned electrodes, *Langmuir*, 27 (24), pp. 14710–14715. doi: 10.1021/la2033324.

[11] Liu, N., Zhou, Y., Wang, L., Peng, J., Wang, J., Pei, J. and Cao, Y. (2009): In situ Growing and patterning of aligned organic nanowire arrays via dip coating, *Langmuir*, 25 (2), pp. 665–671. doi: 10.1021/la8036633.

[12] Zheng, J. Y., Yan, Y., Wang, X., Zhao, Y. S., Huang, J. and Yao, J. (2012): Wire-on-wire growth of fluorescent organic heterojunctions, *Journal of the American Chemical Society*, 134 (6), pp. 2880–2883. doi: 10.1021/ja209815f.

[13] Yu, G. and Lieber, C. M. (2010): Assembly and integration of semiconductor nanowires for functional nanosystems, *Pure and Applied Chemistry*, 82 (12), pp. 2295–2314. doi: 10.1351/PAC-CON-10-07-06.

[14] Jordan, B. J., Ofir, Y., Patra, D., Caldwell, S. T., Kennedy, A., Joubanian, S., Rabani, G., Cooke, G. and Rotello, V. M. (2008): Controlled self-assembly of organic nanowires and

platelets using dipolar and hydrogen-bonding interactions, *Small*, 4 (11), pp. 2074–2078. doi: 10.1002/smll.200800811.

[15] Liu, M., Ji and Z., Shang, L. (2010): Top-Down Fabrication of Nanostructures, In *Nanotechnology, Vol. 8: Nanostructured Surfaces*, Chi, L., Ed., WILEY-VCH: Weinheim, pp. 17-35.

[16] Zhong, D., Zhang, H., Chi, L. (2010): Surface-Supported Nanostructures Directed by Atomic- and Molecular-Level Templates, In *Nanotechnology, Vol. 8: Nanostructured Surfaces*, Chi, L., Ed., WILEY-VCH: Weinheim, pp. 357-369.

[17] Kowarik, S., Gerlach, a and Schreiber, F. (2008): Organic molecular beam deposition: fundamentals, growth dynamics, and in situ studies, *Journal of Physics: Condensed Matter*, 20 (18), p. 184005. doi: 10.1088/0953-8984/20/18/184005.

[18] Treier, M., Orgiu, E., Zalewski, L., Cho, D., Rieger, R., Müllen, K. and Samorì, P. (2010): Solid–solid transfer of organic semiconductors for field-effect transistor fabrication, *Journal of Materials Chemistry*, 20 (41), p. 9018. doi: 10.1039/c0jm02173c.

[19] Trixler, F., Markert, T., Lackinger, M., Jamitzky, F. and Heckl, W. M. (2007): Supramolecular Self-Assembly Initiated by Solid–Solid Wetting, *Chemistry - A European Journal*, 13 (27), pp. 7785–7790. doi: 10.1002/chem.200700529.

[20] Eberle, A., Nosek, A., Büttner, J., Markert, T. and Trixler, F. (2017): Growing low-dimensional supramolecular crystals directly from 3D particles, *CrystEngComm*, 19 (10), pp. 1417–1426. doi: 10.1039/C6CE02348G.

[21] Eberle, A., Greiner, A., Ivleva, N. P., Arumugam, B., Niessner, R. and Trixler, F. (2017): Doping graphene via organic solid-solid wetting deposition, *Carbon*, 125, pp. 84–92. doi: 10.1016/j.carbon.2017.09.043.

[22] Eberle, A., Markert, T. and Trixler, F. (2018): Revealing the Physicochemical Basis of Organic Solid–Solid Wetting Deposition: Casimir-like Forces, Hydrophobic Collapse, and the Role of the Zeta Potential, *Journal of the American Chemical Society*, 140 (4), pp. 1327–1336. doi: 10.1021/jacs.7b10282.

[23] Trixler, F., Heckl, W. M. (2007): Various approaches to control solid/solid wetting self-assembly of organic semiconductors with STM, In *Modern Research and Educational Topics in Microscopy,* Méndez-Vilas, A., Diaz, J., Eds., Formatex: Badajoz, 2007, Vol. 2, pp. 534-541.

[24] Elemans, J. A. A. W., Lei, S. and De Feyter, S. (2009): Molecular and Supramolecular Networks on Surfaces: From Two-Dimensional Crystal Engineering to Reactivity, *Angewandte Chemie International Edition*, 48 (40), pp. 7298–7332. doi: 10.1002/anie.200806339.

[25] Haber, J., Machej, T. and Czeppe, T. (1985): The phenomenon of wetting at solid/solid interface, *Surface Science*, 151 (1), pp. 301–310. doi: 10.1016/0039-6028(85)90468-6.

[26] Leyrer, J., Margraf, R., Taglauer, E. and Knözinger, H. (1988): Solid-solid wetting and formation of monolayers in supported oxide systems, *Surface Science*, 201 (3), pp. 603–623. doi: 10.1016/0039-6028(88)90505-5.

[27] Bertinchamps, F., Grégoire, C. and Gaigneaux, E. M. (2006): Systematic investigation of supported transition metal oxide based formulations for the catalytic oxidative elimination of (chloro)-aromatics, *Applied Catalysis B: Environmental*, 66 (1–2), pp. 1–9. doi: 10.1016/j.apcatb.2006.02.011.

[28] Furukawa, S. and De Feyter, S. (2009): Two-dimensional crystal engineering at the liquid-solid interface, *Top.Cur.Chem.*, 287, pp. 87-133. doi: 10.1007/128_2008_6.

[29] Koepf, M., Chérioux, F., Wytko, J. a. and Weiss, J. (2012): 1D and 3D surface-assisted self-organization, *Coordination Chemistry Reviews*. Elsevier B.V., 256 (23–24), pp. 2872–2892. doi: 10.1016/j.ccr.2012.05.039.

[30] Głowacki, E. D., Tangorra, R. R., Coskun, H., Farka, D., Operamolla, a., Kanbur, Y., Milano, F., Giotta, L., Farinola, G. M. and Sariciftci, N. S. (2015): Bioconjugation of hydrogen-bonded organic semiconductors with functional proteins, *J. Mater. Chem. C*, pp. 6554–6564. doi: 10.1039/C5TC00556F.

[31] Głowacki, E. D., Romanazzi, G., Yumusak, C., Coskun, H., Monkowius, U., Voss, G., Burian, M., Lechner, R. T., Demitri, N., Redhammer, G. J., Sünger, N., Suranna, G. P. and Sariciftci, S. (2014): Epindolidiones-Versatile and Stable Hydrogen-Bonded Pigments for Organic Field-Effect Transistors and Light-Emitting Diodes, *Advanced Functional Materials*, pp. 1–12. doi: 10.1002/adfm.201402539.

[32] Sytnyk, M., Głowacki, E. D., Yakunin, S., Voss, G., Schöfberger, W., Kriegner, D., Stangl, J., Trotta, R., Gollner, C., Tollabimazraehno, S., Romanazzi, G., Bozkurt, Z., Havlicek, M., Sariciftci, N. S. and Heiss, W. (2014): Hydrogen-Bonded Organic Semiconductor Micro- And Nanocrystals: From Colloidal Syntheses to (Opto-) Electronic Devices, *Journal of the American Chemical Society*, 136, pp. 16522–16532.

[33] Głowacki, E. D., Irimia-Vladu, M., Kaltenbrunner, M., Gsiorowski, J., White, M. S., Monkowius, U., Romanazzi, G., Suranna, G. P., Mastrorilli, P., Sekitani, T., Bauer, S., Someya, T., Torsi, L. and Sariciftci, N. S. (2013): Hydrogen-bonded semiconducting pigments for air-stable field-effect transistors, *Advanced Materials*, 25 (11), pp. 1563–1569. doi: 10.1002/adma.201204039.

[34] Głowacki, E. D., Leonat, L., Voss, G., Bodea, M., Bozkurt, Z., Irimia-Vladu, M., Bauer, S. and Sariciftci, N. S. (2011): Natural and nature-inspired semiconductors for organic electronics, *Organic Semiconductors in Sensors and Bioelectronics IV*, 8118, p. 81180M–81180M–10. doi: 10.1117/12.892467.

[35] Głowacki, E. D., Irimia-Vladu, M., Bauer, S. and Sariciftci, N. S. (2013): Hydrogen-bonds in molecular solids – from biological systems to organic electronics, *Journal of Materials Chemistry B*, 1 (31), p. 3742. doi: 10.1039/c3tb20193g.

[36] Wagner, T., Györök, M., Huber, D., Zeppenfeld, P. and Głowacki, E. D. (2014): Quinacridone on Ag(111): Hydrogen bonding versus chirality, *Journal of Physical Chemistry C*, 118 (20), pp. 10911–10920. doi: 10.1021/jp502148x.

[37] Sue, K., Usami, T., Arai, K., Kasai, H., Nakanishi, H. and Hiaki, T. (2007): Quinacridone solubility in hot-compressed water, *Journal of Chemical and Engineering Data*, 52 (3), pp. 714–717. doi: 10.1021/je060466i.

[38] De Feyter, S., Gesquière, A., De Schryver, F. C., Keller, U. and Müllen, K. (2002): Aggregation properties of soluble quinacridones in two and three dimensions, *Chemistry of Materials*, 14 (3), pp. 989–997. doi: 10.1021/cm011053y.

[39] Keller, U., Müllen, K., De Feyter, S. and De Schryver, F. C. (1996): Hydrogen-bonding and phase-forming behavior of a soluble quinacridone, *Advanced Materials*, 8 (6), pp. 490–493. doi: 10.1002/adma.19960080607.

[40] Paulus, E. F., Leusen, F. J. J. and Schmidt, M. U. (2007): Crystal structures of quinacridones, *CrystEngComm*, 9 (2), pp. 131–143. doi: 10.1039/B613059C.

[41] Lincke, G. (2000): A review of thirty years of research on quinacridones. X-ray crystallography and crystal engineering, *Dyes and Pigments*, 44 (2), pp. 101–122. doi: 10.1016/S0143-7208(99)00082-0.

[42] Trixler, F. (2013): Quantum Tunnelling to the Origin and Evolution of Life, *Current organic chemistry*, 17 (16), pp. 1758–1770. doi: 10.2174/13852728113179990083.

[43] Räder, H. J., Rouhanipour, A., Talarico, A. M., Palermo, V., Samorì, P. and Müllen, K. (2006): Processing of giant graphene molecules by soft-landing mass spectrometry., *Nature materials*, 5 (4), pp. 276–280. doi: 10.1038/nmat1597.

[44] Cousty, J. and Pham Van, L. (2002): Formation of partially demixed two-dimensional solid solutions from binary mixtures of n-alkanes with very different lengths, *Physical Chemistry Chemical Physics*, 5 (3), pp. 599–603. doi: 10.1039/b206529k.

[45] Iqbal, M. W., Singh, A. K., Iqbal, M. Z. and Eom, J. (2012): Raman fingerprint of doping due to metal adsorbates on graphene, *Journal of Physics: Condensed Matter*, 24 (33), p. 335301. doi: 10.1088/0953-8984/24/33/335301.

[46] Wang, W. X., Liang, S. H., Yu, T., Li, D. H., Li, Y. B. and Han, X. F. (2011): The study of interaction between graphene and metals by Raman spectroscopy, *Journal of Applied Physics*, 109 (7), pp. 15–18. doi: 10.1063/1.3536670.

[47] Casiraghi, C. (2009): Probing disorder and charged impurities in graphene by Raman spectroscopy, *Physica Status Solidi - Rapid Research Letters*, 3 (6), pp. 175–177. doi: 10.1002/pssr.200903135.

[48] Dong, X., Fu, D., Fang, W., Shi, Y., Chen, P. and Li, L. J. (2009): Doping single-layer graphene with aromatic molecules, *Small*, 5 (12), pp. 1422–1426. doi: 10.1002/smll.200801711.

[49] Liu, H., Liu, Y. and Zhu, D. (2011): Chemical doping of graphene, *Journal of Materials Chemistry*, 21 (10), p. 3335. doi: 10.1039/c0jm02922j.

[50] Ni, Z., Wang, Y., Yu, T. and Shen, Z. (2008): Raman Spectroscopy and Imaging of Graphene, *Nano Research*, 1, pp. 273–291. doi: 10.1007/s12274-008-8036-1.

[51] Li, G., Luican, A. and Andrei, E. Y. (2009): Scanning tunneling spectroscopy of graphene on graphite, *Physical Review Letters*, 102 (17), pp. 1–4. doi: 10.1103/PhysRevLett.102.176804.

[52] Castellanos-Gomez, A., Wojtaszek, M., Arramel, Tombros, N. and Van Wees, B. J. (2012): Reversible hydrogenation and bandgap opening of graphene and graphite surfaces probed by scanning tunneling spectroscopy, *Small*, 8 (10), pp. 1607–1613. doi: 10.1002/smll.201101908.

[53] Hamers, R. J. (1989): Atomic-Resolution Surface Spectroscopy with the Scanning Tunneling Microscope, *Annual Review of Physical Chemistry*, 40 (1), pp. 531–559. doi: 10.1146/annurev.pc.40.100189.002531.

[54] Herbert, F. W., Krishnamoorthy, A., Van Vliet, K. J. and Yildiz, B. (2013): Quantification of electronic band gap and surface states on FeS2(100), *Surface Science*, 618, pp. 53–61. doi: 10.1016/j.susc.2013.08.014.

[55] Lim, S.-J., Leem, D.-S., Park, K.-B., Kim, K.-S., Sul, S., Na, K., Lee, G. H., Heo, C.-J., Lee, K.-H., Bulliard, X., Satoh, R.-I., Yagi, T., Ro, T., Im, D., Jung, J., Lee, M., Lee, T.-Y., Han, M. G., Jin, Y. W. and Lee, S. (2015): Organic-on-silicon complementary metal–

oxide–semiconductor colour image sensors, *Scientific Reports*, 5 (1), p. 7708. doi: 10.1038/srep07708.

[56] Lauffer, P., Emtsev, K. V., Graupner, R., Seyller, T. and Ley, L. (2008): Molecular and electronic structure of PTCDA on bilayer graphene on SiC(0001) studied with scanning tunneling microscopy, *Physica Status Solidi (B)*, 245 (10), pp. 2064–2067. doi: 10.1002/pssb.200879615.

[57] Zhao, L., He, R., Rim, K. T., Schiros, T., Kim, K. S., Zhou, H., Gutierrez, C., Chockalingam, S. P., Arguello, C. J., Palova, L., Nordlund, D., Hybertsen, M. S., Reichman, D. R., Heinz, T. F., Kim, P., Pinczuk, A., Flynn, G. W. and Pasupathy, A. N. (2011): Visualizing Individual Nitrogen Dopants in Monolayer Graphene, *Science*, 333 (6045), pp. 999–1003. doi: 10.1126/science.1208759.

[58] Stokes, R. J., Evans, D. F. (1997): Fundamentals of Interfacial Engineering, Wiley-VHC, Weinheim, 1997, pp 34−41 & 121−163. ISBN: 978-0-471-18647-2.

[59] Attard, P., Kjellander, R., Mitchell, D. J. and Jonsson, B. (1988): Electrostatic fluctuation interactions between neutral surfaces with adsorbed mobile ions or dipoles, *Journal Of Chemical Physics*, 89 (3), pp. 1664–1680. doi: 10.1063/1.455113.

[60] Lau, A. W. C. and Pincus, P. (2002): Counterion condensation and fluctuation-induced attraction, *Physical Review E - Statistical, Nonlinear, and Soft Matter Physics*, 66 (4), pp. 1–14. doi: 10.1103/PhysRevE.66.041501.

[61] Lau, A. W. C., Lukatsky, D. B., Pincus, P. and Safran, S. A. (2002): Charge fluctuations and counterion condensation, *Physical Review E - Statistical, Nonlinear, and Soft Matter Physics*, 65 (5), pp. 1–7. doi: 10.1103/PhysRevE.65.051502.

[62] Kardar, M. and Golestanian, R. (1999): The "friction" of vacuum, and other fluctuation-induced forces, *Reviews of Modern Physics*, 71 (4), pp. 1233–1245. doi: 10.1103/RevModPhys.71.1233.

[63] Bartolo, D., Ajdari, A., Fournier, J.-B. and Golestanian, R. (2002): Fluctuations of fluctuation-induced casimir-like forces., *Phys. Rev. Lett.*, 89, p. 230601. doi: 10.1103/PhysRevLett.89.230601.

[64] Hansen, J. P. and Lowen, H. (2000): Effective interactions between electric double layers., *Annual review of physical chemistry*, 51, pp. 209–242. doi: 10.1146/annurev.physchem.51.1.209.

[65] Golestanian, R. (2005): Fluctuation-induced forces in and out of equilibrium, *Pramana - Journal of Physics*, 64 (6 SPEC. ISS.), pp. 1029–1038. doi: 10.1007/BF02704165.

[66] Lukatsky, D. B. and Safran, S. A. (1999): Pressure of correlated layer-charge and counterion fluctuations in charged thin films, *Phys. Rev. E*, 60 (5), pp. 5848–5857.

[67] Christenson, H. K. and Claesson, P. M. (2001): Direct measurements of the force between hydrophobic surfaces in water, *Advances in Colloid and Interface Science*, 91 (3), pp. 391–436. doi: 10.1016/S0001-8686(00)00036-1.

[68] Hammer, M. U., Anderson, T. H., Chaimovich, A., Shell, M. S. and Israelachvili, J. (2010): The search for the hydrophobic force law, *Faraday Discussions*, 146, pp. 299–308. doi: 10.1039/b926184b.

[69] Remsing, R. C., Xi, E., Vembanur, S., Sharma, S., Debenedetti, P. G., Garde, S. and Patel, A. J. (2015): Pathways to dewetting in hydrophobic confinement., *Proceedings of the*

National Academy of Sciences of the United States of America, 112 (27), pp. 8181–8186. doi: 10.1073/pnas.1503302112.

[70] X. Huang, C. J. Margulis, B. J. B. (2004): Dewetting-induced collapse of hydrophobic particles, *Proceedings of the National Academy of Sciences of the United States of America*, 100 (21), pp. 11953–11958. doi: 10.1073/pnas.1115170108.

[71] Berne, B. J., Weeks, J. D. and Zhou, R. (2009): Dewetting and Hydrophobic Interaction in Physical and Biological Systems, *Annual review of physical chemistry*, 60, pp. 85–103. doi: 10.1146/annurev.physchem.58.032806.104445.

[72] Leong, Y. K., Scales, P. J., Healy, T. W., Boger, D. V. and Buscall, R. (1993): Rheological evidence of adsorbate-mediated short-range steric forces in concentrated dispersions, *J. Chem Soc. Farad. Trans.*, 89 (14), pp. 2473–2478. doi: 10.1039/ft9938902473.

[73] Kozlov, S. M., Viñes, F. and Görling, A. (2011): Bandgap engineering of graphene by physisorbed adsorbates, *Advanced Materials*, 23 (22–23), pp. 2638–2643. doi: 10.1002/adma.201100171.

[74] Jacobasch, H. J., Simon, F. and Weidenhammer, P. (1998): Adsorption of ions onto polymer surfaces and its influence on zeta potential and adhesion phenomena, *Colloid and Polymer Science*, 276 (5), pp. 434–442. doi: 10.1007/s003960050263.

[75] Tandon, V., Bhagavatula, S. K., Nelson, W. C. and Kirby, B. J. (2008): Zeta potential and electroosmotic mobility in microfluidic devices fabricated from hydrophobic polymers: 1. The origins of charge, *ELECTROPHORESIS*, 29 (5), pp. 1092–1101. doi: 10.1002/elps.200700734.

[76] Tandon, V. and Kirby, B. J. (2008): Zeta potential and electroosmotic mobility in microfluidic devices fabricated from hydrophobic polymers: 2. Slip and interfacial water structure, *ELECTROPHORESIS*, 29 (5), pp. 1102–1114. doi: 10.1002/elps.200800735.

[77] Vrbka, L., Mucha, M., Minofar, B., Jungwirth, P., Brown, E. C. and Tobias, D. J. (2004): Propensity of soft ions for the air/water interface, *Current Opinion in Colloid & Interface Science*, 9 (1–2), pp. 67–73. doi: 10.1016/j.cocis.2004.05.028.

List of Figures

List of Tables

Appendix

I. Low Cost Fabrication of Organic Semiconductor Monolayer via OSWD

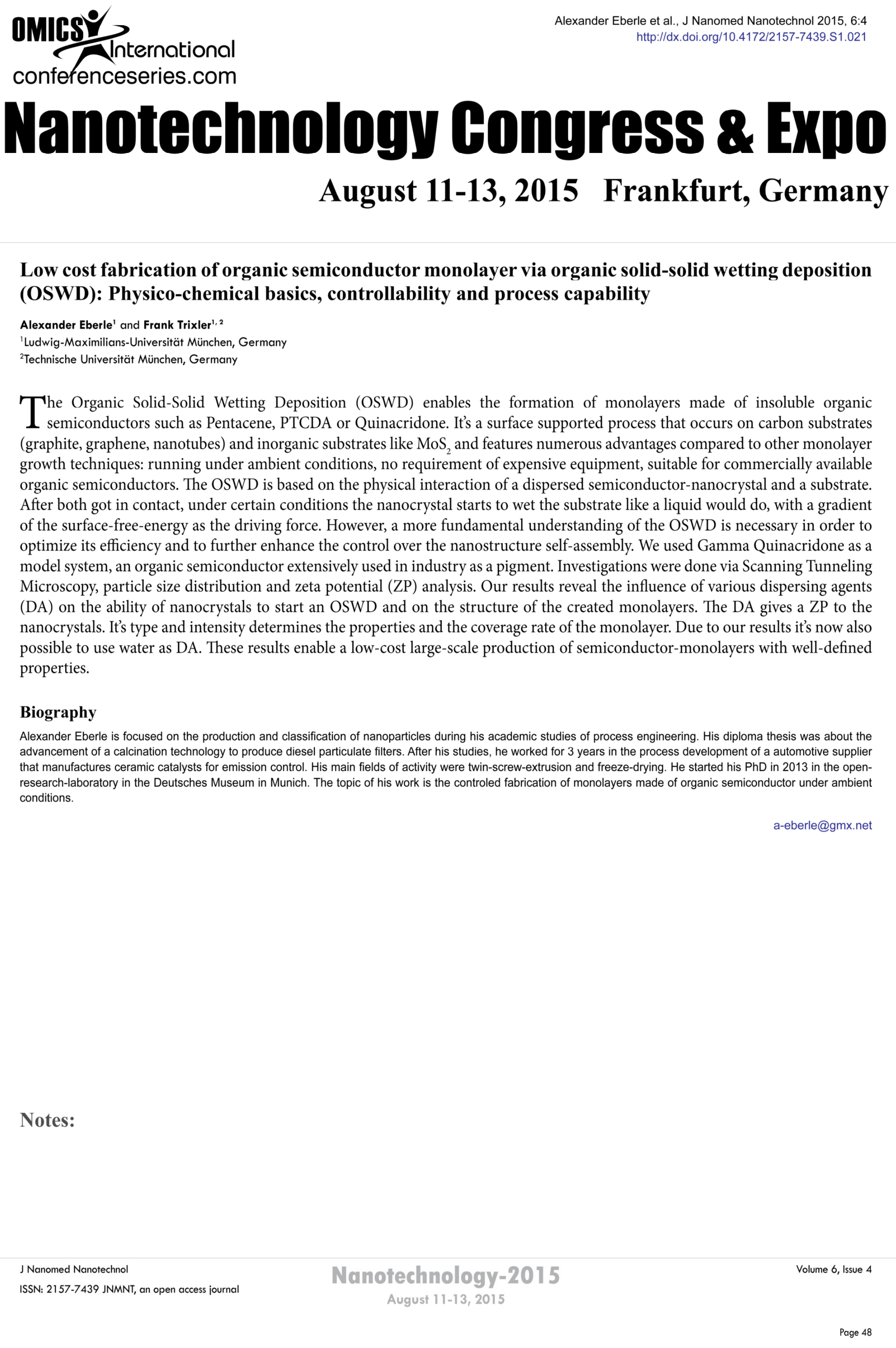

OMICS International
conferenceseries.com

Alexander Eberle et al., J Nanomed Nanotechnol 2015, 6:4
http://dx.doi.org/10.4172/2157-7439.S1.021

Nanotechnology Congress & Expo
August 11-13, 2015 Frankfurt, Germany

Low cost fabrication of organic semiconductor monolayer via organic solid-solid wetting deposition (OSWD): Physico-chemical basics, controllability and process capability

Alexander Eberle[1] and **Frank Trixler**[1, 2]
[1]Ludwig-Maximilians-Universität München, Germany
[2]Technische Universität München, Germany

The Organic Solid-Solid Wetting Deposition (OSWD) enables the formation of monolayers made of insoluble organic semiconductors such as Pentacene, PTCDA or Quinacridone. It's a surface supported process that occurs on carbon substrates (graphite, graphene, nanotubes) and inorganic substrates like MoS_2 and features numerous advantages compared to other monolayer growth techniques: running under ambient conditions, no requirement of expensive equipment, suitable for commercially available organic semiconductors. The OSWD is based on the physical interaction of a dispersed semiconductor-nanocrystal and a substrate. After both got in contact, under certain conditions the nanocrystal starts to wet the substrate like a liquid would do, with a gradient of the surface-free-energy as the driving force. However, a more fundamental understanding of the OSWD is necessary in order to optimize its efficiency and to further enhance the control over the nanostructure self-assembly. We used Gamma Quinacridone as a model system, an organic semiconductor extensively used in industry as a pigment. Investigations were done via Scanning Tunneling Microscopy, particle size distribution and zeta potential (ZP) analysis. Our results reveal the influence of various dispersing agents (DA) on the ability of nanocrystals to start an OSWD and on the structure of the created monolayers. The DA gives a ZP to the nanocrystals. It's type and intensity determines the properties and the coverage rate of the monolayer. Due to our results it's now also possible to use water as DA. These results enable a low-cost large-scale production of semiconductor-monolayers with well-defined properties.

Biography

Alexander Eberle is focused on the production and classification of nanoparticles during his academic studies of process engineering. His diploma thesis was about the advancement of a calcination technology to produce diesel particulate filters. After his studies, he worked for 3 years in the process development of a automotive supplier that manufactures ceramic catalysts for emission control. His main fields of activity were twin-screw-extrusion and freeze-drying. He started his PhD in 2013 in the open-research-laboratory in the Deutsches Museum in Munich. The topic of his work is the controled fabrication of monolayers made of organic semiconductor under ambient conditions.

a-eberle@gmx.net

Notes:

Acknowledgement

Undertaking the doctoral studies has been one of the most significant academic challenges that I ever had to face. Surviving this stressful, time-consuming, and often frustrating period would not have been possible without the support and assistance of a few remarkable people, to whom I would like to express my deepest gratitude in this exclusive section.

First and foremost, I would like to express my deepest gratitude to my supervising tutor, Frank Trixler. Thank you so much Frank for providing me the opportunity of fulfilling my dream of becoming a Ph.D., for giving me the freedom to develop my own ideas, for being a constant source of inspiration whenever I felt stuck, and most importantly, for helping and guiding me through the hardships of publishing scientific papers.

Next, I feel immensely grateful to my doctoral supervisor, Wolfgang W. Schmahl, for kindly accepting me as a Ph.D. student and for such inspiring discussions that paved completely new paths in exploring the very basics of the OSWD process. In this regard, a special thanks goes as well to Guntram Jordan, for his excellent idea of performing DLVO theory related simulations.

Further, I am extremely obliged to Volker Diete-Wendl, for having introduced me to the very secret and hardly understandable arts of using our home-built STM. Only due to his tutorials and the tricks and ruses he taught me, was it possible for me to generate all the fancy STM pictures that can be seen within this dissertation.

Besides, my sincere gratitude extends as well to my colleague and co-author Andrea Greiner, who not only managed to bring one of the two broken STM's back to life but performed some essential measurements for our Carbon paper just in time (after I had almost given up all the hope to meet the deadline). Heartfelt acknowledgment is expressed additionally to our student apprentice Michaela Wenner for her valuable assistance, particularly during the sample reworking experiments, enabling me to juggle with my doctoral studies and a half-time job with much more ease.

Another special gratitude is conveyed to Natalia P. Ivleva, from the Chair for Analytical Chemistry at the TUM, for her constant and extremely valuable advices in the analysis and interpretation of Raman spectra, significantly increasing my understanding of the issue.

Furthermore, I feel highly indebted to Martina Zeiler from the Papiertechnische Stiftung in München, for her quick and constant support regarding the zeta potential measurements, providing a substantial contribution in understanding the basis of the OSWD process.

I would like to also warmly thank Manfred Seidel from the Deutsche Museum, whose expertise in the field of chemistry was such a valuable input at all times and, equally important, for his practical assistance in the often-chaotic daily life of the Deutsches Museum, as and when needed.

Heartfelt acknowledgment is expressed as well to Neeti Phatak for her invaluable support with the proofreading and editing of the scientific papers and for devoting often her weekends at short notices, as to significantly improve the linguistic quality of my publications.

Apart from the aid of various people that were directly involved in my doctoral studies, I further would like to acknowledge some special supporters at the Helmholtz Institute Erlangen-Nürnberg (HI ERN) for their invaluable support in the background. In this respect, the prime and utmost gratitude is extended to my boss, Karl Mayrhofer, who offered me a job without having me finished my Ph.D. Even though he knew, probably better than I did, that the duration of doctoral studies is incalculable, he was generous enough to give me the adequate time required to finish it. Dear Karl, thank you very much from the bottom of my heart for this!

Besides, a very heartfelt gratitude is expressed to all my colleagues at the HI ERN, for making me feel as a part of a research community, for their priceless advices and assistance, particularly with regard to the doctoral studies, and last but not the least, for boosting up my spirits from time-to-time. Peyman Khanipour, Marcus Pohl, Ioannis Katsounaros, Andreas Reichert, Achim Mannke, and many more - thank you very much for being there for me!

It is rightly said that the love of a family is life’s greatest blessing. I owe my deepest gratitude to all my family members, particularly to my uncle Thomas Eberle, my parents-in-law, Gertrud und Raimund Hoff, my grandparents, Dietmar und Carola Wagner, my father, Martin Eberle, and my grandmother, Elisabeth Eberle, for their unconditional support and their constant belief in me, throughout all stages of this work. A very heartfelt thanks is extended as well to all my friends who implicitly stood behind me, who always made my gloomy days brighter, and especially to those who warmly welcomed me and my wife back in Nürnberg, giving me the strength to carry on.

Finally, yet importantly, I feel eternally grateful to the most important person of my life, my wife Verena Eberle. Dear Verena, thank you so much for always supporting me in these seemingly endless years of my life, for always being there for me through thick and thin, for your constant belief and faith in me and my work, and for your outstanding patience. Without your love and support, undoubtedly, I would not have had the strength to survive the doctoral studies. Thank you so much for being a part of my life!

4. List of Publications

4.1. Journal Publications

Eberle, A. and Trixler, F. (2015): Low cost fabrication of organic semiconductor monolayer via organic solid-solid wetting deposition (OSWD): Physico-chemical basics, controllability and process capability, *Journal of Nanomedicine & Nanotechnology*, 6 (4), p. 48. doi: 10.4172/2157-7439.S1.021.

Eberle, A., Nosek, A., Büttner, J., Markert, T. and Trixler, F. (2017): Growing low-dimensional supramolecular crystals directly from 3D particles, *CrystEngComm*, 19 (10), pp. 1417–1426. doi: 10.1039/C6CE02348G.

Eberle, A., Greiner, A., Ivleva, N. P., Arumugam, B., Niessner, R. and Trixler, F. (2017): Doping graphene via organic solid-solid wetting deposition, *Carbon*, 125, pp. 84–92. doi: 10.1016/j.carbon.2017.09.043.

Eberle, A., Markert, T. and Trixler, F. (2018): Revealing the Physicochemical Basis of Organic Solid–Solid Wetting Deposition: Casimir-like Forces, Hydrophobic Collapse, and the Role of the Zeta Potential, *Journal of the American Chemical Society*, 140 (4), pp. 1327–1336. doi: 10.1021/jacs.7b10282.

4.2. Talks at Conferences

Assembly of organic semiconductor monolayer via solid-solid wetting: physico-chemical basics, controllability, process capability
Eberle, A., Kristallographisches Oberseminar, München, Germany, June 13, 2014.

Assembly of organic semiconductor monolayer via solid-solid wetting: physico-chemical basics, controllability, process capability
Eberle, A., 79. Jahrestagung der DPG (Deutschen Physikalischen Gesellschaft) und DPG Frühjahrestagung, Berlin, Germany, March 15 – 20, 2015.

Oberflächenbenetzung durch Pigmentpartikel: Erzeugung molekular dünner Nanoschichten unter einfachsten Bedingungen
Eberle, A., Nanotechnologie bei der Papierherstellung und in verwandten Branchen, Munich, Germany, April 28 – 29, 2015.

Low cost fabrication of organic semiconductor monolayer via Organic Solid-Solid Wetting Deposition (OSWD): physico-chemical basics, controllability, process capability
Eberle, A., Nanotechnology congress & Expo, Frankfurt, Germany, August 11 – 13, 2015.

Growing low-dimensional crystals directly from 3D particles via solid-solid wetting
Eberle, A., Kristallographisches Oberseminar, München, Germany, October 23, 2015.

4.3. Poster Presented at Conference

Characteristics and controllability of solid-wetting Deposition of organic semiconductors
Eberle, A., F. Trixler, Nanosciences: Great Adventures on Small Scales, San Servolo (Venice), Italy, September 16 – 20, 2013.